



Title	Production of polarized $^3\text{He}$ ion beam based on electron pumping
Author(s)	有本, 靖
Citation	大阪大学, 2000, 博士論文
Version Type	VoR
URL	<a href="https://doi.org/10.11501/3169104">https://doi.org/10.11501/3169104</a>
rights	
Note	

*The University of Osaka Institutional Knowledge Archive : OUKA*

<https://ir.library.osaka-u.ac.jp/>

The University of Osaka

Production of polarized  $^3\text{He}$  ion beam based on  
electron pumping method

平成11年度

大阪大学大学院理学研究科物理学専攻

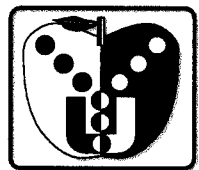
有本 靖

Doctor Thesis 2000

# **Production of polarized $^3\text{He}$ ion beam based on electron pumping method**

Y. Arimoto

*Research Center for Nuclear Physics  
Osaka University*



## Abstract

We have constructed a polarized  $^3\text{He}$  ion source based on a new method, "electron pumping method" at the Research Center for Nuclear Physics, Osaka University. The  $^3\text{He}^+$  ions do multiple electron capture and stripping collision with the polarized Rb atom in a 2-T magnetic field and atomically polarizes. Half of the polarization is transferred from the electron of  $^3\text{He}^+$  to the nucleus by the hyperfine interaction. The  $^3\text{He}^+$  ions are produced by a duoplasmatron ion source. An electron of Rb atom is polarized by means of optical pumping using a circularly polarized laser light. The nuclear polarization is measured by the polarimeter based on beam-foil spectroscopy.

To verify the principle of electron pumping, the nuclear polarization dependence on the Rb vapor thickness was measured. It was observed that the  $^3\text{He}$  polarization increased with the increase of the vapor thickness in the range of  $2\sim 6\times 10^{14}$  atoms/cm<sup>2</sup>, which is a characteristic feature of the electron pumping. The obtained maximum nuclear polarization was 5.5 %. This nuclear polarization was obtained under the following conditions: The  $^3\text{He}^+$  current was about  $200\mu\text{A}$  at 19 keV. The Rb vapor polarization was 16% and the thickness was  $5.5\times 10^{14}$  atoms/cm<sup>2</sup> where one cycle of electron capture and stripping process is occurred. The photon counting rate at the polarimeter was 5 kcps at S/N ratio of 50. From the theoretical calculation of the spin-exchange cross section, it was found that a contribution of this process to the polarization growth of  $^3\text{He}$  is small compared to the multiple charge exchange process, i.e., the electron pumping.

In the electron pumping method, it is necessary to polarized Rb vapor at high density to achieve multiple charge exchange collision between  $^3\text{He}$  ions/atoms and Rb atoms. However it is difficult to obtain highly polarized Rb vapor due to various depolarization effects. In order to improve Rb polarization at high density, the relaxation rates of the polarized Rb vapor were measured by using a chopped pumping laser varying the magnetic field, Rb cell temperature, and frequency of the pumping laser. The experimental results showed that two components, i.e., a fast component with the relaxation rate of  $\sim 65\text{ ms}^{-1}$  and a slow component with the relaxation rate of  $\sim 1\text{ ms}^{-1}$  contribute. It was found that the slow component was well explained by the wall relaxation and the effusion effect. On the other hand, the fast component is due to a formation of the localized Rb polarization around the pumping laser by a radiation trapping effect and a subsequent relaxation process due to an effusion.

# Contents

<b>1</b>	<b>Introduction</b>	<b>7</b>
<b>2</b>	<b>Brief history of polarized ion sources</b>	<b>9</b>
2.1	History of polarized hydrogen/deuterium ion source . . . . .	9
2.2	Brief history of polarized $^3\text{He}$ ion sources . . . . .	10
<b>3</b>	<b>Basic descriptions</b>	<b>13</b>
3.1	Electron pumping . . . . .	13
3.1.1	Difficulties in polarizing $^3\text{He}$ by the OPPIS . . . . .	13
3.1.2	Principle of electron pumping . . . . .	14
3.1.3	Quantitative treatment of electron pumping . . . . .	17
3.1.4	Effective nuclear charge and LS decoupling field . . . . .	18
3.2	Relaxation of optically pumped Rb vapor . . . . .	20
3.2.1	General view . . . . .	20
3.2.2	Relaxation models . . . . .	21
3.3	Problems on the beam profiles created by the electron pumping . . . . .	23
3.3.1	Creation of a polarization hole . . . . .	24
3.3.2	Monte Carlo simulation . . . . .	25
3.3.3	Various facet of the polarization hole derived from the Monte Carlo simulation . . . . .	26
3.3.4	Analytical formalism for $r_{\text{hole}}$ and $d_{\text{hole}}$ . . . . .	29
<b>4</b>	<b>Experimental Apparatus</b>	<b>35</b>
4.1	Layout of the electron pumping polarized $^3\text{He}$ ion source . . . . .	35
4.1.1	Beam transport system . . . . .	35
4.1.2	Duoplasmatron ion source . . . . .	36
4.1.3	Optical pumping . . . . .	37
4.1.4	Superconducting solenoidal magnet . . . . .	44
4.1.5	Beam-foil polarimeter . . . . .	46
4.2	Computer control data acquisition systems . . . . .	51

<b>5</b>	<b>Experimental results and discussion</b>	<b>57</b>
5.1	Verification of the electron pumping . . . . .	57
5.1.1	Rb polarization vs Rb vapor thickness . . . . .	57
5.1.2	$^3\text{He}$ nuclear polarization vs Rb vapor thickness . . . . .	58
5.1.3	Spin-exchange cross section . . . . .	61
5.1.4	Calculation including transition to other states . . . . .	63
5.1.5	Extraction of experimental value of the spin-exchange cross section . . . . .	64
5.2	Optimization of the electron pumping polarized $^3\text{He}$ ion source . . . . .	65
5.2.1	Dependence on pumping laser power . . . . .	66
5.2.2	Dependence on $^3\text{He}^+$ ion current . . . . .	67
5.2.3	Impact energy dependence . . . . .	69
5.3	Relaxation of optically pumped Rb vapor . . . . .	70
5.3.1	A brief review of measurement . . . . .	71
5.3.2	Experimental results . . . . .	72
5.3.3	Comparison of the experimental results with the model calculations . . . . .	75
5.3.4	Conclusion from study on Rb relaxation . . . . .	79
5.4	Possible origin of reduction of $^3\text{He}$ polarization . . . . .	80
5.4.1	Radial localization of Rb polarization . . . . .	81
5.4.2	Polarization hole effect . . . . .	82
<b>6</b>	<b>Future prospect</b>	<b>83</b>
6.1	Feasibility of the electron pumping ion source . . . . .	83
6.1.1	Definition of $Q$ factor, figure of merit . . . . .	83
6.1.2	Improvement of $^3\text{He}$ polarization . . . . .	83
6.1.3	Improvement of $^3\text{He}^+$ beam current . . . . .	84
6.2	Evaluation of $Q$ factor for electron pumping polarized ion source . . . . .	84
6.3	Possibility of spin-exchange polarized ion source . . . . .	85
6.4	Application of polarized $^3\text{He}$ ion source . . . . .	85
<b>7</b>	<b>Conclusion</b>	<b>89</b>
<b>A</b>	<b>Mechanism of spin-exchange</b>	<b>93</b>
<b>B</b>	<b>Potential energy for <math>(\text{He-Rb})^+</math> molecule</b>	<b>97</b>
<b>C</b>	<b>A Monte Carlo simulation for evaluating a radial distribution of the Rubidium polarization caused by a radiation trapping effect</b>	<b>101</b>
<b>D</b>	<b>Analytical estimation of polarization hole</b>	<b>103</b>

*Contents*

5

**E Fraction of  $\text{Rb}^+$  produced by charged particle**

**107**

# Chapter 1

## Introduction

The polarization phenomena in nuclear physics have been one of the important probes to investigate nuclear reaction mechanisms and nuclear structures since the first double scattering measurement performed in the beginning of 50's. To efficiently measure spin observables, nuclear polarized beams are indispensable. For this purpose, enormous efforts have been paid for developing polarized ion sources since the pioneering work on the polarized proton ion source by Clausnitzer, Fleischmann, and Schopper [1].

Although intense beams of polarized protons, deuterons and possibly heavy ions, such as  ${}^6,7\text{Li}$  and  ${}^{23}\text{Na}$ , are available today, this is not the case for  ${}^3\text{He}$ . The polarized  ${}^3\text{He}$  beams were so far practically used for nuclear physics only at the University of Birmingham and at Rice University in 70th. However, their kinetic energies were limited at low energy region less than 50 MeV and both devices have been already terminated.

Recently, nuclear physics with polarized  ${}^3\text{He}$  beams has received much attention in particular at an intermediate and high energy region [2]. In the former energy region, importance of the polarized  ${}^3\text{He}$  beam is suggested for studying the spin-isospin excitation modes in nuclei by the ( ${}^3\text{He},t$ ) reaction, the few body problems, and the time reversal invariance. In the latter energy region, the experiments on the deep inelastic scattering of a polarized  ${}^3\text{He}$  target by leptons, such as an electron and a muon have been performed as a counter part of a polarized proton/deuteron for studying the contribution of quarks and gluons in nucleon since, so called, the spin crisis in 1988 [3].

On the basis of the above circumstances, we decided to construct a polarized  ${}^3\text{He}$  ion source which could provide a polarized  ${}^3\text{He}$  ion beam with a high intensity and a high polarization. Among the various types of polarization methods, we chose a method so called, OPPIS ( Optical Pumping Polarized Ion Source ), which employs an electron capture process between a fast  ${}^3\text{He}^{2+}$  ion and an alkali-metal vapor (Rb) polarized by means of the laser optical pumping, as one of the promising methods since the OPPIS showed great advantage in producing a polarized proton beam with a high intensity and a high polarization. However, after an elaborate effort in developing this

type of the polarized  $^3\text{He}$  ion source, it was found that a serious drawback, i.e., a reduction of the polarization and a growth of the beam emittance of the  $^3\text{He}$  ions were unavoidable.

In order to solve this problem, a breakthrough was eagerly anticipated. After an earnest consideration to the next step, we had finally reached a novel idea to produce a polarized  $^3\text{He}$  beam without sacrificing both the polarization and the beam intensity of  $^3\text{He}$  ions. We named this method an "electron pumping".

This idea is based on an extended concept of the OPPIS; the OPPIS uses a single process of the electron capture, while the electron pumping uses the multiple cycles of the electron capture and stripping. An advantage of the electron pumping is that the depolarization and the beam emittance growth would be reduced. The fundamental importance of the electron pumping is that the polarized electrons in the electron pumping play a role similar to the polarized photons in the OPPIS. This strongly indicates that the electron pumping is an extended concept of the optical pumping discovered by Kastler [4].

However, it is more difficult to realize the conditions necessary for the electron pumping than for the OPPIS. The electron pumping requires much higher alkali-metal vapor thickness than the OPPIS. As a result, we may meet serious problems which never occurred in the OPPIS. In fact, we encountered an unexpected reduction of the polarization for the alkali-metal vapor, an emittance growth, and an polarization spatial distribution due to multiple collisions. Besides the above problems, one must pay attention to the spin-exchange collision between an incident  $^3\text{He}^+$  ion and a polarized alkali-metal vapor since this term also contributes to generate the  $^3\text{He}$  polarization. However, no discussion on this term has been done on the  $^3\text{He}$  plus Rb system so far. Therefore, the investigation of this term is necessary to experimentally verify the principle of the electron pumping.

Although the present work is primarily concerned with an experimental verification of the electron pumping, a detailed study on the relaxation mechanism of the polarized Rb vapor was also investigated to understand phenomena occurring at an extremely high Rb vapor density by introducing simple models. The experimental value of the spin-exchange cross section which contributes to the electron pumping was compared with the theoretical calculations assuming formation of quasimolecules consisting of a Rb atom and a  $^3\text{He}^+$  ion.

This article consists of three major subjects, i.e., verification of the electron pumping, the relaxation mechanism of the Rb vapor, and spin-exchange cross section for  $^3\text{He}^+$ -Rb system. In chapter 2, a historical review of the polarized ion sources is given. In chapter 3, the basic descriptions are given on the concepts of the electron pumping, the relaxation mechanism of the Rb vapor, and the spin-exchange processes. In chapter 4, an experimental apparatus is described. In chapter 5, experimental results and discussion are mentioned. In chapter 6, future prospects are described, where the improvements of the polarized  $^3\text{He}$  ion source and an idea of polarized  $^3\text{He}$  ion source based on the spin-exchange process are presented. Conclusion is given in chapter 7, closing chapter.

## Chapter 2

# Brief history of polarized ion sources

In this chapter, a brief history of polarized ion sources is presented individually for hydrogen/deuterium and  $^3\text{He}$  ions.

### 2.1 History of polarized hydrogen/deuterium ion source

As commented in the preceding chapter, the first measurement on the production of the nuclear polarized beams, so called, the double scattering experiment, were done to investigate the non-central n-p interaction at high energy by the 184-inch synchro-cyclotron at Berkeley[5].

On the other hand, a construction of a polarized proton ion source based on the Stern-Gerlach's experiment with a quadrupole magnet was designed and constructed in the middle 1950's [1]. This is a beginning of the atomic beam polarized ion source. Though they succeeded in separating four hyperfine states of a hydrogen atom, they could not produce a polarized proton beam because of a large background. It was 1960 that Huber et. al. succeeded in producing a polarized ion beam by using a deuteron gas instead of a hydrogen gas, thus eliminating the background. The ABS type polarized ion source is working nowadays at many laboratories including RCNP [6], IUCF [7], COSY [8], etc.

A modern type ABS developed for practical use has a composition as follows: A H atom beam with a temperature of 30~80 K dissociated by a radio frequency is led to a sextupole or quadrupole magnet. This magnet has a function to focus a H atom with a component,  $m_j=+1/2$  and to defocus a H atom with a component,  $m_j=-1/2$ . The focused component of the atomic polarized H atom is then introduced to the transition regions (either weak transition, or strong transition), where the atomic polarization is transferred to the proton polarization by using the weak field transition between the hyperfine states. The nuclear polarized H atoms are ionized positively or negatively by an ECR (electron cyclotron resonance) ion source, electron beam impact, or resonant charge exchange collisions.

On the other hand, possibility to polarize a proton beam by using a Lamb-shift was pointed

out by Lamb and Retherford in 1950. They suggested that hydrogen atoms in the 2s (metastable) state can be polarized by passage through a magnetic field of 575 G crossed by a weak electric field [9]. Since then, there has been interest in using this technique to produce a beam of polarized nuclei for injection into accelerators, and experiments along this line were carried out by Madansky and Owen [10]. However, in these experiments the ion beams arising from metastable atoms was masked by a larger beam of ions arising from the ground-state atoms. But in 1965, Donnelly and Sawyer solved this problem and succeeded in producing the polarized hydrogen by this method [11]. They produced a beam by charge exchange in a Cs vapor and converted it to negative ions in an Ar gas cell [12]. This type of polarized ion source is called a Lamb-shift ion source and now are working at many laboratories; such as Tsukuba University etc. The Lamb-shift type ion source is suitable particularly for injection into a tandem Van de Graaff accelerator because this device can produce predominantly high intensity negative ions.

In 1979, Anderson (Wisconsin University) had suggested a new type polarized proton ion source [13]. The original idea of this method is due to Zavoiskii [14]. He suggested production of polarization by passing a fast proton beam through a thin ferromagnetic foil. A more practical idea was proposed by Haeberli [15], and later by Anderson. He proposed to use an alkali-metal vapor optically pumped as a source of polarized electrons. This ion source was later named an OPPIS (Optically Pumped Polarized Ion Source). A first polarized proton beam from the OPPIS was successfully extracted by Y. Mori ( KEK ) in 1983 [16]. Nowadays, the OPPIS is working for practical use at several laboratories such as; KEK [17], TRIUMF [18, 19, 20, 21, 22], LAMPF [23], and INR [24]. It is noteworthy to mention that the OPPIS to be used at TRIUMF is working with a satisfactory performance for the nuclear physics research. The OPPIS at RHIC and HERA are almost ready for use for high energy physics by Zelenski [25].

A modern OPPIS has a composition shown below: Protons produced by an ECR ion source are injected into a polarized alkali-metal vapor and they capture polarized electrons forming an atomically polarized hydrogen. The polarized hydrogen atoms are, then, introduced to a spin-reversal region, so called, the Sona transition [26] to transfer the atomic polarization to nuclear one. The nuclear polarized H atoms, then, enter a Na-vapor ionizer cell where they pick up another electron forming negative H ions and finally injected into the accelerator.

## 2.2 Brief history of polarized $^3\text{He}$ ion sources

Finally in this section, a short history of the polarized  $^3\text{He}$  ion sources is presented. A first trial to produce a polarized  $^3\text{He}$  beam was made by S. Baker et. al. [27] in 60th. They produced a polarized  $^3\text{He}$  beam by extracting polarized  $^3\text{He}^+$  ions from a discharge of a metastability spin exchange pumped cell. The  $^3\text{He}^+$  polarization and beam current realized by this method was 0.11 and 8  $\mu\text{A}$ , respectively [27].

The second method for production of a polarized  $^3\text{He}^{2+}$  beam was based on a sophisticated

technique using the Lamb shift method [28]. The polarization and the beam current achieved by this method was almost 0.7 and 4  $\mu\text{A}$ . Though this ion source was working at Birmingham University for research of nuclear physics in the 70th and 80th, it was terminated in the mid 80th because of the budgetary reason. Application of the ABS to  $^3\text{He}$  had been done by Slobodrian et. al. in 1984 [29]. They used a  $2^3\text{S}_1$  state of  $^3\text{He}$  which is metastable with a long life time. But, since the produced beam current was very small due to difficulty in production of large amount of the metastable  $^3\text{He}$  atoms, this experiment was interrupted.

M. Tanaka et. al. tried to produce a polarized  $^3\text{He}$  ion beam based on the OPPIS from 1987. But, due to problem on the LS decoupling field the polarization obtainable in principle should be reduced to 0.3 [30].

Belov proposes an ion source with a resonant charge-exchange plasma ionizer. Polarized  $^3\text{He}$  atoms in this scheme are produced by the optical pumping with metastability exchange and then the polarized atoms are stored in a storage cell. Unpolarized  $^4\text{He}^{2+}$  ions are formed in a separate unpolarized plasma source and are injected into the charge-exchange region in which the polarized  $^3\text{He}^{2+}$  ions are produced by the resonant charge-exchange of the polarized  $^3\text{He}$  atoms with the unpolarized  $^4\text{He}^{2+}$  ions [31].

## Chapter 3

# Basic descriptions

This chapter describes the physical background of the electron pumping and related subjects, i.e., the relaxation mechanism of the polarized Rb vapor, the spin-exchange processes between a  $^3\text{He}^+$  ion and a Rb atom, and the spatial distribution of the  $^3\text{He}$  polarization, i.e., a polarization hole.

### 3.1 Electron pumping

Discussion of this section is placed mainly upon a principle of the electron pumping. As was mentioned already, the electron pumping was invented to overcome difficulties in polarizing  $^3\text{He}^+$  ions by means of the OPPIS. Therefore, we will start with description of the difficulties in the OPPIS when the OPPIS is applied to polarize  $^3\text{He}$  nucleus.

#### 3.1.1 Difficulties in polarizing $^3\text{He}$ by the OPPIS

Historically, the OPPIS greatly succeeded in polarizing protons. This suggested possibility to polarized composite particles such as  $^3\text{He}$ ,  $^6,7\text{Li}$ , et al. However, if one applies this method to the  $^3\text{He}$  polarization, serious difficulties never experienced with the proton polarization should be overcome as shown below.

The first problem is much larger depolarization than for the proton OPPIS due to an insufficient LS decoupling field. When a polarized electron of Rb atom is captured by an incident  $^3\text{He}^+$  ion, the captured electron is usually in an excited state. The electron in the excited state, then, deexcites to the lower states by emitting photons, and finally reaches the ground state or metastable state. During the photon emission process, a certain amount of the electron spin polarization would be carried away by the emitted photons if the LS decoupling is insufficient. A magnetic field to fully decouple the LS coupling scheme is expressed for a hydrogen like atom as

$$B_z \propto Z^4. \quad (3.1)$$

Here,  $Z$  is a nuclear charge. In case of a hydrogen, this magnetic field is practically 1~2 T. On the other hand, for a singly charged helium,  ${}^3\text{He}^+$ , this is estimated to be 16~32 T by scaling the proton result. The realization of this huge magnetic field is impractical. As a matter of fact, we are currently using a few tesla generated by a superconducting solenoidal magnet as an LS decoupling field. Of course, this strength is far weaker than that required for the  ${}^3\text{He}^+$  LS decoupling. This is a major reason why large depolarization is caused for the OPPIS applied to the  ${}^3\text{He}$  polarization.

The second serious problem of the  ${}^3\text{He}$  OPPIS is a large beam emittance growth due to the fringing field of the LS decoupling field. In the  ${}^3\text{He}$  OPPIS, a  ${}^3\text{He}^{2+}$  is incident on a Rb vapor cell where a strong LS decoupling field is applied and emerges from it after an electron capture. As Ohlsen pointed out, a beam emittance growth due to the fringing magnetic field would be unavoidable when a net charge changes in the magnetic field [32].

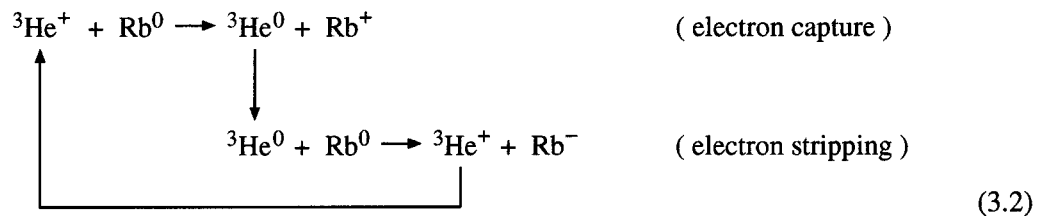
The above problems in the  ${}^3\text{He}$  OPPIS would make it difficult to realize a practical polarized  ${}^3\text{He}$  ion source with a high intensity and high polarization. As a result, a novel method to overcome these difficulties are sincerely anticipated.

The electron pumping method, then, came on stage to eliminate the above difficulties. A basic principle of the electron pumping was, proposed by Tanaka et al. [33] a few years ago.

### 3.1.2 Principle of electron pumping

The electron pumping method was invented to solve the problems listed in the preceding subsection, i.e., large depolarization, and a large beam emittance growth. In what follows, an intuitive picture of a novel principle, the electron pumping is described, through which one can understand how successfully the above problems could be solved by the novel method.

The electron pumping method uses repeated cycles of the electron capture and stripping processes for an incident fast  ${}^3\text{He}^+$  ion (not  ${}^3\text{He}^{2+}$  but  ${}^3\text{He}^+$  ion!) on a polarized thick Rb vapor under presence of a strong magnetic field ( $\sim 2$  T). The cycle is expressed as follows:



When an incident  ${}^3\text{He}^+$  ion has a kinetic energy of about a few keV/amu, major processes are electron capture for  ${}^3\text{He}^+$  ions and electron stripping for  ${}^3\text{He}$  atoms, while an electron stripping of a  ${}^3\text{He}^+$  ion to form a  ${}^3\text{He}^{2+}$  ion, or an electron capture of a  ${}^3\text{He}$  atom to form a  ${}^3\text{He}^-$  ion is negligible small.

In the capture process, a valence electron of the Rb atom is transferred to a  ${}^3\text{He}^+$  ion and a neutral  ${}^3\text{He}$  atom is formed usually in the excited states. If the formed  ${}^3\text{He}$  atom is in a magnetic

field,  $B_{LS}$  strong enough to decouple the LS coupling scheme, the electron spin polarization is well kept during photon deexcitation processes. In this process, it is considered that the electron in the excited state feels an effective nuclear charge  $Z_e \sim 1$  due to screening effect by the electron in ground state. As a result, it is expected that  $B_{LS}$  needed for this case is almost equal to that for the proton case, i.e., only a 1~2 T.

On the other hand, in the stripping process during the cycle of the electron pumping, no depolarization is expected. As a result, it is concluded that no serious depolarization occurs through the above cycles if a magnetic field of about 2 T is applied.

Under the above condition, we consider about the growth of the polarization by the repeated cycles mentioned above.

Suppose that an unpolarized  ${}^3\text{He}^+$  ion beam is incident on a polarized Rb vapor as shown in Fig. 3.1. An incident  ${}^3\text{He}^+$  ion first captures a polarized electron from a Rb atom forming an

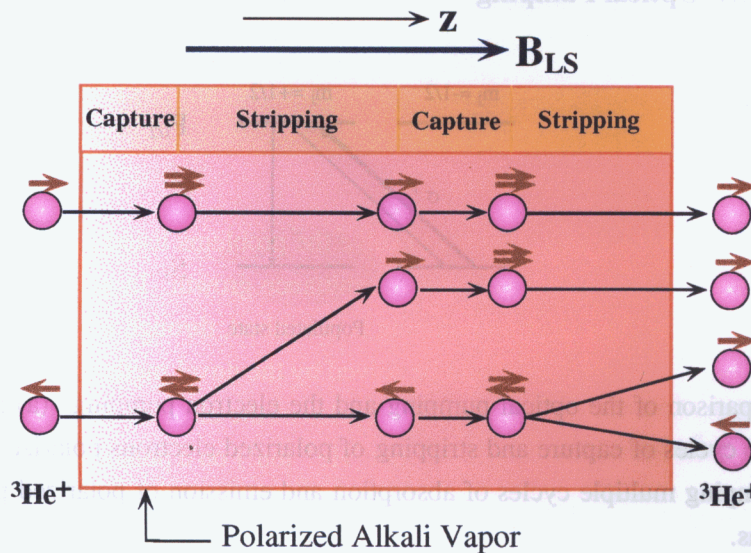
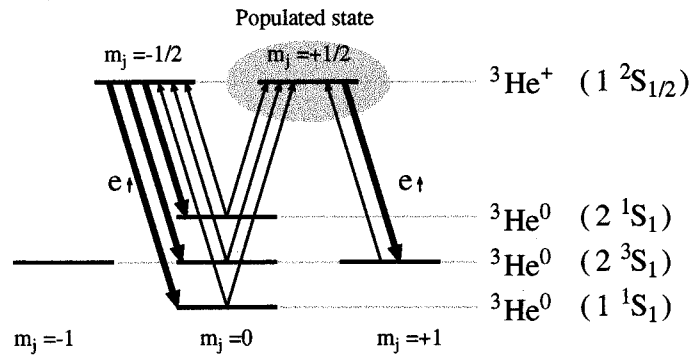


Figure 3.1: A schematic view of the electron pumping process.

excited  ${}^3\text{He}$  atom, followed by deexcitation either to the ground or metastable state by radiative decay. During further passage of the  ${}^3\text{He}$  atom through the polarized Rb vapor, the  ${}^3\text{He}$  is converted into a  ${}^3\text{He}^+$  ion again by an electron stripping process. Since either of the two electrons of the  ${}^3\text{He}$  atom can be stripped with approximately the same probability, the  ${}^3\text{He}^+$  ion is polarized by this process. If the Rb vapor thickness is large enough to allow repeated capture and stripping cycles, the polarization of the  ${}^3\text{He}^+$  ion increases and finally reaches a maximum value determined by the polarization of the Rb vapor. The multiple-collision processes mentioned above can be discussed in another way. An energy-level diagram for a  ${}^3\text{He}^+$  ion and a  ${}^3\text{He}$  atom is shown in Fig. 3.2, where the levels of the  ${}^3\text{He}$  atom with  $S=0$  (singlet levels, S) and with  $S=1$  (triplet levels, T) are indicated.

## (a) Electron Pumping



## (b) Optical Pumping

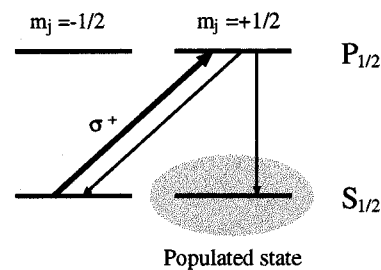


Figure 3.2: Comparison of the optical pumping and the electron pumping. (a) : In the electron pumping multiple cycles of capture and stripping of polarized electrons polarize  ${}^3\text{He}^+$  ions. (b) : In the optical pumping multiple cycles of absorption and emission of polarized photons polarize alkali-metal atoms.

An incident  ${}^3\text{He}^+$  ion first captures a polarized electron from an Rb atom and forms a  ${}^3\text{He}$  atom in an excited state. It then deexcites to the ground or metastable state of the  ${}^3\text{He}$  atom by a radiative decay. The radiative decay keeps the spin multiplet unchanged. Fig. 3.2 shows the energy levels of the  ${}^3\text{He}^+$  ion, including the two metastable levels and the ground level of the  ${}^3\text{He}$  atom. Other levels are not shown for simplicity. In the capture process, a  ${}^3\text{He}^+$  ion with an  $m_z = +\frac{1}{2}$  magnetic substate captures a polarized electron to form only a  ${}^3\text{He(T)}$  atom with  $m_z = +1$ , while a  ${}^3\text{He}^+$  ion with  $m_z = -\frac{1}{2}$  captures a polarized electron and forms either a  ${}^3\text{He(T)}$  or  ${}^3\text{He(S)}$  state with  $m_z = 0$ . When an electron stripping process takes place, a  ${}^3\text{He}^+$  ion is formed again. An electron stripping process for the  ${}^3\text{He(T)}$  atom with  $m_z = +1$  forms only a  ${}^3\text{He}^+$  ion with  $m_z = +\frac{1}{2}$ , while an electron stripping for the  ${}^3\text{He(T or S)}$  atom with  $m_z = 0$  forms a  ${}^3\text{He}^+$  ion with  $m_z =$  either

$+\frac{1}{2}$  or  $-\frac{1}{2}$  with the equal probability. Most of the  $^3\text{He}$  singlet atoms are in the ground level. The electron stripping process from this level is negligible small at our incident energy. After many repetitions of the capture and stripping processes, the  $^3\text{He}^+$  ions with  $m_z = +\frac{1}{2}$  predominate, that is, the electron of the  $^3\text{He}^+$  ion is polarized. The above scenario is almost identical to the principle of optical pumping if one replaces a polarized electron with a circularly polarized photon. This is a reason why we name our method “electron pumping”. It should be further mentioned that the electron pumping requires large collisions cross sections for both capture and stripping processes. In fact, this condition is satisfied for a fast  $^3\text{He}$  ion incident on a Rb target as discussed later.

### 3.1.3 Quantitative treatment of electron pumping

In what follows, a more quantitative discussion on the electron pumping is done by solving rate equations expressing the electron pumping process.

For this purpose the prescription given in the preceding work [33] has been modified. The rate equations were expressed in terms of matrices as shown below.

$$\frac{d}{d\pi}\mathbf{F} = (\varepsilon_+ \mathbf{R}_+ + \varepsilon_- \mathbf{R}_-) \mathbf{F}, \quad (3.3)$$

where,  $\pi$  is a Rb vapor thickness and  $\varepsilon_+$  and  $\varepsilon_-$  are

$$\varepsilon_+ = \frac{1 + P_{\text{Rb}}}{2}, \quad \varepsilon_- = \frac{1 - P_{\text{Rb}}}{2}, \quad (3.4)$$

where  $P_{\text{Rb}}$  is the Rb polarization. Here  $\mathbf{F}$  and  $\mathbf{R}_\pm$  are given below.

$$\mathbf{F} = \begin{pmatrix} H_{1/2}^+ \\ H_{-1/2}^+ \\ H_{t1} \\ H_{t0} \\ H_{t-1} \\ H_{s0} \end{pmatrix}, \quad \mathbf{R}_+ = \begin{pmatrix} -\sigma_{10} & \sigma_{se} & \sigma_{t1} & \frac{\sigma_{t1}}{2} & 0 & \frac{\sigma_{s1}}{2} \\ 0 & -\sigma_{10} - \sigma_{se} & 0 & \frac{\sigma_{t1}}{2} & \sigma_{t1} & \frac{\sigma_{s1}}{2} \\ \sigma_{10} & 0 & -\sigma_{t1} & \sigma_{sea} & 0 & 0 \\ 0 & \frac{\sigma_{10}}{2} & 0 & -\sigma_{t1} - \sigma_{sea} & \sigma_{sea} & 0 \\ 0 & 0 & 0 & 0 & -\sigma_{t1} - \sigma_{sea} & 0 \\ 0 & \frac{\sigma_{10}}{2} & 0 & 0 & 0 & -\sigma_{s1} \end{pmatrix} \quad (3.5)$$

$$\mathbf{R}_- = \mathbf{T} \mathbf{R}_+ \mathbf{T}^\dagger, \quad \mathbf{T} = \begin{pmatrix} 0 & 1 & 0 & 0 & 0 & 0 \\ 1 & 0 & 0 & 0 & 0 & 0 \\ 0 & 0 & 0 & 0 & 1 & 0 \\ 0 & 0 & 0 & 1 & 0 & 0 \\ 0 & 0 & 1 & 0 & 0 & 0 \\ 0 & 0 & 0 & 0 & 0 & 1 \end{pmatrix} \quad (3.6)$$

$H_j^+$  is the population of a  $^3\text{He}^+$  ion in the  $m_z=j$  states.  $H_{tj}$  is the population of a triplet  $^3\text{He}$  atom in the  $m_z=j$  states. and  $H_{s0}$  is a population of a singlet  $^3\text{He}$  atom.  $\sigma_{ij}$  is a cross section from  $i$  to

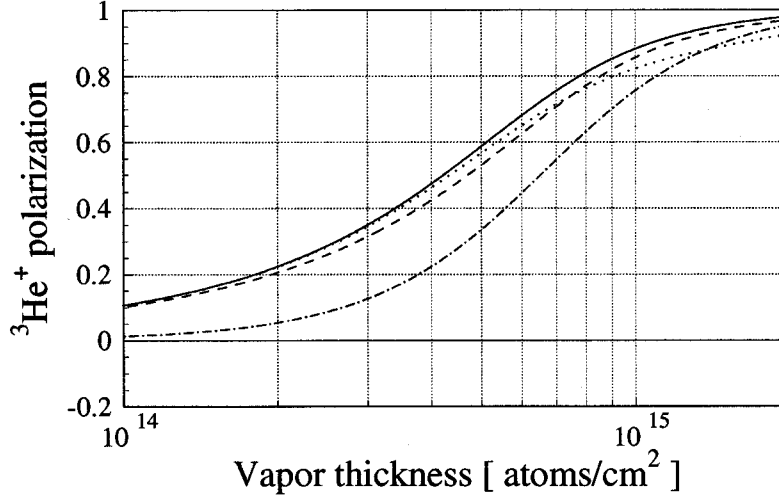


Figure 3.3: The polarization of the outgoing  ${}^3\text{He}^+$  ions calculated by the Runge-Kutta method using the rate Eqs. (3.3) as a function of the alkali-metal vapor thickness.

$j$  state where  $i=1$  is for a  ${}^3\text{He}^+$  ion,  $i=t(s)$  is for a triplet(singlet)  ${}^3\text{He}$  atom,  $j=0$  is for a  ${}^3\text{He}$  atom and  $j=1$  is for a  ${}^3\text{He}^+$  ion.  $\sigma_{se}$  is spin-exchange cross section for a  ${}^3\text{He}^+$  ion and  $\sigma_{sea}$  is that for a  ${}^3\text{He}$  atom.

The rate equations can be solved by the Runge-Kutta method. The calculation results with a few sets of the reasonable collision cross sections are shown in Fig. 3.3. The values of cross sections used here will be described at a later chapter. You can see that the  ${}^3\text{He}$  polarization increases with the increase of the alkali-metal vapor thickness. This is a characteristic feature of the electron pumping. At a vapor thickness of  $5 \times 10^{14}$  atoms/cm<sup>2</sup>, a certain amount of  ${}^3\text{He}^+$  ions begin to experience the one cycle of the electron capture and stripping processes and over the thickness of  $1 \times 10^{15}$  atoms/cm<sup>2</sup>, most amount of  ${}^3\text{He}^+$  ions experience one cycle of the charge exchange and some ions do the multiple cycles.

### 3.1.4 Effective nuclear charge and LS decoupling field

As discussed already, we used an LS decoupling field of about 2 T. This value was determined by assuming that an effective nuclear charge,  $Z_e$  felt by an electron captured by a  ${}^3\text{He}^+$  ion was approximately 1. In this subsection, we will examine the validity of this assumption.

In case of a hydrogen like atom the spin-orbit energy, i.e., LS coupling energy is given by

$$\delta E = \frac{\alpha^2 Z^4}{2n^3 l(l+1)} \quad \text{a.u.}, \quad (3.7)$$

where  $n$ ,  $l$ ,  $Z$  and  $\alpha$  are, respectively, a principal quantum number, an orbital angular momentum, a nuclear effective charge, and a fine-structure constant. Assuming that this energy is equal to a potential energy of an electron with a magnetic dipole moment in a magnetic field, i.e.,  $\mu_B B_{LS}$ ,  $B_{LS}$  is expressed in terms of  $n$ ,  $l$ ,  $Z$  and  $\alpha$ , as well.

Now, we assume that an electron orbital of a  ${}^3\text{He}^+$  ion is a 1s and captured orbitals are 1s, 2s, 2p, 3s, 3p, 3d, etc. Among these captured orbitals, the 1s, 2s, and 3s orbitals of the  ${}^3\text{He}^+$  ion do not induce the spin depolarization because the deexcitation processes from these orbitals do not accompany with the spin depolarization due to  $L=0$ . On the other hand, the deexcitation from other states in the  ${}^3\text{He}$  atom, more or less, accompanies with the spin depolarization.

Among these excited states, the most serious state which influences the spin depolarization is the 2p orbital because it has the largest LS interaction as shown in Eq. (3.7). In other words, if the external magnetic field is large enough to decouple the LS coupling scheme of the 2p state, then, the spin polarization would be completely conserved. Therefore it is of importance to estimate the LS decoupling field for the 2p orbital. For this purpose, it is necessary to know an effective nuclear charge,  $Z_e$  for the 2p orbital of the  ${}^3\text{He}$ .  $Z_e$  has been precisely calculable by using a variational method. The results are  $Z_e = 1.09$  for the  $2^3\text{P}$  (triplet) state, and  $Z_e = 0.97$  for the (singlet)  $2^1\text{P}$  state [34]. The transition from the (singlet)  $2^1\text{P}$  state to the ground  $1^1\text{S}$  state does not contribute to the electron pumping processes because the stripping cross section of the singlet state is negligible small. So further consideration on this component is omitted.

By using  $Z_e = 1.09$  for the  $2^3\text{P}$  (triplet) state, we can obtain a decoupling field  $B_{LS}$  as given by

$$B_{LS} = 1.10 \quad \text{T}. \quad (3.8)$$

Let me compare this value with that for the hydrogen 2p state as given by

$$B_{LS} = 0.7823 \quad \text{T}. \quad (3.9)$$

It is only  $\sim 1.4$  times larger than that of the hydrogen. Practically,  $1 \sim 2$  T is applied for the hydrogen OPPIS. Scaling this value to the  ${}^3\text{He}$  electron pumping, we would be required to use a decoupling field given by,

$$B_{LS} = 1.4 \sim 2.8 \quad \text{T}. \quad (3.10)$$

This is one of the greatest advantages for the  ${}^3\text{He}$  electron pumping since the  ${}^3\text{He}$  OPPIS required a decoupling field more than 16 T.

## 3.2 Relaxation of optically pumped Rb vapor

### 3.2.1 General view

As mentioned in the previous section, the electron pumping method uses repeated cycles of electron capture and stripping collisions under a strong magnetic field 2~ 3 T. To realize this method, it is necessary to create a highly polarized Rb vapor with much higher thickness (at least an order of magnitude) than that used in the OPPIS. In addition, it is also necessary to create a homogeneous distribution of the Rb polarization along the  $^3\text{He}$  beam trajectory in the collision region (a region of a Rb cell). However, behavior of the polarized alkali-metal vapor has not been thoroughly investigated for such an extremely thick Rb vapor under a strong magnetic field so far. To realize the polarized Rb vapor required for the electron pumping, we have initiated investigation of the fundamental behavior of the polarized Rb vapor in such an extreme condition. This investigation concerns with observation and theoretical understanding of the relaxation mechanism of the polarized Rb vapor.

In this subsection, we will give a general view of the relaxation mechanism of the polarized Rb vapor. The experimental procedures, experimental results and discussion will be presented in the later chapter.

The investigations of relaxation mechanisms of optically pumped alkali-metal vapors are of interest for fundamental quantum mechanics [35, 36, 37, 38, 39], and also for practical purposes such as the production of polarized ions [40, 41, 42] and gases [43, 44, 45]. In general, for the vapor in a closed cell, one expects that the Rb atom collisions with walls of the cell (wall relaxation) and with other atoms in the vapor (spin-disorientation) contribute to the depolarization. At low densities, the spin-disorientation effects are expected to be less important. For Rb atoms with collision cross section of  $\sim 10^{-16}$  atoms/cm<sup>2</sup>, one expects that spin-disorientations are negligible for densities less than  $10^{14}$  atoms/cm<sup>3</sup> [43]. In polarized ion sources, where one employs an open aperture on the wall, another depolarization mechanism becomes important. It is the phenomenon where the polarized atoms escape from the optical pumping cell and they are replaced by unpolarized atoms. This process, known as effusion, has not so far been examined in detail.

Motivation to study these phenomena has been stimulated by the recent developments of a new type of polarized  $^3\text{He}$  ion source based on electron pumping [46, 47, 33]. Here, one would like to produce a high density alkali-metal vapor of high degree of polarization in the environment of strong magnetic fields. Under these conditions, the commonly known wall relaxation and spin-disorientation processes may not cause much depolarization, but the effusion may result in depolarization of the vapor. Radiation trapping is another effect which might cause over-all decrease in the polarization. It might also render the polarization inhomogeneous around the pumping laser light. The present work was undertaken to investigate these processes in detail. We studied the relaxation rates of the Rb polarization from the time dependence of the Rb polarization for different magnetic fields ( $B = 1 - 5$  T), for temperature settings of the Rb cells ( $T_{\text{cell}} = 90 - 130$  °C), and as

the polarization distribution along the axis of the Rb cell is varied.

### 3.2.2 Relaxation models

#### Wall relaxation

The wall relaxation is simply understood qualitatively as follows [38, 39, 40, 42, 48]: When a polarized Rb atom sticks on a wall surface, the atom feels a local magnetic field,  $b$ , produced by the wall during a sticking time,  $\tau_s$ , in addition to a magnetic field,  $B$ . The local field,  $b$  is randomly oriented with a correlation time,  $\tau_c$ . Since the electron spin of the Rb atom precesses around the time dependent effective field composed of  $b$  and  $B$ , the depolarization of electron spin is induced. Assuming that a mean flight time of the Rb atom between wall collisions is  $\tau_v$ , the fraction of time that the local field acts on the Rb atom is  $\tau_s/(\tau_s + \tau_v)$ . Quantitatively, the wall relaxation rate is given by

$$T_{ws}^{-1} = C \frac{1}{1 + \left(\frac{e\tau_c B}{m}\right)^2}, \quad (3.11)$$

$$C = \frac{2}{3} \frac{\tau_s}{\tau_s + \tau_v} \gamma_s^2 b^2 \tau_c, \quad (3.12)$$

where  $eB/m$  is the electron cyclotron frequency, and  $\gamma_s$  is gyromagnetic ratio of the electron. The sticking time,  $\tau_s$  is given as

$$\tau_s = \tau_0 \exp(E_a/kT_{\text{cell}}), \quad (3.13)$$

where  $E_a$  is an adsorption energy,  $\tau_0$  is a constant with a typical value,  $\tau_0 \simeq 10^{-12}$  s [49].

#### Relaxation due to effusion

The relaxation due to an effusion effect is qualitatively understood as follows: The effusion process is due to a combination of migration of Rb atoms between the pumping and the outside regions. Fig. 3.4 is a pictorial depiction of the diffusion processes, resulting in a change of polarized Rb atom density by effusion. A polarized Rb atom can migrate away from the pumping region to the side without significant collisions with the cell walls (Process A in Fig. 3.4), or it might escape into the outer tube through one of the four slots (Process B). It is also possible that the pumping region is enriched by unpolarized Rb atoms migrating from the outer tube via the slots (Process C). The net effect is an apparent increase in the relaxation rate. Below is a quantitative description of the effusion process.

We assume that a Rb atom is an elastic ball moving back and forth with a velocity,  $v$ , in a cylindrical cell whose length, radius, and cross section are  $L$ ,  $R$  and  $S$ , respectively. Each end of the cylindrical cell has a small hole with an area,  $S'$ . Then, the loss rate of the polarized Rb atom on the cell end per one collision is  $S'/S$ . On the other hand, the number of collisions with the cell

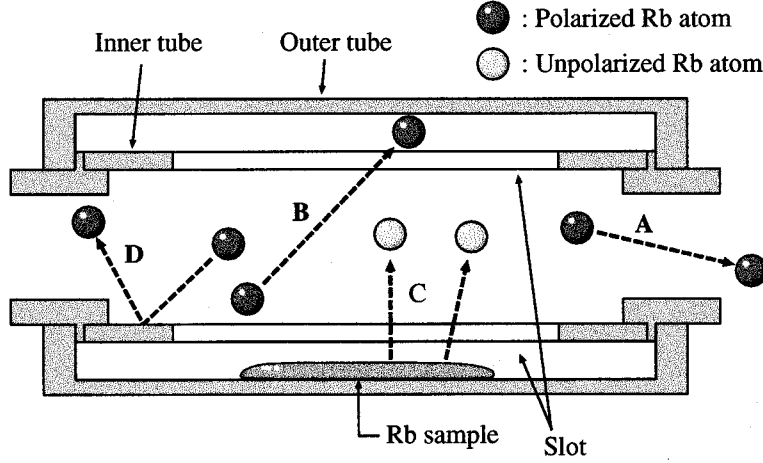


Figure 3.4: A schematic picture showing an effusion process. “A” and “B” are polarized Rb atoms escaping into the outer region. “C” is an unpolarized Rb atoms migrating into the outer region. “D” is deflection by bouncing against cell walls.

end per one second is  $v/L$ . Therefore, the number of the Rb atoms surviving after  $t$  second is given by

$$\left(1 - \frac{S'}{S}\right)^{vt/L}. \quad (3.14)$$

A similar equation holds for the radial direction. If we approximate the cylindrical cell to a rectangular parallelepiped with dimensions  $L \times 2R \times 2R$ , the Rb polarization after  $t$  seconds is given by,

$$P(t) \simeq P_0 \left(1 - \frac{S'}{S}\right)^{vt/L} \times \left(1 - \frac{C'}{C}\right)^{2vt/2R} = P_0 e^{-t/T_{es}}. \quad (3.15)$$

We approximate  $v$  by a mean velocity along a direction in Maxwellian distribution,  $\bar{v} = \sqrt{2kT_{\text{cell}}/\pi M}$ , where  $k$  is the Boltzmann constant,  $M$  is Rb mass. Consequently, the relaxation rate,  $T_{es}^{-1}$  is given by,

$$T_{es}^{-1} = -\sqrt{\frac{2k}{\pi M}} \left( \frac{\ln(1 - S'/S)}{L} + \frac{\ln(1 - C'/C)}{R} \right) \sqrt{T_{\text{cell}}}. \quad (3.16)$$

The significance of this formula is that the relaxation due to the effusion is simply determined by the cell temperature and a geometry of the Rb cell, i.e.,  $S'/S$ ,  $C'/C$ ,  $L$ , and  $R$ . Though obvious, it is worth mentioning that the effusion process does not depend on  $B$ . This simple model does not include the scattering angular distribution of the Rb atom by the walls for an oblique entry [41]. To better account for the data, we carried out a Monte Carlo simulation allowing for the angular

distribution of the scattered particle. The distribution is taken to be proportional to  $\cos \theta$ , where  $\theta$  is the scattering angle with respect to the normal to the wall surface [41].

The above two processes are enough to describe the slow component of the relaxation rates. As to be discussed below, the fast component necessitates another physics phenomenon, viz. localized sheath formation. It should be remarked that a fast component was observed in the earlier works [50, 51], which used high density Rb vapor as is the case in the present work. It is very conceivable that the fast component has its origins in localized microscopic processes such as radiation scattering and absorption. To further examine this aspect, we carried out a Monte Carlo simulation, the details of which are presented in the Appendix A. A brief discussion of the physics of the simulation follows.

We assume that there exists, along the path of the pumping laser beam, a localized sheath of Rb vapor with a high degree of polarization. When the pumping laser is switched off, this sheath of radius,  $r$ , begins to expand with a velocity  $v$  due to the thermal motion of the Rb atom. The sheath radius at a time,  $t$ , is expressed by

$$r_t = r_0 + vt. \quad (3.17)$$

Assuming that the Rb polarization  $P_t$  is uniform inside the sheath,  $P_t$  is given by

$$P_t r_t^2 = P_0 r_0^2, \quad (3.18)$$

where  $P_0$  and  $r_0$  are the Rb polarization and radius for the sheath, when the laser is switched off. Inserting Eq. (3.17) into Eq. (3.18),  $P_t$  is expressed as a function of time as

$$P_t = P_0 \frac{r_0^2}{(r_0 + vt)^2} \quad (3.19)$$

Assuming that the relaxation time,  $T_f$  is defined by the time that  $P_t/P_0 = 1/e$  the relaxation rate,  $T_f^{-1}$  for the fast component is given by

$$T_f^{-1} = \frac{v}{r_0(\sqrt{e}-1)} = \sqrt{\frac{2k}{\pi M}} \frac{1}{\sqrt{e}-1} \frac{\sqrt{T_{\text{cell}}}}{r_0}. \quad (3.20)$$

This equation suggests that the relaxation by this process is determined only by the Rb cell temperature,  $T_{\text{cell}}$ , and the initial radius of the sheath,  $r_0$ .

### 3.3 Problems on the beam profiles created by the electron pumping

In this section, we discuss important subjects which are related to quality of the polarized  $^3\text{He}$  beam produced by the electron pumping method.

The electron pumping method uses repeated cycles of electron capture and stripping collision of a  $^3\text{He}$  ion/atom in a strong magnetic field. If a  $^3\text{He}^+$  ion incident on a Rb vapor with an oblique

entry relative to the z-axis, i.e., the direction of the magnetic field, the beam trajectory shows a screw motion by the presence of a Lorentz force. In our previous work, we developed a Monte Carlo simulation program to evaluate this effect particularly from the view point of the beam emittance growth [52]. One of the important features found through the above analysis was that the beam emittance growth was suppressed. This is favorable for designing a practical polarized  $^3\text{He}$  ion source based on the electron pumping method.

Another important subject to be examined is a spatial distribution of the  $^3\text{He}$  polarization produced by the electron pumping method. It has been, for a long time, suggested that there is an inhomogeneity of the polarization caused by repeated multiple electron capture and stripping collisions in a strong magnetic field. However, no one has ever investigated this problem. In the present work, we have done a Monte Carlo simulation to evaluate this effect.

### 3.3.1 Creation of a polarization hole

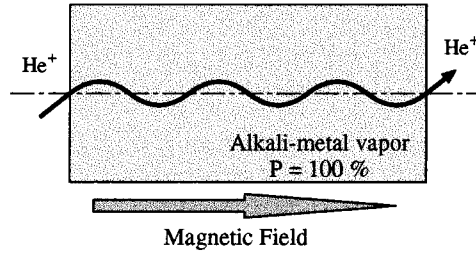
An essence of this effect is that a number of repeated cycles of the electron capture and stripping process in a strong magnetic field is practically not infinite but only a few times. Of course, a spatial distribution of the  $^3\text{He}^+$  polarization as a result of the electron pumping should be homogeneous if all  $^3\text{He}^+$  ions are incident on a Rb vapor cell parallel to the z-axis, i.e. the direction of the magnetic field because they are not influenced by a Lorentz force. On the other hand, if incident  $^3\text{He}^+$  ions have oblique entries with respect to the z direction, their beam trajectories become dispersive because they are influenced by a magnetic field in case they are  $^3\text{He}^+$  ions and they are not influenced by a magnetic field in case they are neutral atoms. As a result, this effect is expected to induce a spatial inhomogeneity of the  $^3\text{He}$  polarization, i.e., “polarization hole”, which was named by us. The generation mechanism of this hole is schematically shown in Fig. 3.5.

The formation of the polarization hole may depend strongly on the Rb vapor thickness and less on a strength of the magnetic field: When an alkali-metal vapor thickness is not so thick as to be equilibrated, in other words, the process is expressed by a small number of the electron capture and stripping processes, a parallel component has a large fraction of the collisionless  $^3\text{He}^+$  ions having no polarization, while an oblique component will deviate from their straight trajectories and disperses by a Lorentz force when the electron capture processes are induced, which results in the expectation that the central region of the output  $^3\text{He}^+$  beam has no polarization and the surrounding region has a large polarization. If the Rb vapor thickness is increased, i.e., the multiple electron capture and stripping collisions are equilibrated, such a polarization hole is expected to disappear.

On the other hand, the magnetic field dependence of the polarization hole is less pronounced. In this case a point is a cyclotron radius determined by the  $^3\text{He}^+$  ion velocity and the magnetic field. Accordingly, the total radius of the polarization hole will hopefully determined by a radius of the parallel component plus a cyclotron radius. Since the parallel radius is usually much larger than the cyclotron radius, its dependence on the magnetic field is less important.

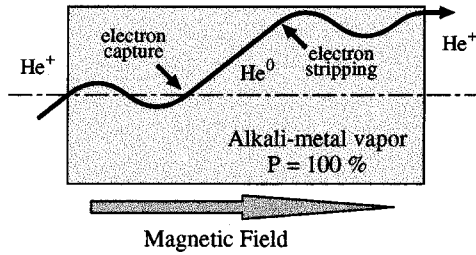
To treat this phenomenon more quantitatively, we have carried out a Monte Carlo simulation

Process 1: Without charge exchange



Polarization : 0  
Beam size : Small

Process 2 : With charge exchange



Polarization : High  
Beam size : Large

Figure 3.5: Schematic view of generation mechanism of the polarization hole.

as shown in the next subsection. Before going into the detail, we define following parameters to describe the property of the polarization hole.

1.  $d_{\text{hole}}$  : Depth of the hole, defined by  $(P_{\text{ext}} - P_{\text{hole}})/P_{\text{ext}}$ .
2.  $r_{\text{hole}}$  : Radius of the hole, where  $P(r_{\text{hole}}) = \frac{1}{2}(P_{\text{ext}} - P_{\text{hole}})$ .

### 3.3.2 Monte Carlo simulation

To discuss the phenomenon simply, we assume an ideal condition as shown Fig. 3.6. A magnetic field is uniformly 2 T with a sharp edge. A Rb vapor cell has a bore diameter of 1 cm and a length of 30 cm. A Rb vapor is uniformly distributed throughout the interior of the cell and no Rb vapor is present outside of the cell. A Rb vapor is uniformly polarized inside the cell with a full polarization.

Unpolarized  ${}^3\text{He}^+$  ions are incident on the Rb vapor cell. We assume that through the multiple collisions  ${}^3\text{He}^+$  ionic states consist of three components, i.e., a singly charged  ${}^3\text{He}^+$  ion, a singlet and a triplet  ${}^3\text{He}$  atom, where formation of components such as a doubly charged  ${}^3\text{He}^{2+}$  ion or a negative  ${}^3\text{He}^-$  ion are ignored because of small cross sections for formation of these components.

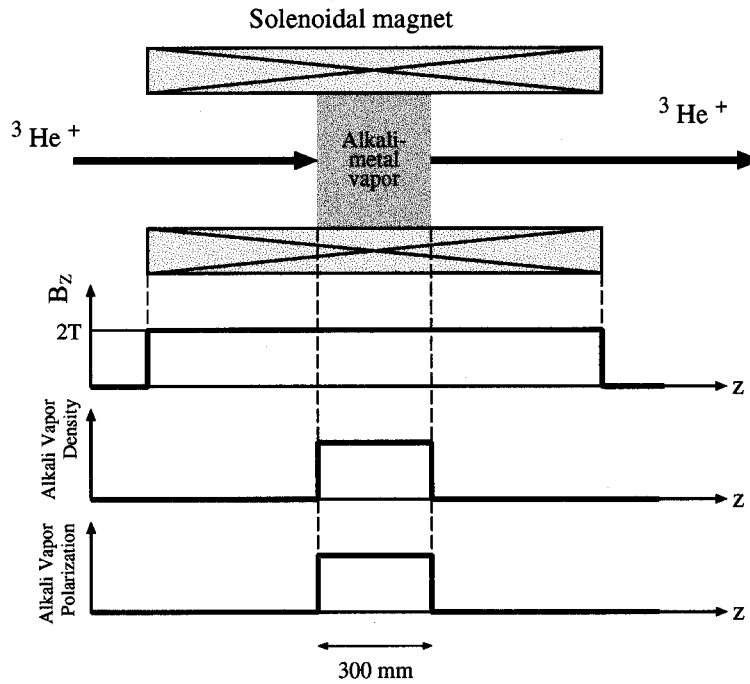


Figure 3.6: An idealized geometry assumed in the present Monte Carlo simulation. An alkali-metal vapor with a length of 300 mm is distributed at the center of the solenoidal coil. The vapor density and polarization uniformly distributes throughout the region where the vapor is distributed. The 2-T magnetic field is provided by a solenoidal coil and the magnetic field is also uniformly distributed throughout the interior of the solenoidal magnet.

In the Monte Carlo simulation we assume that the  ${}^3\text{He}^+$  ions are incident on a Rb vapor with a kinematic energy of 19 keV because we have done the measurement of the electron pumping at this energy. In addition, the cross sections of electron capture and stripping between  ${}^3\text{He}^+$  ions and the Rb vapor are well known as shown below. A cross section of the electron capture for singly charged ion is  $\sigma_{10} = 0.418 \times 10^{-14} \text{ cm}^2$  and the electron stripping cross section for the triplet atom is  $\sigma_{t1} = 0.108 \times 10^{-14} \text{ cm}^2$  and for the singlet one is  $\sigma_{s1} = 0.0012 \times 10^{-14} \text{ cm}^2$ .

We do not take the effect of the scattering angle due the electron stripping and capture processes into account because of their smallness ( $< 0.1^\circ$ ).

### 3.3.3 Various facet of the polarization hole derived from the Monte Carlo simulation

Typical simulation results are shown in Fig. 3.7 and 3.8 using the parameters tabulated in Table 3.1. It is found that a polarization is small at the center of beam axis. This is “polarization hole” as suggested before.

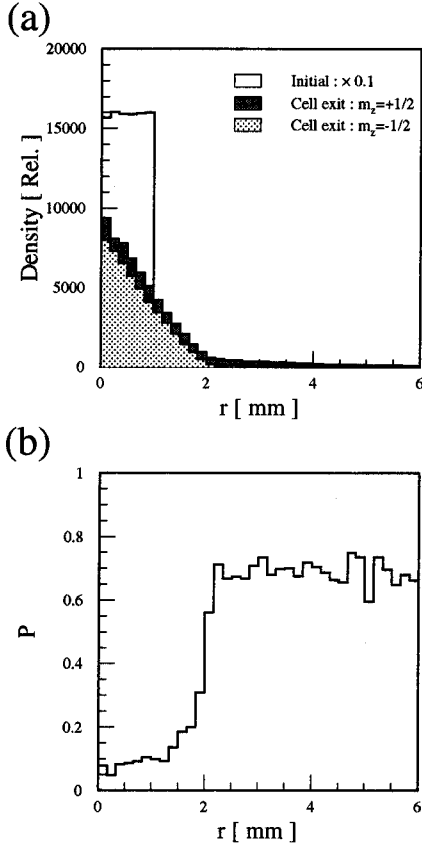


Figure 3.7: Typical beam intensity and polarization distributions plotted as a function of  $r$  calculated by the Monte Carlo simulation. (a)  $r$ -distribution of  ${}^3\text{He}^+$  ions. Incident beam has  $r = 1$  mm (no shaded histogram. The histogram is multiplied by 0.1). An outgoing beam spatially spreads due to the cyclotron motion and multiple charge exchange collisions under a strong magnetic field in addition to the initial spreading. A  ${}^3\text{He}^+$  ion beam with  $m_z = +1/2$  (thick shaded histogram) spatially spreads more than that with  $m_z = -1/2$  (thin shaded histogram) due to the multiple charge exchange collisions. (b)  $r$ -distribution of the polarization of  ${}^3\text{He}^+$  ion. The polarization shows small values ( $\sim 0.1$ ) at  $r < 2$  mm, while it shows large values ( $\sim 0.75$ ) at  $r > 2$  mm. The polarization dip found in this figure is called “polarization hole”.

To study properties of this polarization hole in more detail, the dependences of  $r_{\text{hole}}$  and  $d_{\text{hole}}$  on the external magnetic field, on the initial beam emittance, and on the alkali-metal vapor thickness are investigated.

The parameters,  $r_{\text{hole}}$  and  $d_{\text{hole}}$  are evaluated by the least square fittings of the results obtained from the Monte Carlo simulation, where a fitting function is assumed by

$$P(r) = P_{\text{ext}} - \frac{P_{\text{hole}}}{1 + \exp\{(r - r_{\text{hole}})/a\}}, \quad (3.21)$$

where  $a$  is a diffuseness parameter and  $P_{\text{ext}}$ ,  $P_{\text{hole}}$  and  $d_{\text{hole}}$  are those defined in the beginning of this section. where  $r$  is a radial distance from the center of beam axis.

### Magnetic field dependence

Fig. 3.11 shows diffuseness,  $P_{\text{ext}}$ ,  $P_{\text{hole}}$ ,  $r_{\text{hole}}$ , and  $d_{\text{hole}}$  plotted as a function of  $B_z$ . Interestingly,  $r_{\text{hole}}$  shows a damped oscillation with respect to  $B_z$ . This is explained qualitatively as follows. A phase of the cyclotron motion for a  ${}^3\text{He}^+$  ion changes at the exit of the Rb vapor cell since the

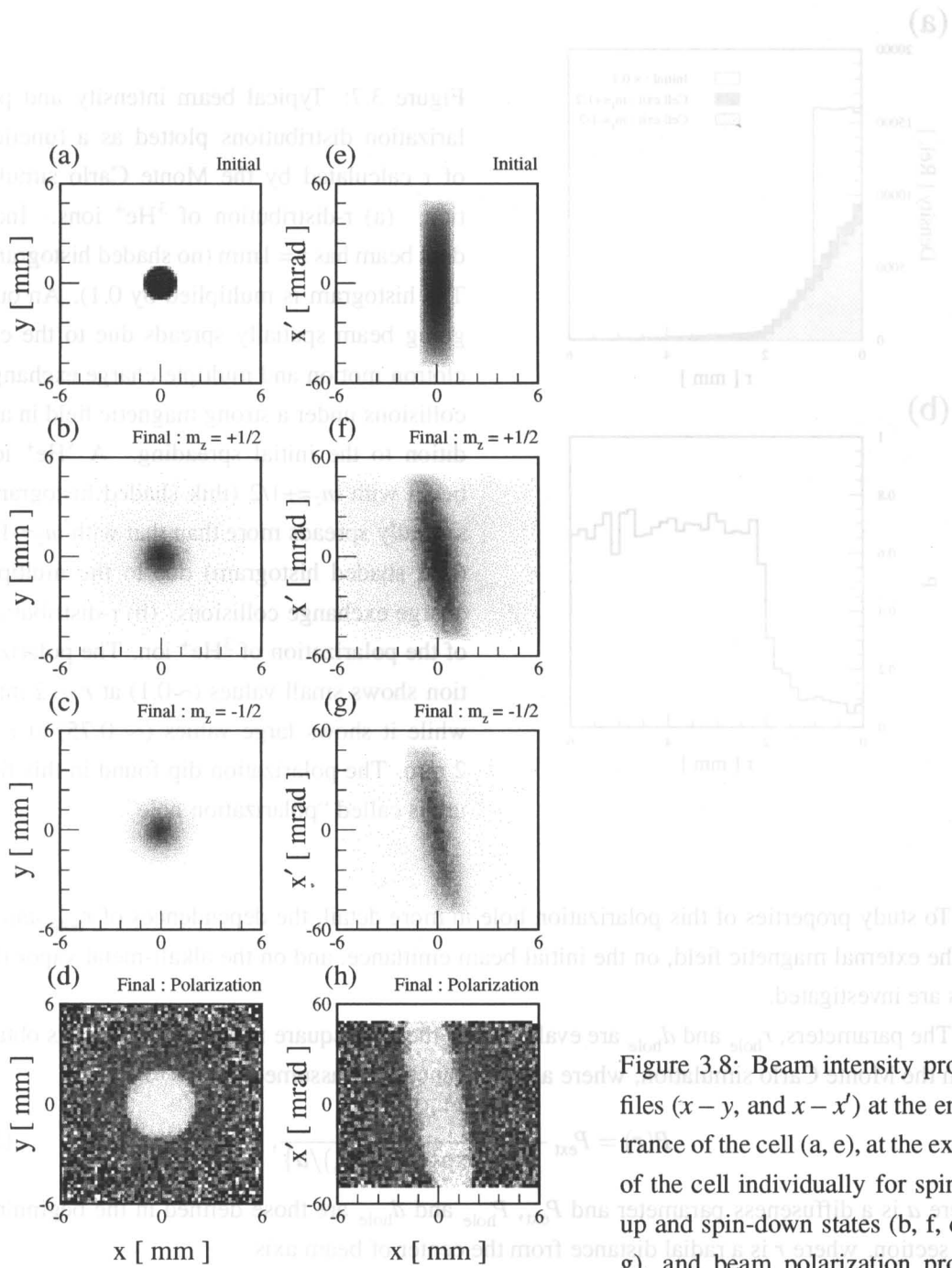


Figure 3.8: Beam intensity profiles ( $x - y$ , and  $x - x'$ ) at the entrance of the cell (a, e), at the exit of the cell individually for spin-up and spin-down states (b, f, c, g), and beam polarization profiles (d, h)

$r_{\max}$	1 mm
$r'_{\max}$	50 mrad
$B_z$	2 T
Alkali-metal vapor thickness	$5.0 \times 10^{14}$ atoms/cm <sup>2</sup>
Projectile energy	19 keV

Table 3.1: Typical parameters used on the Monte Carlo simulation for the polarization hole

cyclotron frequency linearly changes as  $B_z$  and a cyclotron radius reduces inversely proportional to  $B_z$ .

### Beam emittance (Angular spreading) dependence

$r_{\text{hole}}$  is proportional to the beam spreading angle. This is because a cyclotron radius is a linear function of a beam angle with respect to the direction of the magnetic field.

### Spot size dependence

$r_{\text{hole}}$  directly depends on an initial spot size. This is found in Fig. 3.3.4. On the other hand, it is found that  $d_{\text{hole}}$  decreases as  $r$  decreases. This is simply because the beam density decreases owing to an increase of the beam radius.

### Rb vapor thickness dependence

In Fig. 3.12, it is found that  $d_{\text{hole}}$  decreases as the Rb vapor thickness increases. Since a fraction of ions which experience no charge exchange collisions and experiences the collisions more than twice depends on an alkali-metal vapor thickness,  $d_{\text{hole}}$  depends on an alkali-metal vapor thickness as well.

### Spot size dependence under constant emittance

The simulated results under the constant emittance,  $50\pi$  mm·mrad are shown in Fig. 3.13. It is found that  $P_{\text{hole}}$  asymptotically close to the result from the rate equation (3.3) with increase of the spot size. This means that to eliminate the hole effect, it is preferable that the beam spreading angle is small under the constant emittance. The decrease of  $r_{\text{hole}}$  at small  $r$  is due to a decrease of  $r'$ .

### 3.3.4 Analytical formalism for $r_{\text{hole}}$ and $d_{\text{hole}}$

In this section, we will discuss how to express the results of the Monte Carlo simulation in terms of analytical functions for  $r_{\text{hole}}$  and  $d_{\text{hole}}$ . This is important to understand physics underlying this phenomenon.

Firstly, we try to formulate  $r_{\text{hole}}$ . From the results of the simulation,  $r_{\text{hole}}$  is found to depend on  $r$ ,  $r'$  and  $B_z$ .  $r'$  and  $B_z$  change the cyclotron radius of the projectile. Consequently,  $r_{\text{hole}}$  is written as a function of  $r$  and the cyclotron radius,  $r_L$  as formulated below.

$$r_{\text{hole}} = r_0 + r_L, \quad (3.22)$$

$$r_L = \{1 + \cos(\theta - \pi)\} \frac{mv_0 r'}{qB_z}, \quad (3.23)$$

$$\theta = \omega_c z / v_z, \quad (3.24)$$

$$\omega_c = qB_z / m. \quad (3.25)$$

where  $v_0$  and  $q$  are the projectile velocity and charge, respectively.

Next,  $d_{\text{hole}}$  is mentioned. To express this parameter, the spreading radius caused during the one period of the electron capture and electron stripping process is considered. This is approximated by

$$r \sim r_0 + r_L + r_{ce}, \quad (3.26)$$

where  $r_{ce}$  is the spreading radius when an incident  ${}^3\text{He}^+$  ion experiences only one period of the electron capture and stripping in an infinite magnetic field as expressed by ( see appendix D ).

$$r_{ce} = \frac{4}{3} R_0 \theta_{\text{max}}, \quad (3.27)$$

where

$$R_0 = \frac{C_2 L - 2 + (C_2 L + 2)e^{-C_2 L}}{C_2(C_2 L - 1 + e^{-C_2 L})} \quad (3.28)$$

$$C_1 = \sigma_{10} \sigma_{t1} e^{-\sigma_{10} L} \quad (3.29)$$

$$C_2 = \sigma_{t1} - \sigma_{10}. \quad (3.30)$$

It is expected that  $d_{\text{hole}}$  depends on the ratio of the  ${}^3\text{He}^+$  ions which experience the charge exchange collisions and no collisions, respectively. These densities are given by

$$\rho_0 = \frac{F_0}{\pi r_{\text{hole}}^2}, \quad (3.31)$$

$$\rho_2 = \frac{F_2}{\pi r_2^2}. \quad (3.32)$$

Here,  $\rho_0$  and  $\rho_2$  are the density of ions which experience no charge exchange collisions and experiences the collisions more than twice, respectively.  $F_0$  and  $F_2$  are an ion fraction at the exit of the Rb vapor cell and meanings of the subscript are the same as used for  $\rho$ . From the above equations,  $P_{\text{hole}}$  is given by

$$P_{\text{hole}} = \frac{P_{\text{ext}}}{1 + \frac{\rho_0}{\rho_2}}, \quad (3.33)$$

and  $d_{\text{hole}}$  is

$$d_{\text{hole}} = 1 - \frac{1}{1 + \frac{\rho_0}{\rho_2}} \quad (3.34)$$

$$= 1 - \frac{1}{1 + \frac{F_0 r_2^2}{F_2 r_{\text{hole}}^2}}. \quad (3.35)$$

With the above equations,  $d_{\text{hole}}$  and  $r_{\text{hole}}$  can be expressed by analytical forms as shown below;

In Fig. 3.3.4- 3.12 the results of Monte Carlo simulation and the numerical results of the analytical estimations are compared as functions of  $r$ ,  $r'$ ,  $B_z$  and the alkali-metal vapor thickness, where analytical results are plotted by the solid curves.

From this comparison, it can be seen that our analytical formalisms are roughly reproducing the results of the Monte Carlo simulation. This, in turn, suggests that the polarization hole is produced as a result of the beam size growth due to the charge exchange process.

A sizable deviation of the analytical calculations from the Monte Carlo simulation may suggest that in this analytical calculation, the total polarization radius is a superposition of an initial beam radius, a cyclotron radius, and a spreading radius caused by charge exchange processes.

From the above analytical equations and the simulation it is found that if a spreading of  $\theta$  is small at the entrance of the Rb vapor cell, the depth of the polarization hole becomes small, while if an incident beam spot size has a small radius, the radius of the polarization hole become small too, but its depth becomes deep. In conclusion, it is desirable for a practical polarized  $^3\text{He}^+$  ion source that an incident  $^3\text{He}^+$  beam is as possible as coaxial at the region of the vapor cell.

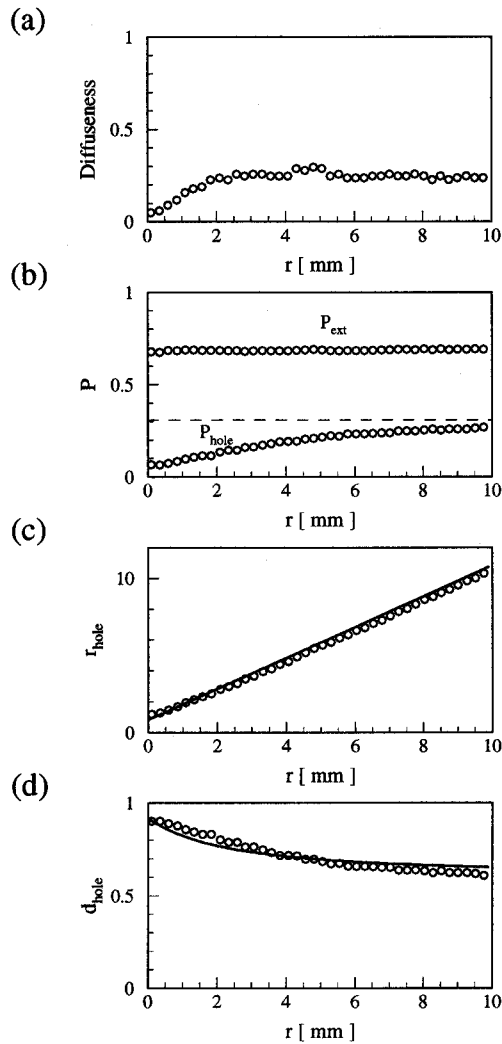


Figure 3.9: Initial beam size ( $r$ ) dependence of parameters characterizing output beam. (a) diffuseness, (b) polarization for the hole region and for the exterior region, (c)  $r_{hole}$ , and (d)  $d_{hole}$ . The solid curves are calculated results by the analytical method. The dot-dashed curve in (b) are calculated results by the rate Eqs. (3.3).

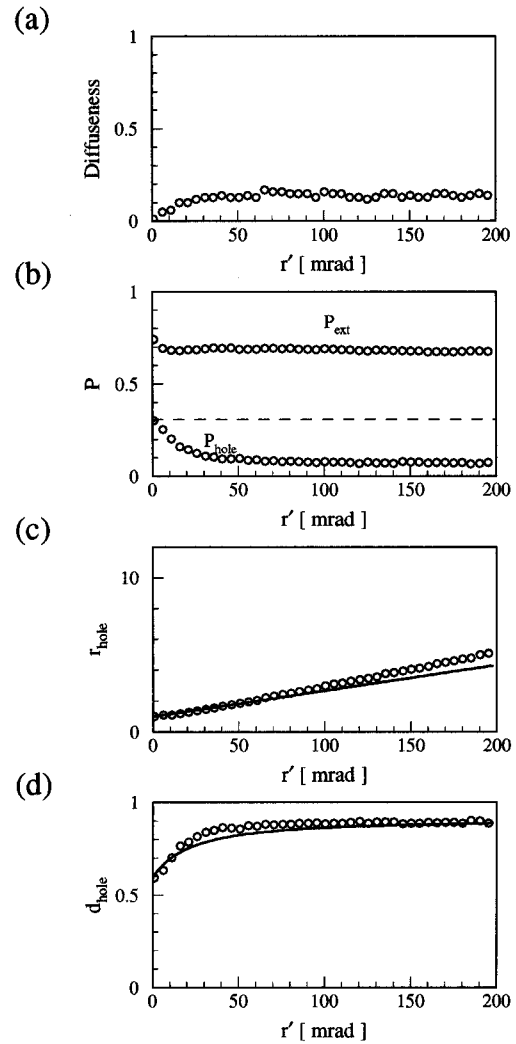


Figure 3.10: Initial beam spreading angle ( $r'$ ) dependence of parameters characterizing output beam. (a) diffuseness, (b) polarization for the hole region and for the exterior region, (c)  $r_{hole}$ , and (d)  $d_{hole}$ . The solid curves are calculated results by the analytical method. The dot-dashed curve in (b) are calculated results by the rate Eqs. (3.3).

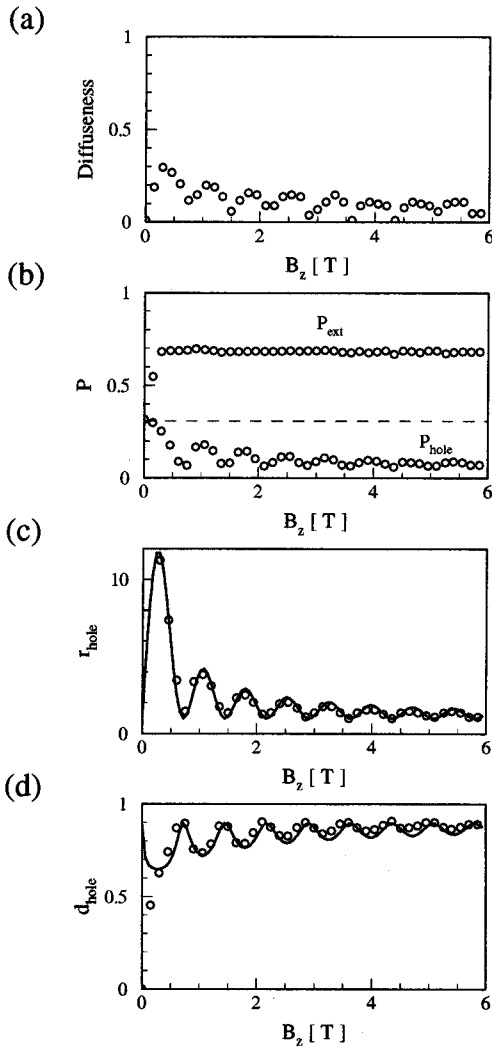


Figure 3.11: Magnetic flux density ( $B_z$ ) dependence of parameters characterizing output beam. (a) diffuseness, (b) polarization for the hole region and for the exterior region, (c)  $r_{hole}$ , and (d)  $d_{hole}$ . The solid curves are calculated results by the analytical method. The dot-dashed curve in (b) are calculated results by the rate Eqs. (3.3).

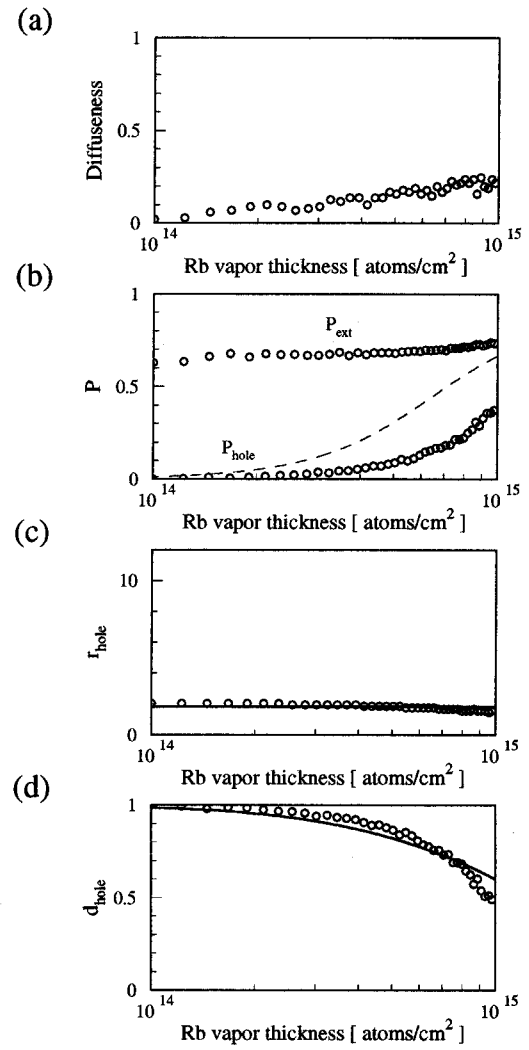


Figure 3.12: Alkali-metal vapor thickness dependence of parameters characterizing output beam. (a) diffuseness, (b) polarization for the hole region and for the exterior region, (c)  $r_{hole}$ , and (d)  $d_{hole}$ . The solid curves are calculated results by the analytical method. The dot-dashed curve in (b) are calculated results by the rate Eqs. (3.3).

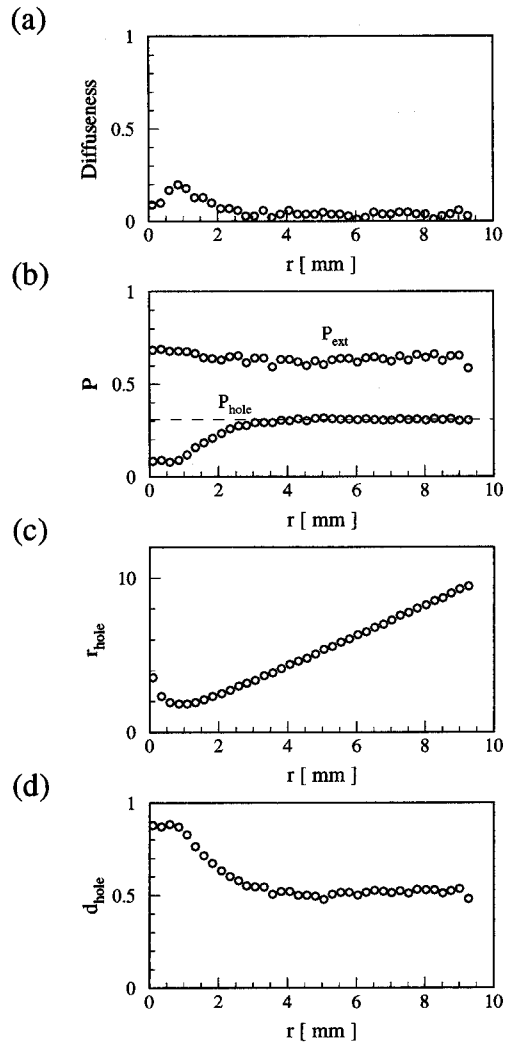


Figure 3.13:  $r$  dependence of parameters characterizing output beam under the condition that the emittance is constant ( $50\pi$  mm·mrad). (a) diffuseness, (b) polarization for the hole region and for the exterior region, (c)  $r_{\text{hole}}$ , and (d)  $d_{\text{hole}}$ . The dot-dashed curve in (b) are calculated results by the rate Eqs. (3.3).

## Chapter 4

# Experimental Apparatus

### 4.1 Layout of the electron pumping polarized $^3\text{He}$ ion source

A schematic view of the electron pumping polarized  $^3\text{He}$  ion source is shown in Fig. 4.1. This ion source consists of many parts; a duoplasmatron ion source for production of an unpolarized  $^3\text{He}^+$  ion, a high intensity laser system for optical pumping of a Rb vapor, a Rb vapor cell where multiple electron capture and stripping collisions occur, an optical system to measure Faraday rotation angles for determining a Rb polarization and thickness, a superconducting magnet to produce an axial magnetic field strong enough to decouple the LS coupling, a pair of Helmholtz coils used for preventing depolarization by an external disturbing field, a beam-foil polarimeter system used for measuring the  $^3\text{He}$  polarization, and a beam transport system. Each system will be described in the following subsections in more detail.

#### 4.1.1 Beam transport system

$^3\text{He}^+$  ions produced by the duoplasmatron ion source is extracted at 19 kV and momentumly analyzed by a sector magnet. These ions are transported to the Rb cell located in the center of the superconducting solenoidal magnet so that they might be focused on the center of the Rb cell, where repeated cycles of electron capture and stripping collisions occur. The  $^3\text{He}^+$  ions emerging out of the Rb vapor cell are, then, energetically analyzed by an electrostatic deflector with a  $90^\circ$  bending angle and finally introduced to the beam-foil polarimeter.

To enable the above beam transportation, we used three focusing elements, two electrostatic quadrupole doublet lenses, and an electrostatic quadrupole triplet lens.

To determine an optimized arrangement of the elements of the beam optics, a calculation of the ion beam optics was carried out by using the computer programs for a beam transport, GIOS [53] and COSY [54]. The GIOS program was used from the duoplasmatron ion source to an exit of the superconducting solenoidal magnet. The more handy program, COSY was used for a calculation of the region after the exit of the solenoidal magnet. The beam optics was designed so that the  $^3\text{He}$

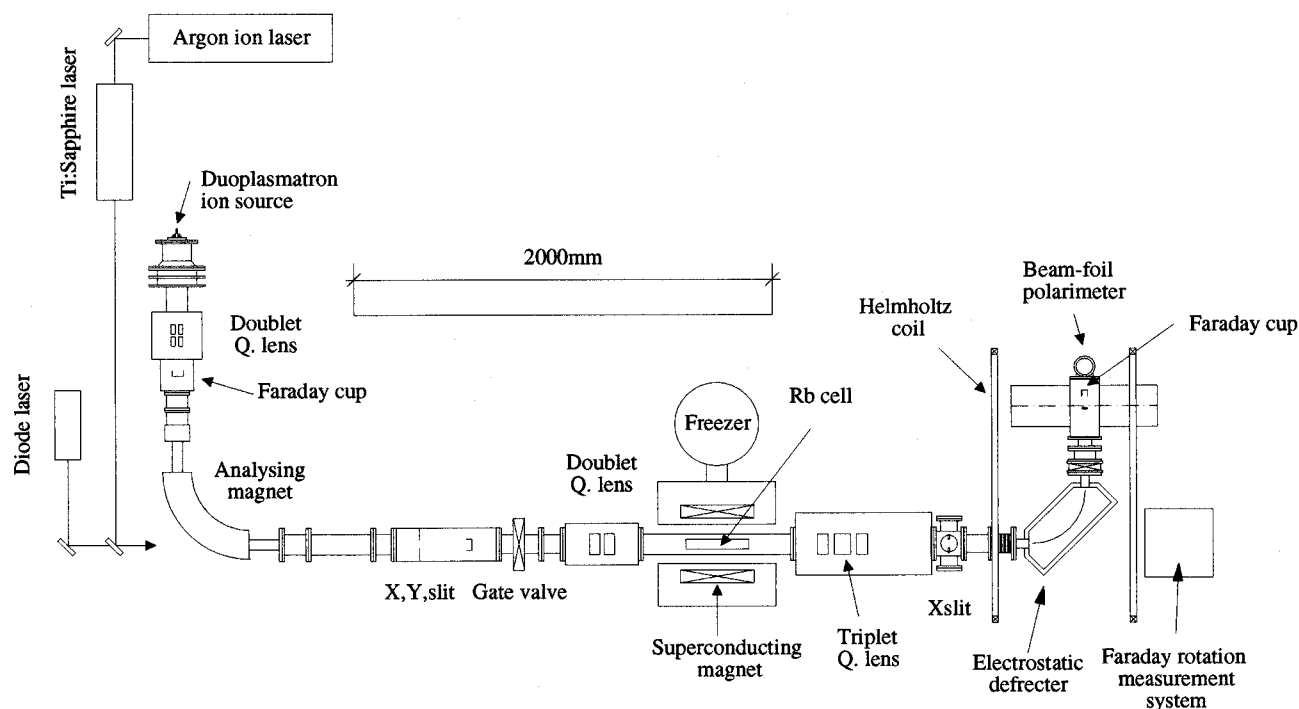


Figure 4.1: A set up of the electron pumping polarized  $^3\text{He}$  ion source

beam focused on the center of the Rb cell. To avoid depolarization by the optical elements, the focusing elements lower stream of the Rb cell consisted of only electrostatic focusing elements instead of the magnetic ones. In Fig. 4.1.1, a designed ion beam optics is shown.

An initial condition of the ion beam was assumed that a beam spot size was  $\pm 1$  mm and a spreading angle was  $\pm 1^\circ$ . Ions extracted from the duoplasmatron were defocused by the doublet Q. lens and after passing the analyzing magnet, they were focused on a slit 1. Then, they were focused on the Rb cell center by the doublet Q. lenses and the superconducting magnet, inside of which the Rb cell was located. Leaving the Rb vapor cell, the ions were focused by the triplet Q. lenses on a slit 2 and finally they were focused on a target of a polarimeter.

#### 4.1.2 Duoplasmatron ion source

$^3\text{He}^+$  ions are produced by a duoplasmatron ion source. This type of ion source can produce dominantly singly charged  $^3\text{He}^+$  ions.

A layout of this ion source is shown in Fig. 4.3. Thermal electrons are emitted from a cathode heated by a tungsten filament. The cathode is coated with a Barium Carbonate to enhance emission of the thermal electrons. The thermal electrons and a  $^3\text{He}$  gas introduced from a gas feeder ignite an arc-discharge between the cathode and an intermediate electrode and also between an anode and the intermediate electrode. These ionized gases are extracted by a second extraction electrode

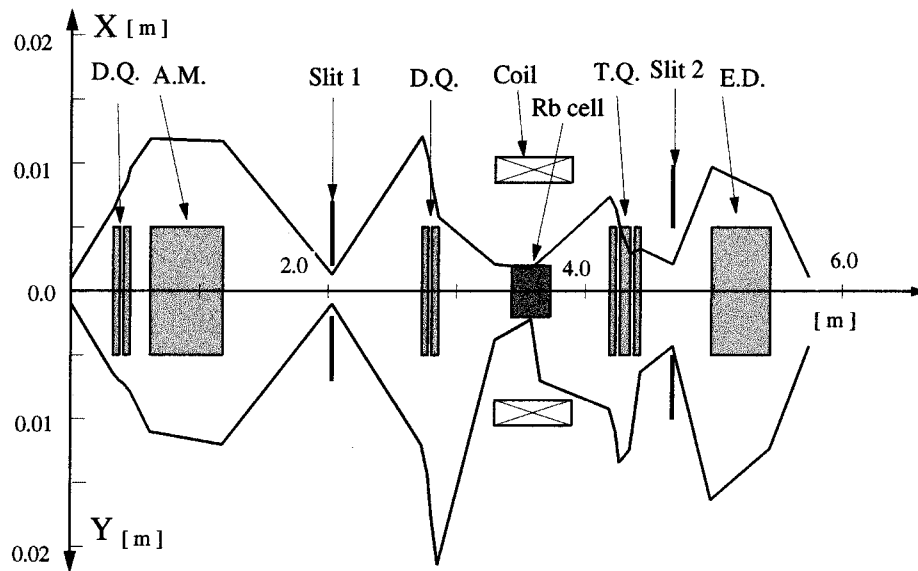


Figure 4.2: Calculated ion beam optics. D.Q. and T.Q. are an electrostatic doublet and triplet quadrupole lenses, respectively. A.M., E.D., and Coil are an analyzing magnet, an electrostatic deflector, and a superconducting solenoidal magnet, respectively.

applied a voltage of 19 kV. To focus the ion beam, 16.5 kV is applied at a first extraction electrode. The equivalent electric circuit is shown in Fig. 4.1.2. Typical operation parameters are tabulated in Table 4.1.

Extracted ions are momentum analyzed by a sector magnet, and a typical mass spectrum is shown in Fig. 4.1.2. It is noted that  $^3\text{He}^+$  ions have the highest peak among other ions. A typical  $^3\text{He}^+$  ion current is  $200 \mu\text{A}$ .

A photograph of this ion source is also shown in Fig. 4.1.2.

### 4.1.3 Optical pumping

A Rb vapor is polarized by the optical pumping method. Our system consists of a pumping laser, a Rb vapor cell and a Faraday rotation monitor system. A schematic view of the apparatus is shown in Fig. 4.7. The pumping laser is introduced to the Rb vapor cell located at the center of a superconducting magnet which can produce a magnetic field up to 6 T. The Rb polarization thus obtained is measured by the Faraday rotation method.

#### Pumping laser system

A 25 watt Ar ion laser ( Coherent : SBRC-DBW 25/7 Ar ion laser ) pumps a Ti:Sapphire ring laser ( Coherent : 899-01 Ti:Sapphire Ring laser ) in order to produce a 4-W pumping laser with a wavelength of 785 nm. The laser system is mounted on a vibration insulated table. With this

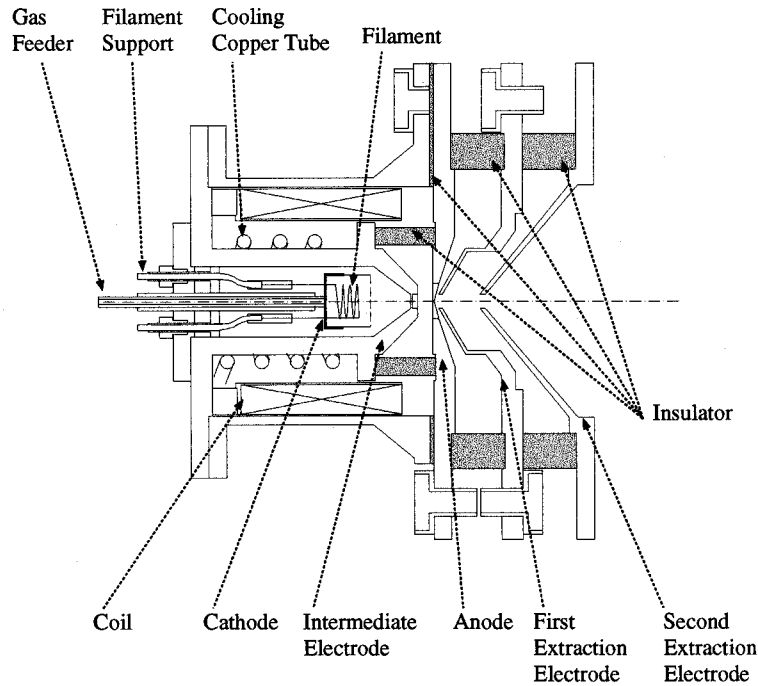


Figure 4.3: A cross section of the duoplasmatron ion source used in the present work.

pumping laser one can induce a transition between the  $5S_{1/2}$  and the  $5P_{1/2}$  states in a Rb atom. Tuning of the laser wavelength is accomplished by manually rotating a birefringent filter of the Ti:Sapphire laser cavity. The bandwidth of this light is 20 GHz by using an etalon. This is broad enough to fully cover the Doppler broadened bandwidth of the Rb atoms and the isotope shift between  $^{85}\text{Rb}$  and  $^{87}\text{Rb}$  atoms.

A beam transport system of the pumping laser is shown in Fig. 4.7. The laser beam out of a front output coupler of the Ti:Sapphire laser is introduced to a beam expander (BE) for enabling tuning the beam size at the Rb vapor cell position downstream. The beam is, then, lifted up to the height equal to the ion beam axis by a set of reflecting mirrors and is transported to a focusing lens (FL). This beam is converted to circularly polarized light from linearly polarized light by using a  $\lambda/4$  plate (QP). This circularly polarized light is injected into the Rb cell. The helicity of the light is reversed by rotating the  $\lambda/4$  plate. A focusing length of the pumping laser is adjusted by the beam expander so that the focusing point should be the center of the Rb vapor cell.

When we measure the Rb relaxation time by a time differential method, a switching system consisting of a Pockels cell (PC) and a polarizer (P) is inserted between the Ti:Sapphire laser and the beam expander, with which we could provide a pulsed pumping laser with a 10 ms duration.

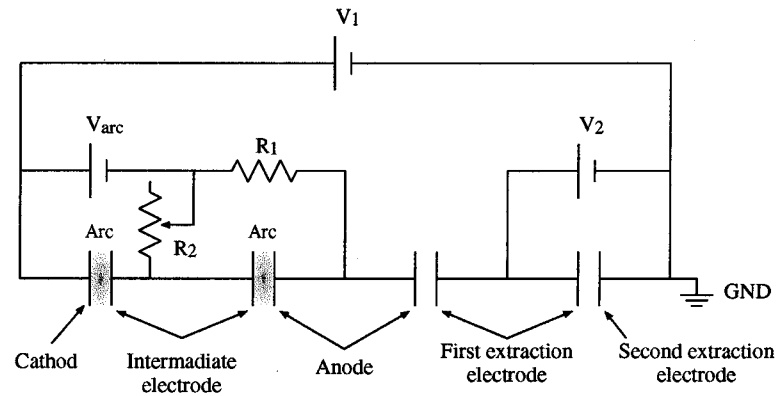


Figure 4.4: An equivalent electric circuit for producing the arc discharge and extraction system of the duoplasmatron.  $V_{\text{arc}}$ ,  $V_1$ , and  $V_2$  are an arc DC-power-supply and the first and second extraction DC-power-supply, respectively.

### Rb vapor cell

A cross section of the Rb vapor cell is shown in Fig. 4.8. A Rb cell is positioned in the center of a 5 T superconducting solenoidal coil. The cell consists of two 30-cm long coaxial copper tubes with a 1 cm and 3 cm diameters, respectively. A heater and water-cooling coils are wound around the outer tube to maintain a constant temperature of the inner tube (90 - 130 °C), whose values are monitored by a type-K thermocouple sensor. Liquid Rb is injected into the outer tube with the aid of a piston, from outside of the vacuum chamber. This arrangement facilitates in replacing a liquid Rb without breaking the vacuum, thus we can keep the vacuum at  $\sim 10^{-6}$  Torr. Due to the high temperature of the outer tube (90 - 130 °C), the Rb in the vapor cell diffuses into the pumping region through four straight slots in the inner tube, where the Rb vapor experiences the pumping laser exposures. The two layer structure of the Rb vapor cell provides a uniformly distributed Rb vapor throughout inside of the cell. The cell temperature is maintained constant with a fluctuation less than 0.5 °C, which enables us to keep the vapor thickness constant during the measurement. The vapor thickness is monitored during the measurement by the Faraday effect as discussed below.

At a distance of 35 mm from both edges of the Rb cell, a pair of water-cooled baffles are attached to confine the Rb vapor as much as possible.

### Faraday rotation measurement system

**(a) Principle of Faraday rotation** A Rb vapor thickness and Rb polarization are measured by the Faraday rotation method. The Faraday rotation is induced by difference between the reflective

Arc	voltage	50 V
	current	2 A
Filament	voltage	20 V
	current	20 A
Coil	voltage	60 V
	current	2 A
First extraction	voltage	19 kV
	current	1 mA
Second extraction	voltage	17 kV
Flow rate of $^3\text{He}$ gas		1 sccm
Degree of vacuum		$5 \times 10^{-6}$ Torr

Table 4.1: Typical operation parameter in the Duoplasmatron ion source

indices for left and right circular polarized lights as expressed by,

$$\theta = \frac{\pi l}{\lambda}(n_+ - n_-), \quad (4.1)$$

where  $n_+$  and  $n_-$  are the reflective indices for the left and right circular polarized light respectively,  $\lambda$  is a wavelength and  $l$  is a target length.  $n_+$ ,  $n_-$  depends on a Rb vapor density, an external magnetic field and a Rb polarization. When a Rb vapor density and a magnetic field are uniform, an amount of the Faraday rotation angle is given as,

$$\theta = \theta_0 + P\theta_p, \quad (4.2)$$

$$\theta = \theta_0 + \alpha P\theta_0, \quad (4.3)$$

$$\alpha = \frac{\theta_p}{\theta_0}, \quad (4.4)$$

$$\theta_0 = vN_0l \quad (4.5)$$

where  $P$  and  $v$  is the Rb polarization and the Verdet constant, respectively.  $v$  and  $\alpha$  is function of a magnetic field and a frequency of a probe laser. These values are computed by a program soft "Faraday" [55].

$$N_0l = \frac{\theta_0}{v} \quad (4.6)$$

and the Rb polarization is obtained by following equation

$$P = \frac{\theta - \theta_0}{\alpha\theta_0}. \quad (4.7)$$

Fig. 4.9 shows the Verdet constants in a magnetic field of 2 T as a function of a frequency of the probe laser computed by the "Faraday". As a result, Rb vapor thickness,  $N_0l$  is obtained by 4.6

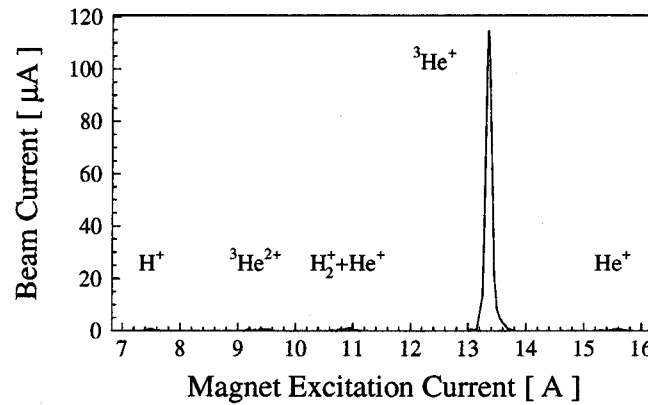


Figure 4.5: Mass spectrum for ions extracted from the Duoplasmatron ion source

**(b) Experimental set up** Our system developed for the measurement of the Faraday rotation angle is shown in Fig. 4.7. A monitor laser light from a diode laser penetrates the Rb vapor cell. The emerging laser light is, then, split into two components by a polarizing beam splitter, i.e., one is a perpendicularly polarized light with respect to the plane of incidence,  $I_{\perp}$  and the other one is a parallel polarized one,  $I_{\parallel}$ , after passing through a  $1/2 \lambda$  plate. Finally, each of these split lights is incident on two photo diodes (Hamamatsu : S2386-8K) by which each light intensities are measured. The electric currents from the photo diodes are converted into voltage with a current to voltage conversion circuit using a fast operational amplifier (TL081) as shown in Fig. 4.10. The converted voltage is measured by an ADC (Internix : PVME303). To reduce a fluctuation of the direction of a polarization plane of the monitor laser light, a Gran-Thomson prism (P) is inserted at the lower stream of a mirror (see Fig. 4.7). As a result, the fluctuation is reduced to less than  $0.008^{\circ}$ . The rotation angle of the polarization plane is analyzed by rotating the  $\lambda/2$  plate and measuring light intensities of these two components.

A tunable diode laser (Micro laser systems SRT7851 diode laser) of 50 mW power set at 789 nm wavelength is used for a probe laser to measure the Rb vapor thickness and Rb polarization by means of the Faraday effect. The choice of the wavelength (789 nm) is due to the fact that the Rb Verdet constant is rather insensitive to the variation of wavelength in the pumping region and it, thus, enables us a precise determination of the vapor thickness and polarization. The FWHM of the wavelength of this laser is 0.5 nm ( Fig. 4.11 ). The Faraday rotation angle depends on the wavelength of the light. The wavelength broadening of the probe laser, then, induces the broadening of the Faraday rotation angle. This is estimated to be only 1 % of the rotation angle at 2 T. In conclusion, this broadening has almost no influence on the present measurement of the Rb polarization and Rb vapor thickness which will be described below.

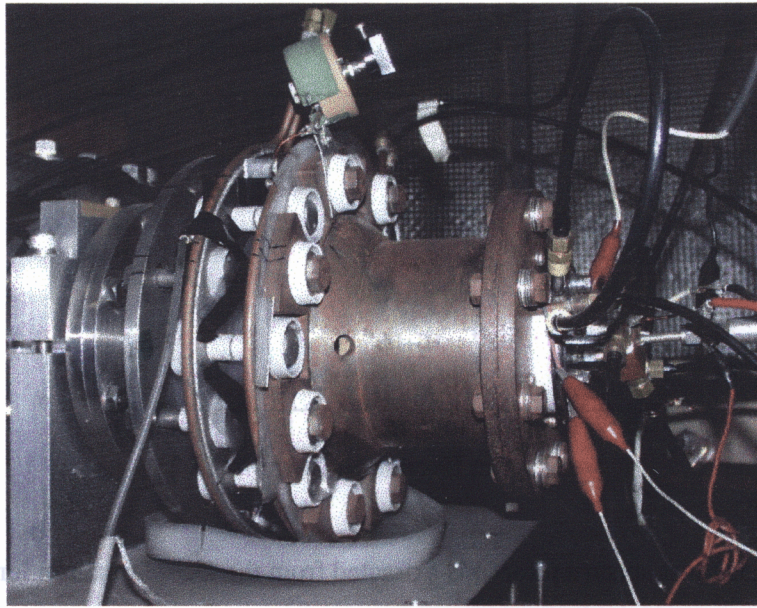


Figure 4.6: Photograph of the duoplasmatron ion source

**(c) Determination of the Rb vapor thickness and polarization** To determine the Faraday rotation angles, the intensity ratios,  $I_{\parallel}/I_{\perp}$  were measured by varying an axis of the  $\lambda/2$  plate (HP), i.e., by varying  $\theta_{\lambda/2}$ . Typical results are shown in Fig. 4.12, where the solid squares are the data for an empty cell at room temperature, the solid triangles are for the cell with Rb vapor at 130 °C without the pumping laser, and the circles represent the data for the polarized Rb vapor. It is worth noting that the shift in the intensity ratio is very sensitive to the Rb polarization, whereas it does not vary sensitively with the cell temperature. The data are well reproduced by fitting functions with a functional shape of  $f(\theta_{\lambda/2}) \propto \tan^2(\theta_{\lambda/2} + \theta_0 + \phi)$ , where  $\phi$  is the Faraday rotation angle. The Rb vapor thickness, thus determined is shown in Fig. 4.13 as a function of  $T_{\text{cell}}$ . The solid curve is the estimated density of the Rb vapor using the Killian's parameters [56]. It seems that the parameters of Ref. [56] reproduce the observed dependence of the Rb vapor thickness plotted as a function of the cell temperature. Thus, the Rb polarization was determined from the Faraday rotation angle measured with the pumping laser on. From the observed phase shifts in Fig. 4.12 we deduced the polarization of  $P = 0.25$ .

#### Insufficient optical pumping due to an inhomogeneity of the magnetic field

The magnetic field distribution over the Rb vapor cell is not uniform. In fact, as shown in Fig. 4.14-(a) which is obtained for 3 T at the center of the Rb vapor cell, a field distribution considerably varies over the cell region; the field at both edges drops to  $B \simeq 2.2$  T. Since the field gradient, in turn, induces a shift of the resonance frequency of the optical pumping, e.g., the frequency shift

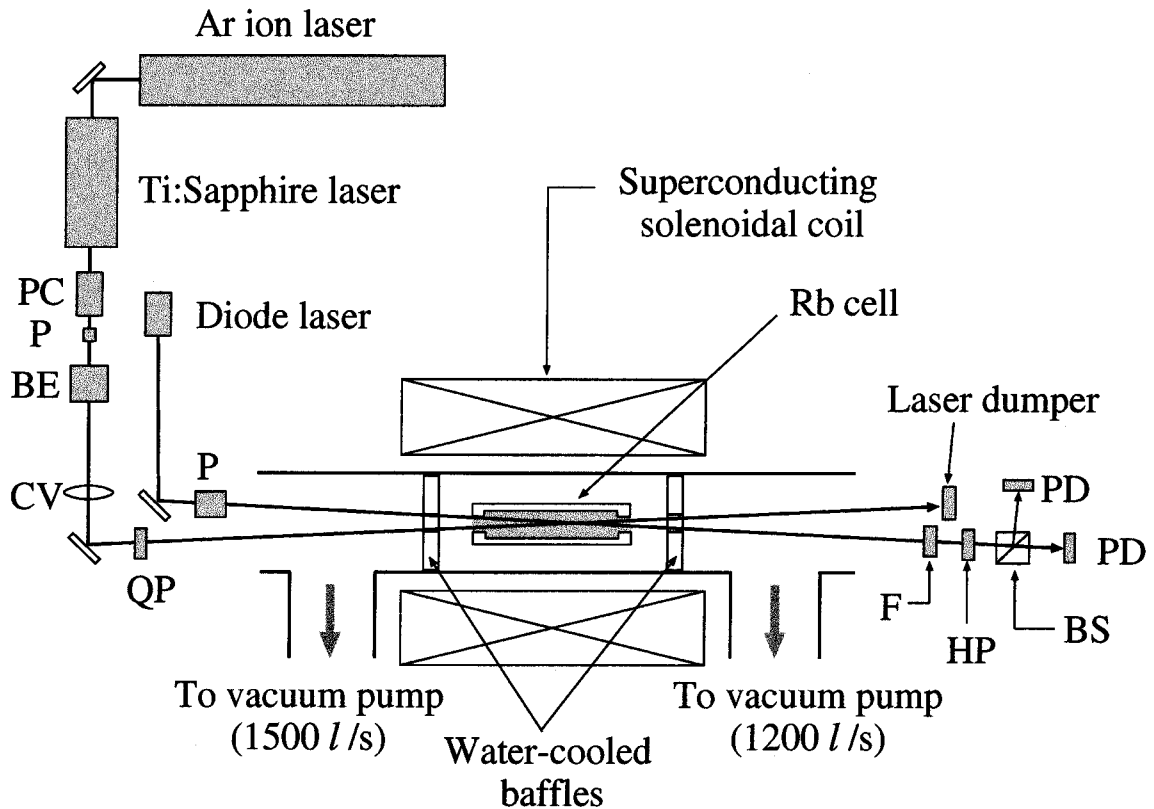


Figure 4.7: A schematic view of the experimental setup. PC, P, BE, QP, BS, F, PD, and HQ are, respectively, a Pockels cell, a polarizer, a beam expander, a  $\lambda/4$  plate, a polarizing beam splitter cube, a wavelength filter, a photo diode, and a  $\lambda/2$  plate.

between the cell center and cell edge is approximately  $\Delta\nu_p = 30$  GHz as shown in Fig. 4.14-(b). On the other hand, the width of the pumping laser frequency extracted from the Ti:Sapphire laser is 20 GHz. This indicates that the pumping laser cannot cover the whole resonance frequency for the Rb atoms with a magnetic field of 3 T at the cell center. This means that if one wants to cover the whole range of the cell, the magnetic field should be reduced to 2 T. Otherwise, one may induce a formation of the polarized Rb vapor partially localized in the cell. However, as later discussed extensively, this is not a demerit. We succeeded in investigating the relaxation mechanism of the Rb vapor optically pumped by forming a polarized Rb vapor localized in the cell. This will be described in the later section. A similar technique was used for the measurement at a low magnetic field [57].

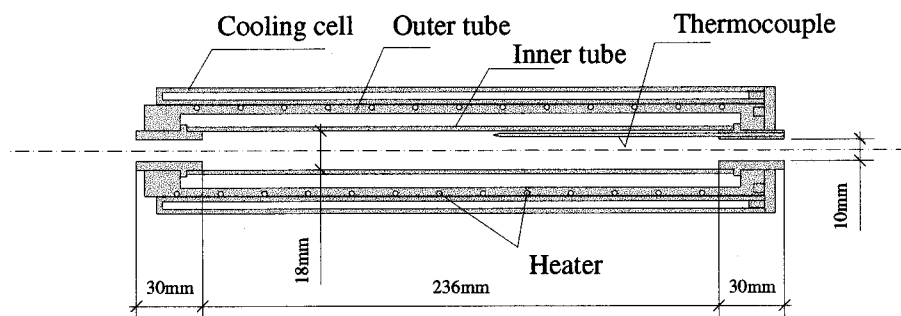


Figure 4.8: A cross section of the Rb vapor cell.

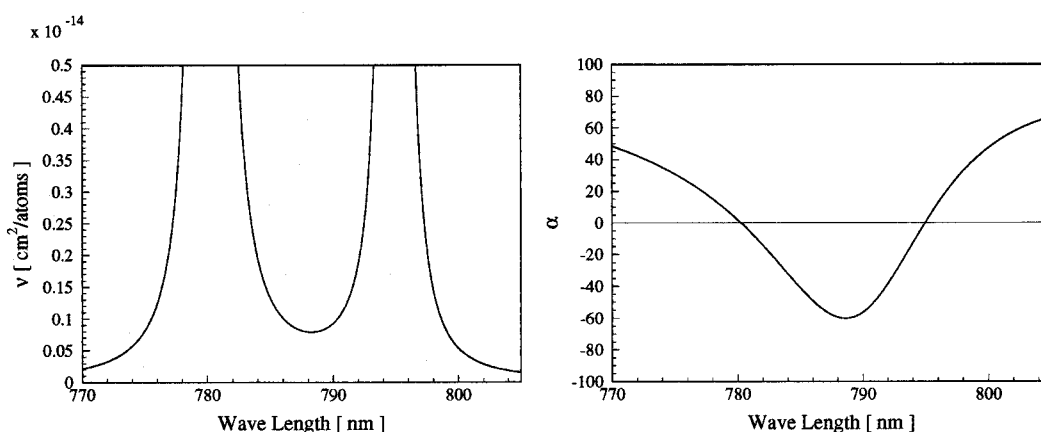


Figure 4.9: The Verdet constant,  $v$  associated with the vapor thickness (left) and the  $\alpha$  associated with the Rb polarization (right) plotted as a function of the probe laser frequency in a magnetic field of 2 T.

#### 4.1.4 Superconducting solenoidal magnet

A superconducting solenoidal magnet (Mitsubishi Electric Corporation : MD-190-60) was introduced to produce the LS decoupling field for  $^3\text{He}$  atom. The magnet consists of a conduction cooled NbTi solenoid, a high  $T_c$  superconductor current leads, and Gifford-McMahon (GM) refrigerator [58]. The GM refrigerator can cool down the solenoid from the room temperature to below 4 K in a few days. Then, the GM refrigerator [59] allows us to operate the system without supplying any cryogen such as liquid helium or nitrogen. The geometry of this magnet is described as follows; the inner diameter is 160 mm, the outer diameter is 600, and overall axial size is 560. The magnet produces a maximum central field of about 6 T at the operation current of 38 A. The measured and calculated values of the magnetic flux density is plotted as a function of the  $z$  axis in Fig. 4.15. The measured value was provided from the Mitsubishi Electric corporation. The

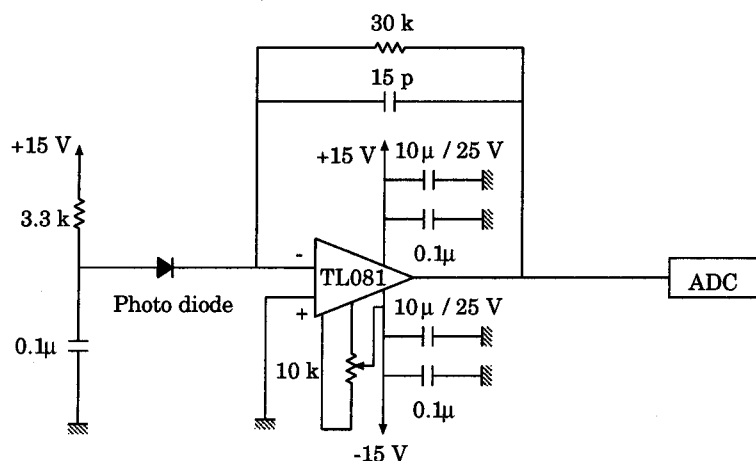


Figure 4.10: A photo diode, amplifier, and ADC for the measurement of the Faraday rotation angle.

calculation of the field strength was done by using the program, “POISSON” in order to examine the performance of the magnet. A reasonable agreement between the calculation and observation is found, which suggests the magnet works reasonably. It is also noted that magnetic field decreases to 70% at the position,  $z = 15$  cm corresponding to the Rb cell edge. The magnet is usually operated at 2 T, since this value is enough strong to decouple the LS coupling (see section 3.1.4). In addition, the pumping laser system sufficiently covers the line broadening of the Rb resonance due to inhomogeneity of the magnetic field.

### Helmholtz coil

To avoid depolarization due to the perturbing fields from the terrestrial magnetism, the stray field of the cyclotron, etc., a uniform magnetic field with 10 G was applied to a region where the nuclear polarized  $^3\text{He}^+$  ion was formed, i.e., a region downstream of the superconducting magnet.

For this purpose, a Helmholtz coil was designed and installed. A basic design was carried out with the program “POISSON”. We determined the dimension of the Helmholtz coil so that the direction of the produced magnetic field might be less than  $\sim 10^\circ$  with respect to the  $z$ -axis over the covered range. The parameters thus obtained are tabulated in Table 4.1.4. Each coil has a diameter of 136cm and a distance between two coil was 32 cm. Each coil was composed of a copper wire with 200 turns. The field strength at the center of the Helmholtz coil was about 10 G with a driving current of 3.6 A.

The magnetic flux densities as a function of  $z$  and  $r$  are shown in Fig. 4.1.4. A solid line is a calculated result with the “POISSON” and open circles are measured data with a hole probe at the coil-current of 3.5 A.

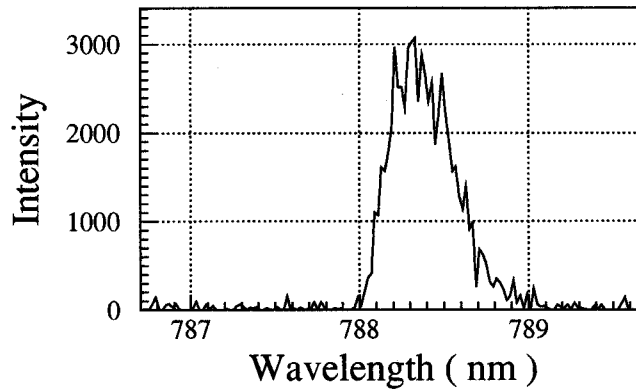


Figure 4.11: A line shape of the diode laser used for the measurement of the Faraday rotation angle.

Magnetic flux density at coil center	10 G
Distance between two coils	64 cm
Coil diameter	136 cm
Electric current of coil	3.7 A
Voltage for two coils	43 Volt
Wire material	Enameled copper
Diameter of wire	2 mm
Turn numbers of wire/coil	200 turn

Table 4.2: Designed parameters for Helmholtz coil.

The Helmholtz coil covers a region downstream of the superconducting magnet. The direction of the symmetry axis of this magnetic field is the same as that of the superconducting solenoidal magnet.

#### 4.1.5 Beam-foil polarimeter

##### Principle

A principle of the polarimeter is based on the the beam-foil spectroscopy firstly succeeded by Andrä [60]. A nuclear polarized  ${}^3\text{He}^+$  ion penetrating a thin carbon foil multiply captures and strips electrons of the carbon atoms in the foil and finally a charge state of the incident  ${}^3\text{He}^+$  ion is equilibrated, i.e., the incident  ${}^3\text{He}^+$  ions becomes almost a  ${}^3\text{He}$  atom for an incident energy of a

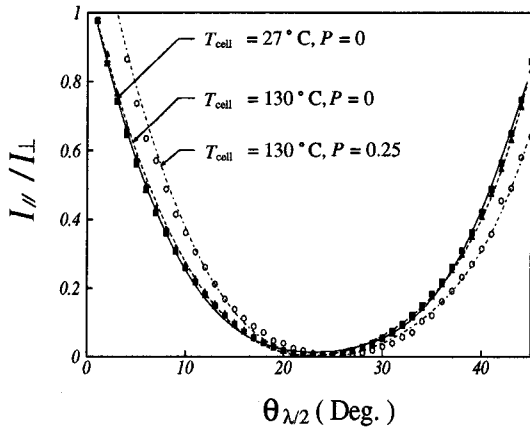


Figure 4.12: Intensity ratios observed by rotating the axis of a  $\lambda/2$  plate at various cell temperatures under the magnetic field strength of 2 T.

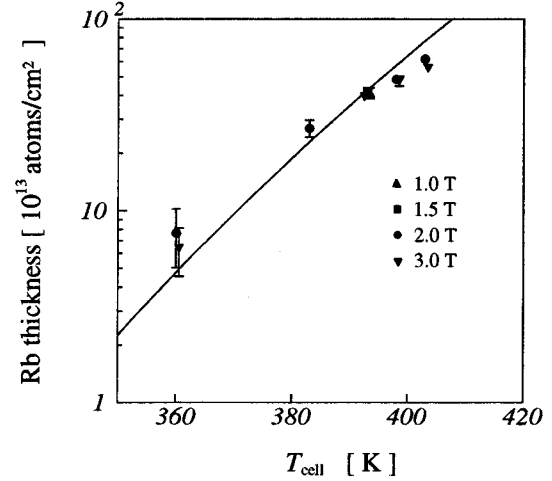


Figure 4.13: The observed Rb vapor thickness determined by the measurement of the Faraday rotation angle. The solid curve is the calculated result using a formula expressing a saturation vapor pressure in Ref. [56].

few keV/amu. Since the hyperfine periods for the  $^3\text{He}$  atoms are much longer than the penetrating time through the foil, the nuclear polarization is hold during collision process.

Most of the  $^3\text{He}$  atoms in the equilibrated charge state emerging out of the foil are in the excited state. They deexcite to the ground or metastable state by emitting photons in flight. During these photon emission process, a certain amount of the nuclear polarization is periodically transferred to the atomic electron by the hyperfine interactions. This eventually generates a circular polarization for the emitted photons. If one, in turn, observes the degree of the circular polarization, one can determined the degree of the nuclear polarization. This is an intuitive explanation of the beam foil spectroscopy.

Photons with a wavelength of 388.9 nm corresponding to the transition between the  $3^3\text{P}_J$  ( $J = 0, 1$  or  $2$ ) and  $2^3\text{S}_1$  states were used in the present measurement of the  $^3\text{He}$  nuclear polarization. They were analyzed with an optics device consisting of a  $\lambda/4$  plate, an interference filter, a linear polarizer, and finally a photomultiplier [61]. As a result, the polarization of the  $^3\text{He}^+$  ion was obtained from the measured  $^3\text{He}$  nuclear polarization.

The circular polarization is defined in terms of the Stokes parameter as,

$$\frac{S}{I} = \frac{N(\sigma^+) - N(\sigma^-)}{N(\sigma^+) + N(\sigma^-)}, \quad (4.8)$$

$$N(\sigma^\pm) = C(\sigma^\pm)/B(\sigma^\pm), \quad (4.9)$$

where  $C(\sigma^\pm)$  and  $B(\sigma^\pm)$  are, respectively, counts of the analyzer and the beam monitor detector

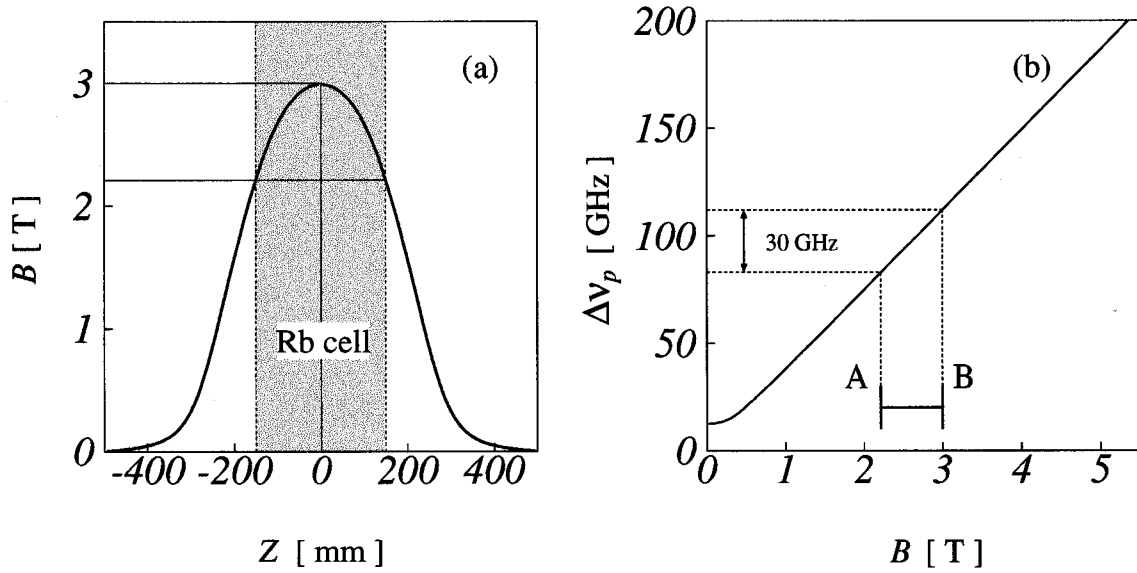


Figure 4.14: (a) Magnetic field distribution of the solenoidal coil plotted as a function of the position along the  $z$  axis in case of  $B = 3$  T at the cell center. (b) A resonance shift of  $D_1$  line due to inhomogeneity of the magnetic field strength (solid curve). The resonance shapes “A” and “B” show localized resonances at both ends and the center of the cell, respectively.

for  $\sigma^\pm$  photons. Then, nuclear polarization of  $^3\text{He}$ ,  $P$ , is given by

$$P = \frac{S}{I} A^{-1}, \quad (4.10)$$

$$A = 0.207, \quad (4.11)$$

where  $A$  is an analyzing power.

### Apparatus of the beam foil spectroscopy

A whole assembly of the polarimeter is located in a uniform magnetic field ( 10 Gauss ) produced by the Helmholtz coil which was described in the preceding subsection. A chamber of the polarimeter is evacuated by a 500  $\ell/s$  turbo molecular pump. A liquid  $\text{N}_2$  trap is attached to the vacuum chamber to improve the vacuum condition enabling to reduce collisions of a polarized  $^3\text{He}$  with the residual gas in the chamber. A typical value of the vacuum degree was about  $1 \sim 3 \times 10^{-7}$  Torr. The photograph of the polarimeter is shown in Fig. 4.17. The experiments were carried out, at first, with a polarimeter 1 which allowed a detection of the circular polarization for the photons emitted only to one direction as shown in Fig. 4.18. We, then, improved the polarimeter 1 so that the detection for both directions might be possible (a polarimeter 2) as shown in Fig. 4.19. In addition, we installed a beam monitor in this polarimeter so that we could accumulate more stable data. A detailed description on the optical device of the polarimeter is as follows: The

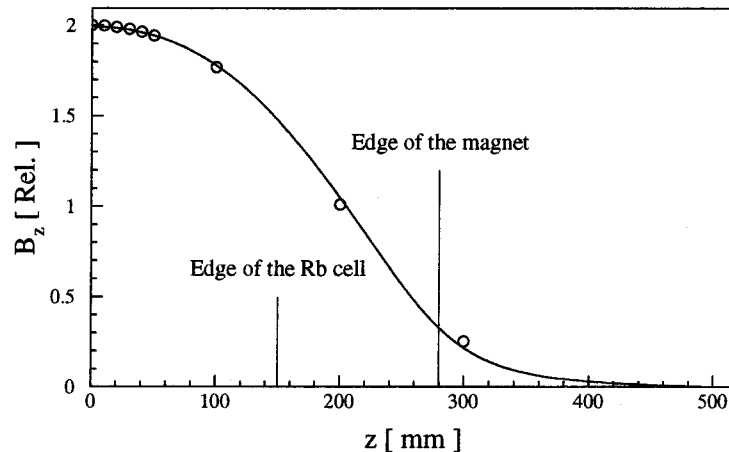


Figure 4.15: The magnetic flux density of the superconducting solenoidal magnet as a function of a  $z$  axis. The solid curve is a calculation result by using “POISSON”. The open circles are measurement results (by Mitsubishi Electric Corporation).

deexcited photons from He I atoms formed after penetration of  $^3\text{He}^+$  ions through the carbon foil were focused by a couple of convex lenses. The circular polarization of the deexcited photons is converted to the linear polarization by a  $\lambda/4$  plate, and the linear polarization is measured by a polarizer (Polaroid). The analyzed photons are detected by a photo multiplier (Hamamatsu R329P). The lens system was designed so that  $\Omega/M$  might have a maximum value, where  $\Omega$  is a solid angle of the detector and  $M$  is a lateral magnification. The calculation shows that the  $\Omega$  and  $M$  are, respectively, determined to be  $0.0388 \times 4\pi$  and 2.22. The length of the observation region along the beam axis is  $\sim 7$  mm. This is experimentally confirmed by using an LED (Fig. 4.20). The analyzing power for the deexcited light is known to oscillate along the beam direction, which is called a quantum beat [33]. However, since the observation length is much longer than a quantum beat period, the oscillating pattern is averaged (Fig. 4.20). The specification of each component composing the photon detection system is tabulated in Table 4.1.5.

### He I spectra

The photons corresponding to the transitions between the  $3^3P_J$  and  $2^3S_1$  states in He I, where with  $J=0,1$ , and 2 (though each of them was not experimentally separated), are selected by a wave length coherent-filter located in front of the photo multiplier.

These transitions have higher intensities and a longer life time ( $\sim 100$  nsec) than others. Fig. 4.21 shows observed spectra, where an upper spectrum is taken without a filter and lower one is taken with it.

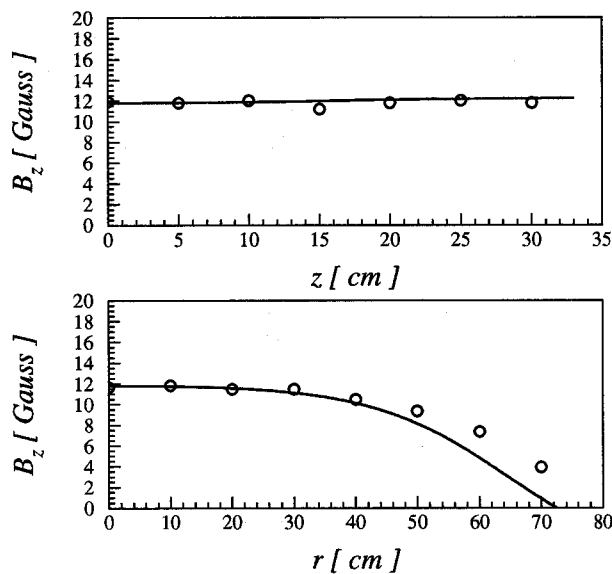


Figure 4.16: Plots of magnetic field strength,  $B_z$  as a function of  $z$  and  $r$  with a coil current of 3.5 A. Open circles are measured values and solid curves are the results of the calculation by using a computer code, POISSON

#### System check by the tilted foil method

As mentioned by Fano and Macek [62], excitation of ion/atom by collision through a foil leaves it generally in anisotropic state. Light emitted in the subsequent decay manifests this anisotropy through its angular distribution and polarization. In general, if a beam passes in the normal direction through a foil, only alignment of the excited atoms of the beam is possible, but by tilting the foil, the broken axial symmetry results in strong angular momentum orientation, i.e. polarization. In this remarkable process, despite the rough final surface of the carbon foil, the atom senses an average tilt, and the electrons receive an asymmetric net impulse.

The performance of our polarimeters is tested by using  $^3\text{He}$  polarized by tilting the foil. The results are shown in figure 4.22. When the tilting angle of the foil is reversed, it is observed that the circular polarization of the deexcited photons consistently changed its sign. This result confirms validity of this polarimeter.

In the course of the present measurement, a typical photon counting rate is  $\sim 10$  kcps with a beam current of 100 nA. The S/N ratio for the photon detection is 50 with this beam current. Under this condition, the nuclear polarization is determined with a precision better than 0.005 in

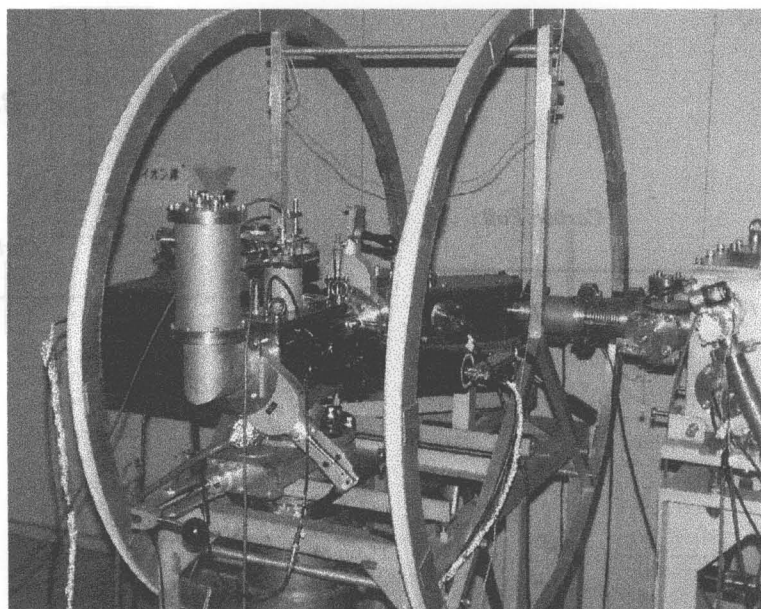


Figure 4.17: Photograph showing the beam-foil polarimeter and the Helmholtz coil

6 minutes measurement. The measurement of the electron pumping was also done with the above counting rates.

## 4.2 Computer control data acquisition systems

The computer control of the device and data acquisition was done by using the NIM modules, the Versa Module Europe (VME) modules and a workstation (SUN : Spark20).

A VME address is virtually mapped on a memory space of the workstation via the VME-S bus interface module (Nissho electronics : Solflower 110). The system, thus, allows us to directly access to the VME address through the workstation. As a result, the VME can be controlled by a UNIX OS (Solaris 2.4) on which the workstation operates. All programs for this data acquisition system are written in the C program language.

The detected photon intensities by a couple of photo diodes for the Faraday rotation measurement are converted from a current to a voltage by a conversion circuit as described previous section and the signals are fed into an 12 bit ADC (Internix : PVME303P). These data are registered on a memory of ADC sequentially. The registered data are read by the workstation and saved on a hard disk.

Photons detected by a photo multipliers of the beam-foil polarimeter are counted by a 24 bit scaler for the VME (Hitachi Zosen : H606B).

Stepping motors attached on the beam-foil polarimeter and the Faraday rotation system are controlled via the GPIB. The GPIB commands are sent via a GPIB-VME bus interface board

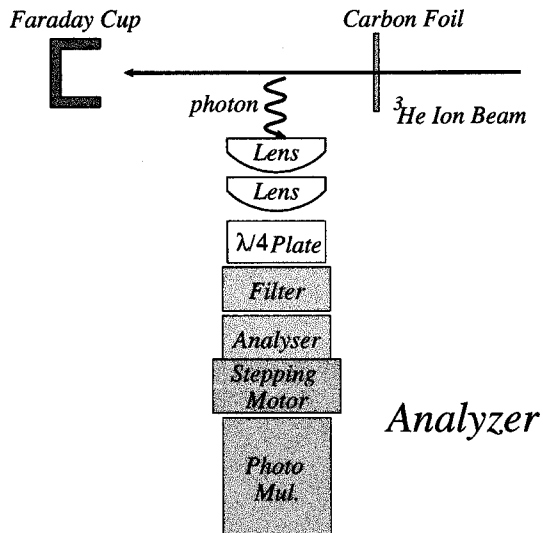


Figure 4.18: Schematic view of the beam-foil polarimeter 1

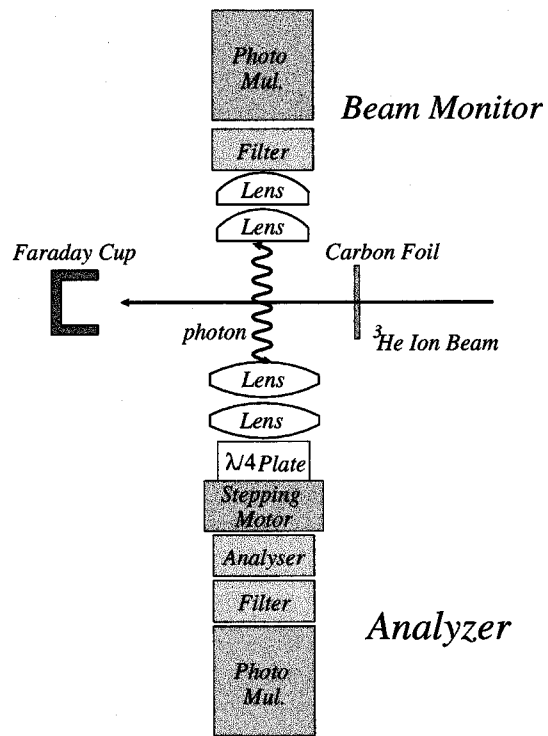


Figure 4.19: Schematic view of the beam-foil polarimeter 2

(Nisshin Electric Corporation : EVME-GPIB21) to a stepping motor driver (Suruga Seiki : D80).

In the NIM system, the analogue signals from the photo multipliers are converted to the logic signals and they are sent to a scaler. A gate signal to the scaler and a trigger signal to the ADC was generated by a Gate & Clock generator. Wave form shaping circuits are required to generate signals acceptable by the scaler and the ADC trigger.

Data and command handling between the VME boards and the workstation are carried out with a polling mode because this mode is much simpler than an interrupting mode. A characteristics of the polling mode controls the modules with reading a content of a status register.

Finally, the read-out data from the data files are graphically displayed with PAW which was developed at CERN as an interactive utility to visualize experimental data on a computer graphics display.

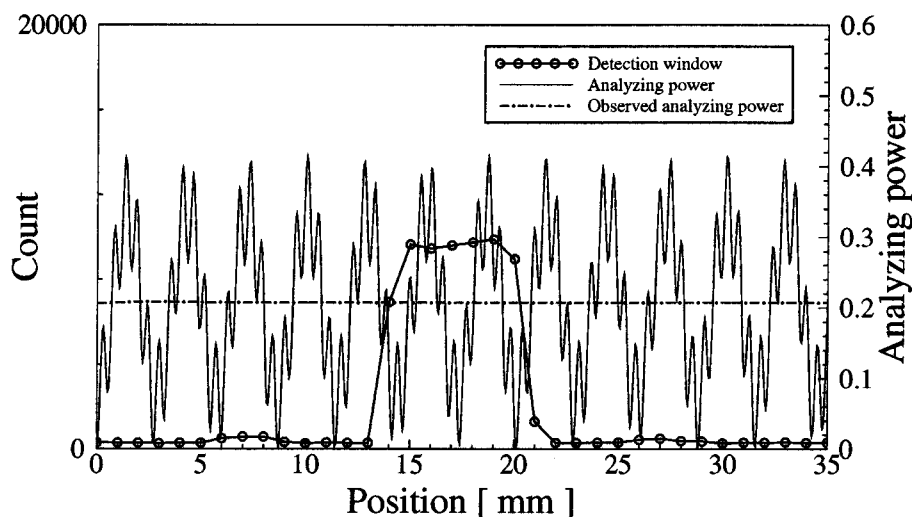


Figure 4.20: A detection efficiency of photons vs position from carbon target (open circles). The solid curve is the calculated analyzing power for the 388.9 nm line. The dot-dashed line is an average value of the analyzing power.

		Polarimeter 1	Polarimeter 2	
		Analyzer	Analyzer	Monitor
Lens (Sigma Koki)	Focal length	70 mm	70 mm	70 mm
	Diameter	50 mm	60 mm	50 mm
	Material	BK7	BK7	BK7
	Transmission (389 nm)	91.8 %	91.8 %	91.8 %
$\lambda/4$ plate (Sigma Koki)	Aimed wavelength	389 nm	389 nm	-
	Transmission	99 %	99 %	-
Polarizer (Polaroid : HNP'B)	Extinction ratio	0.004	0.004	-
	Transmission	51.5 %	51.5 %	-
Wavelength filter (Optical Coatings Japan : MIF-W, * DIF-BP-UV)	Central wavelength	389 nm	389 nm	389 nm*
	FWHM	20 nm	20 nm	9.5 nm*
	Transmission	41.5 %	41.5 %	46.5 %*
Photomultiplier (Hamamatsu : R329P)	Quantum efficiency	23 %	23 %	23 %
	Effective diameter	2 inch	2 inch	2 inch
	Typical bias voltage	-1.8 kV	-1.8 kV	-1.8 kV

Table 4.3: Specification of the optical elements used for the beam-foil polarimeter 1 (Pol. 1) and 2 (Pol. 2).

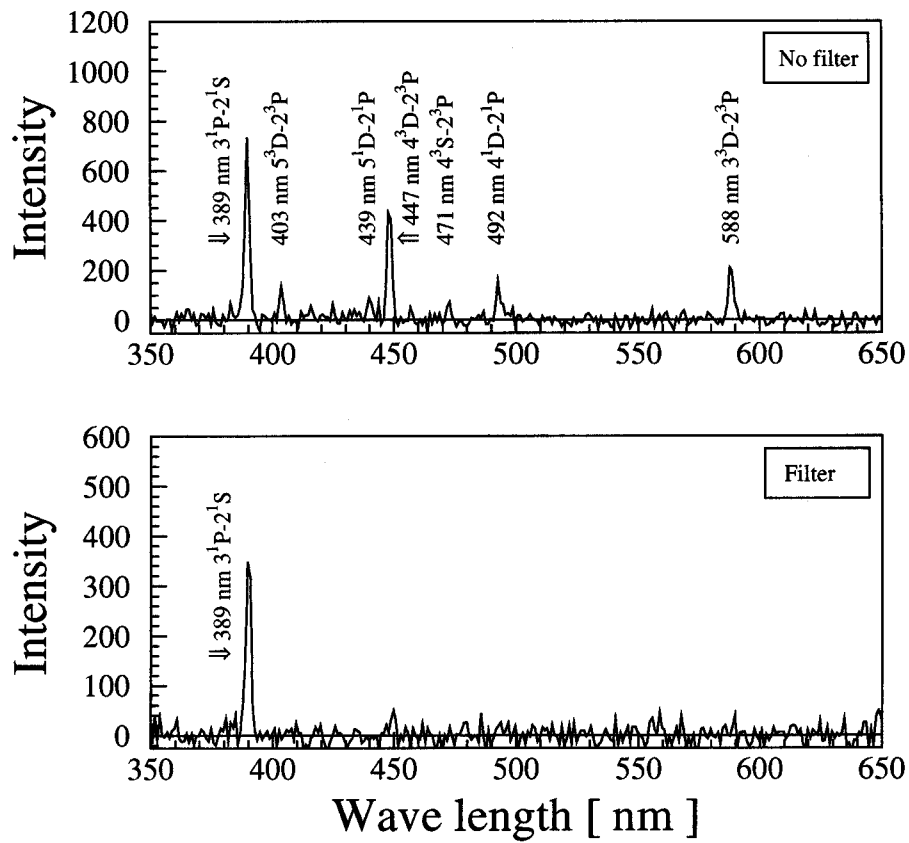


Figure 4.21: Photon spectra from He I atoms formed after  $^3\text{He}^+$  ions penetrate a  $5 \mu\text{g}/\text{cm}^2$  carbon foil. The upper figure is taken without filter and the lower one is taken with a filter.

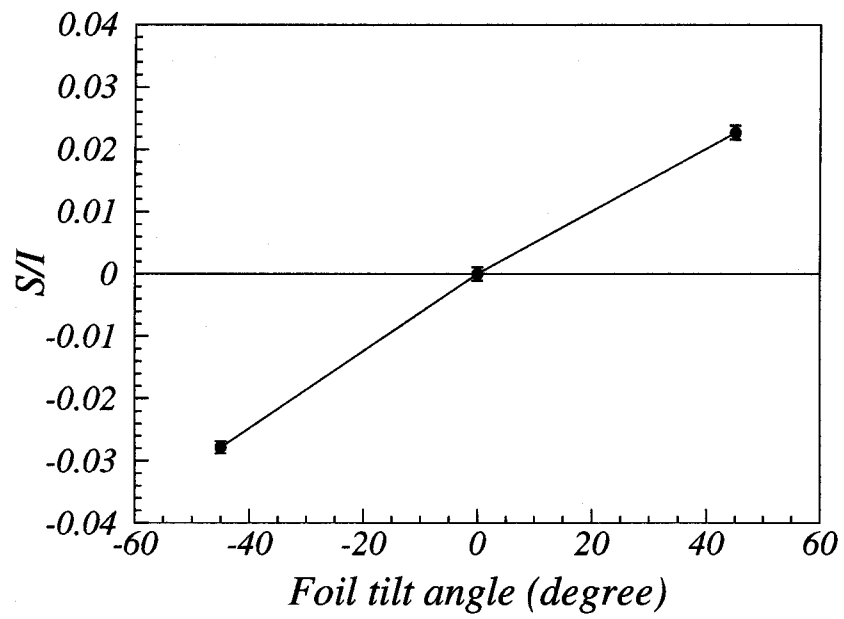
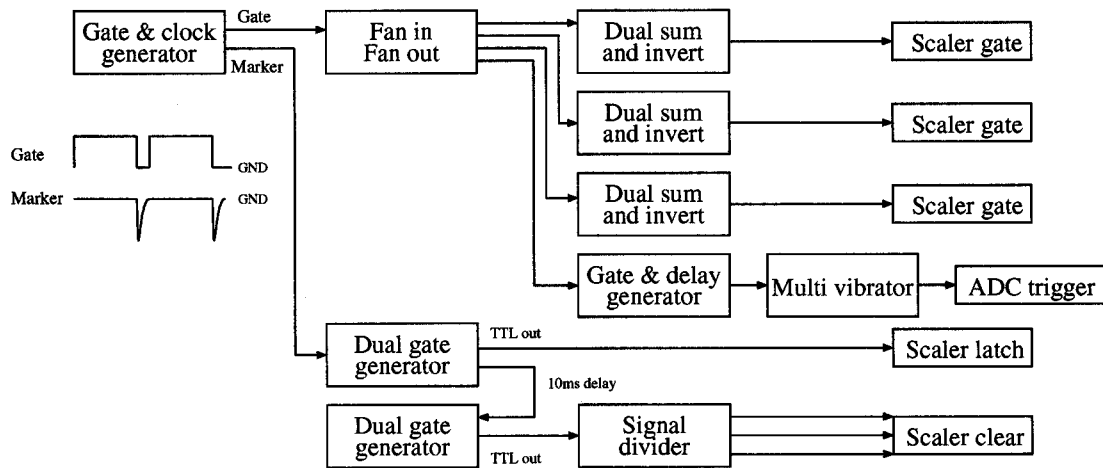


Figure 4.22: The observed polarization of  $^3\text{He}$  generated by the tilting foil method.

## (a) Trigger system



## (b) Beam-foil polarimeter system

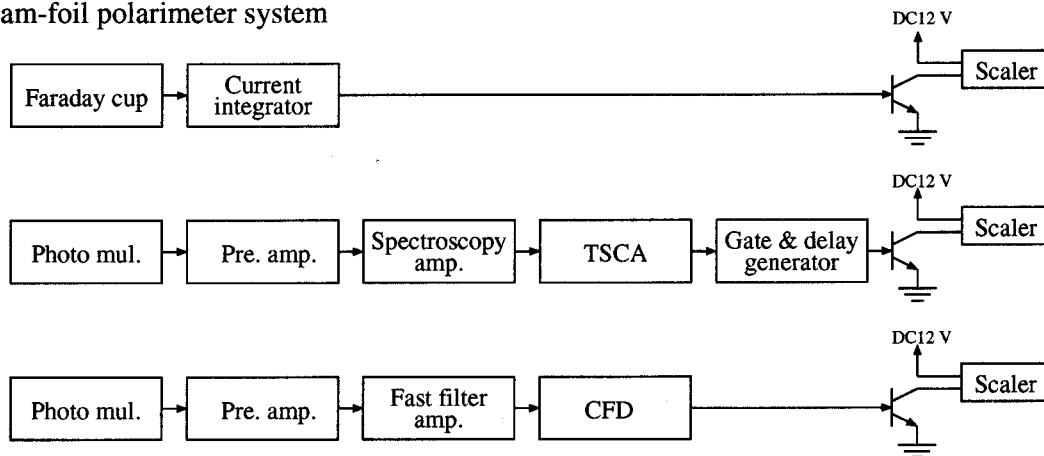


Figure 4.23: Block diagram for circuit system; (a) trigger circuit system for ADC and gate circuit system for scaler, (b) circuit system for the beam-foil polarimeter.

## Chapter 5

# Experimental results and discussion

In this chapter, we will present the experimental results for each subject and subsequent discussion. We will, in the first section, mention the results and discussion on verification of the electron pumping by observing the Rb vapor thickness dependence of the  $^3\text{He}$  polarization, which is a primary aim of our work. In the same section, we will also discuss the spin-exchange cross sections between a  $^3\text{He}^+$  ion and a Rb atom deduced from the Rb vapor thickness dependence of the  $^3\text{He}$  polarization in terms of the theoretical calculations based on a semiclassical impact parameter method, in which formation of a quasimolecule by a Rb atom and a  $^3\text{He}^+$  ion. Finally, we will mention the direct observation of the Rb relaxation times and their understanding in terms of the wall relaxation and the relaxation due to the effusion.

### 5.1 Verification of the electron pumping

As discussed in section 3.1, the electron pumping has a characteristic feature that the  $^3\text{He}$  nuclear polarization increases with an increase of a Rb vapor thickness. On this basis, we have examined the  $^3\text{He}^+$  nuclear polarization by changing the Rb vapor thickness verify the electron pumping principle.

Before going into the detailed description on the above subject, we will briefly touch, at first, the experimental results on variation of the Rb polarization with the Rb vapor thickness, which is subsidiary important in proving the principle of the electron pumping.

#### 5.1.1 Rb polarization vs Rb vapor thickness

In general, the Rb polarization would be decreased according to an increase of the Rb vapor thickness by the following mechanisms; the depolarization due to the radiation trapping effect, and atomic collisions between Rb atoms, and an absorption of the pumping laser light. Among the depolarization mechanisms proposed above, the depolarization due to the Rb-Rb collision is less pronounced at the Rb thickness of present interest, i.e.,  $\leq 10^{15}$  atoms/cm<sup>2</sup>.

To see the above aspect, the Rb polarizations was measured by changing the Rb vapor thickness, where the Rb thickness and Rb polarization were measured by observing the Faraday rotation angles as described in the preceding chapter. A typical laser power used in this measurement was 4 watts.

The measured Rb polarizations are shown in Fig. 5.1 as a function of the Rb thickness. It is found that the Rb polarization decreases from 60% to 20% with an increase of the vapor thickness from  $2 \times 10^{14}$  to  $10 \times 10^{14}$  atoms/cm<sup>2</sup>. This behavior is understood in terms of the radiation trapping effect and the absorption of the pumping laser [63].

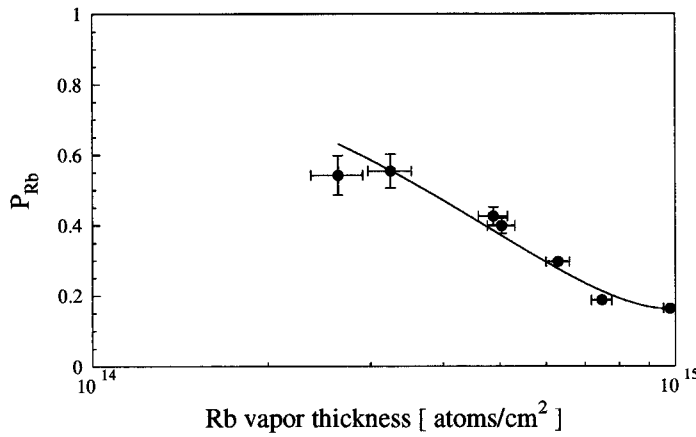


Figure 5.1: Rb polarization optically pumped by a 4-W pumping laser plotted as a function of the Rb vapor thickness.

The experiment of the electron pumping, was in fact, carried out in the range of the Rb thickness same as the above measurement.

### 5.1.2 <sup>3</sup>He nuclear polarization vs Rb vapor thickness

We observed a <sup>3</sup>He<sup>+</sup> nuclear polarization by varying the Rb vapor thickness. For allowing a reliable data accumulation, a helicity of the pumping laser was changed by rotating a  $\lambda/4$  plate. Fig. 5.2 shows the result at the Rb vapor thickness of  $5.5 \times 10^{14}$  atoms/cm<sup>2</sup>. The left and the right symbol in this figure are the observed Stokes parameter when the pumping laser is ignited with an opposite helicity each other. To correct the systematic error due to the tilted foil effect, the observed Stokes parameters are corrected by subtracting the background caused when the pumping laser was off. It is found that the left one is maximum nuclear polarization achieved in our experiments and this value is 5.5 % at the Rb vapor polarization of 16 %.

However, as mentioned in the above subsection, the Rb polarization changes with the Rb vapor

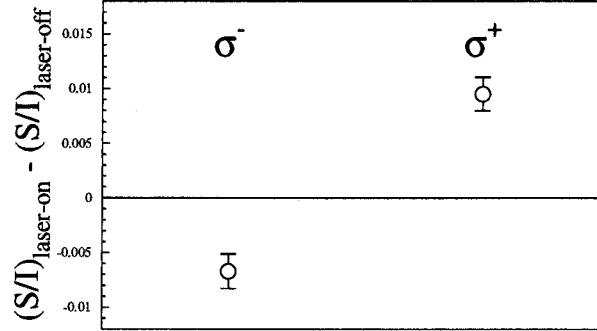


Figure 5.2: Observed Stokes parameters corrected for the baseline shift due to the system asymmetry.  $\sigma^+$  ( $\sigma^-$ ) indicates the right (left) circular polarization for the pumping laser at Rb polarization of 0.16 (-0.10), respectively.

thickness. Therefore, instead of using the  $^3\text{He}^+$  nuclear polarization itself, we must normalize it by the Rb polarization. This quantity is called a polarization transfer coefficient defined by

$$P_T = \frac{2P_{\text{He}}}{P_{\text{Rb}}}, \quad (5.1)$$

where  $P_{\text{He}}$  and  $P_{\text{Rb}}$  are a  $^3\text{He}$  nuclear polarization and a Rb polarization, respectively. Here, it should be noticed that a fraction of polarization transferred from an electron of  $^3\text{He}^+$  ion to a  $^3\text{He}$  nucleus is 1/2 with the present arrangement, a factor '2' appears in this formula.

The deduced  $P_T$ 's are plotted as a function of the Rb vapor thickness as shown in Fig. 5.3. It is clearly seen that  $P_T$  increases according to an increase of the Rb vapor thickness. The behavior is qualitatively understood as follows: When the Rb vapor thickness is increased, the number of collision cycles between the  $^3\text{He}$  ion/atom and Rb atoms is increased. The polarization of the  $^3\text{He}^+$  ion increases cumulatively as the results of multiple electron capture and stripping processes and the spin-exchange processes.

The experimental results are compared with the theoretical calculations for the electron pumping. The rate equations prescribed in the Chap. 3 were solved with a few sets of the reasonable collision cross sections. The capture cross section was taken from the experimental results of Girnius et. al. [64]. Since adequate data for the stripping cross section are not available for the He-Rb system, we use data deduced from the charge exchange collisions between Cs vapor and  $^4\text{He}$  ions at  $E(^4\text{He}) = 25$  keV [65] expecting that the cross sections for the  $^3\text{He}^+$ -Rb system are similar to the above ones [64] (Fig. 5.4). Since the presence of the spin-exchange interactions between a Rb atom and a  $^3\text{He}$  atom or a  $^3\text{He}^+$  ion is expected to enhance the electron pumping,

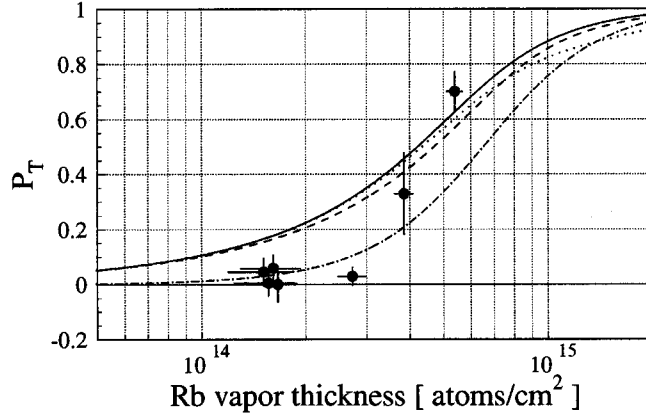


Figure 5.3: Experimental and theoretical values of the polarization transfer coefficient,  $P_T$  plotted as a function of the Rb vapor thickness.  $P_T$  is defined as a  $P_{He}/P_{Rb}$ , where  $P_{He}$  is an electron polarization of the  $^3\text{He}^+$  ion after emerging from the polarized Rb vapor.

we employed the spin-exchange cross sections theoretically predicted for fast hydrogen impact on rubidium atom [66].

Curve	$\sigma_{10}$	$\sigma_{t+}$	$\sigma_{s+}$	$\sigma_{se}$	$\sigma_{sea}$
solid	4.18	1.08	0.012	1.0	1.0
dashed	4.18	0.59	0.012	1.0	1.0
dot-dashed	4.18	1.08	0.012	0.0	1.0
dotted	4.18	1.08	0.012	1.0	0.0

Table 5.1: Cross sections for capture, stripping, and spin-exchange used for the calculations of  $P_T$  as a function of the Rb thickness. The cross-sections are in unit of  $10^{-15} \text{ cm}^2$ .

The solid curve is the result of the full calculation and the dashed curves is the calculated result with the stripping cross section,  $\sigma_{t+}$  reduced to a half of the first case, and the dot-dashed and dotted curves are, respectively, the calculated result with the spin-exchange cross section for atomic  $^3\text{He}$ ,  $\sigma_{sea}$ , set equal to zero and with the one for ionic  $^3\text{He}$ ,  $\sigma_{se}$ , set equal to zero. The need for the second calculations (dashed curve) is due to the fact that the measurement of the stripping cross section of a  $^4\text{He}$  atom in either triplet or singlet state has uncertainty larger than that of the capture cross section because of the indirect measurement [65]. The numerical values of the cross sections for the above four cases are shown in Table 5.1. The notations in this table are referred to the subsection 3.1.3. The calculated results in Fig. 5.3 demonstrate that the increase of  $P_T$ , as

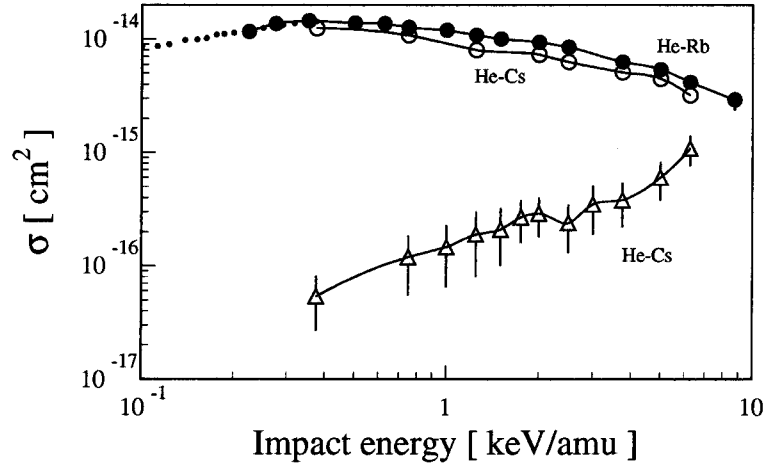


Figure 5.4: Capture and stripping cross sections plotted as a function of  ${}^3\text{He}^+$  impact energy. The open triangles are the stripping cross sections, and the open circles are the capture cross sections for the He-Cs system [65] and the closed circles are those for the He-Rb system [64], respectively. The small closed circles are the capture cross sections for the He-Rb system from Ref. [67].

the Rb vapor thickness increases, is not extremely sensitive to the absolute values of the stripping cross sections and the spin-exchange cross section for  ${}^3\text{He}$  atom. On the other hand, the effect of the growth of  $P_T$  is enhanced by the presence of the spin exchange for  ${}^3\text{He}^+$  ion collisions. This means that there is a possibility that  $P_T$  is increased not by the electron pumping but by the spin-exchange process between  ${}^3\text{He}^+$  ion and Rb.

So, we must ensure that the spin-exchange processes do not contribute significantly to production of the  ${}^3\text{He}^+$  polarization to experimentally verify the principle of the electron pumping. However no experimental and theoretical value of the spin-exchange cross section for  ${}^3\text{He}^+$ -Rb system have been presented so far. So we theoretically calculated the spin-exchange cross section. Next subsection, we will note about this calculation.

### 5.1.3 Spin-exchange cross section

To estimate the spin-exchange cross section, we carried out a calculation by the semiclassical impact parameter method assuming formation of a single molecular state. This procedure succeeded in reproducing the experimental results for the fast H-Rb system [66, 68].

In this formalism, the  $\sigma_{se}$  is given as [66],

$$\sigma_{se} = 2\pi \int_0^\infty b \sin^2 \frac{\phi_{ts}}{2} db, \quad (5.2)$$

$$\phi_{ts} = \int \frac{V_t - V_s}{\hbar} dt = -2 \int_b^\infty \frac{R(V_t - V_s)}{\hbar v \sqrt{R^2 - b^2}} dR. \quad (5.3)$$

Here,  $V_t$  and  $V_s$  are respectively the potential energies of the  $({}^3\text{He-Rb})^+$  molecule in the  $1^3\Sigma$  and  $1^1\Sigma$  ( where  $1\Sigma$  denotes  ${}^3\text{He}^+(1s, {}^2S) - \text{Rb}(5s, {}^2S)$  ) states.  $b$ ,  $R$  and  $v$  are respectively impact parameter, internuclear separation between the Rb atom and the  ${}^3\text{He}^+$  ion, and the incident velocity of the  ${}^3\text{He}^+$  ion. The  $\sigma_{se}$  was calculated as a function of an incident energy of the  ${}^3\text{He}^+$  ion

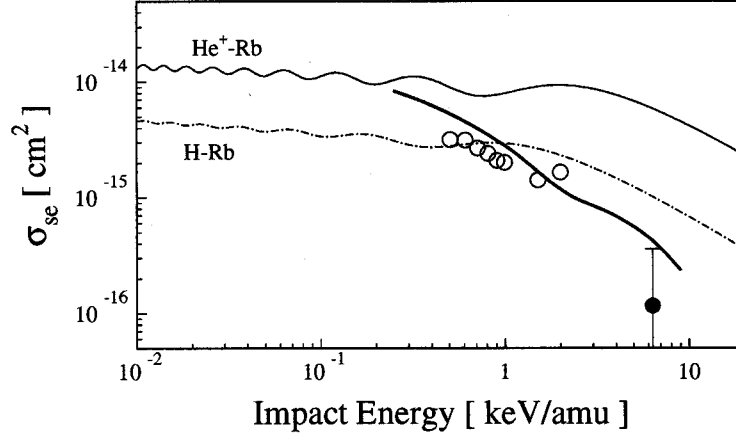


Figure 5.5: Theoretical values of  $\sigma_{se}$  without coupling to other excited states as a function of the incident energy for a H atom (dot-dashed curve) [66], a  ${}^3\text{He}^+$  ion incident on a Rb atom (thin solid curve) and with the coupling for  ${}^3\text{He}^+$  ion (thick solid curve) and experimental values of  $\sigma_{se}$  for the H atom ( $\circ$ ) [68] and the  ${}^3\text{He}^+$  ion ( $\bullet$ ).

by substituting the  $V_{ts}$  for the  ${}^3\text{He}^+\text{-Rb}$  system (see Appendix B) into Eq. (5.3). This result is shown by a solid curve in Fig. 5.5. The experimental data at 6.33 keV/amu, though the detail of the measurement will be presented in the later section, is also shown by a closed circle. For comparison, the results for the H-Rb system are also shown in Fig. 5.5, where the dot-dashed curve is the theoretical result [66] and open circles are the experimental results [68]. The calculation predicts that  $\sigma_{se}$  for the  ${}^3\text{He}^+\text{-Rb}$  system is a several times larger than that for the H-Rb system at all studied energies. This trend is qualitatively understood from Fig. B.3 in terms of the difference in the shape of  $V_{ts}$  between these two systems, i.e.,  $\sigma_{se}$  becomes larger for the  ${}^3\text{He}^+\text{-Rb}$  than for the H-Rb, because  $V_{ts}$  extends to larger  $R$  in the case of  ${}^3\text{He}^+\text{-Rb}$  system (see Appendix B). At 6.33 keV/amu, this cross section is

$$\sigma_{se} = 5.9 \times 10^{-15} \text{ cm}^2. \quad (5.4)$$

In Fig. 5.6, we show the calculated results of the  $P_T$  plotted as a function of the Rb vapor thickness obtained by assuming the above theoretical prediction (dotted curve). The experimental results was also plotted once more. As seen in this figure, the calculation clearly overestimates. On the other hand, it was found from Fig. 5.5 that the theory could reproduce the observed results for the H-Rb system. In other words, the theory used for the H-Rb system could not be applied to the the

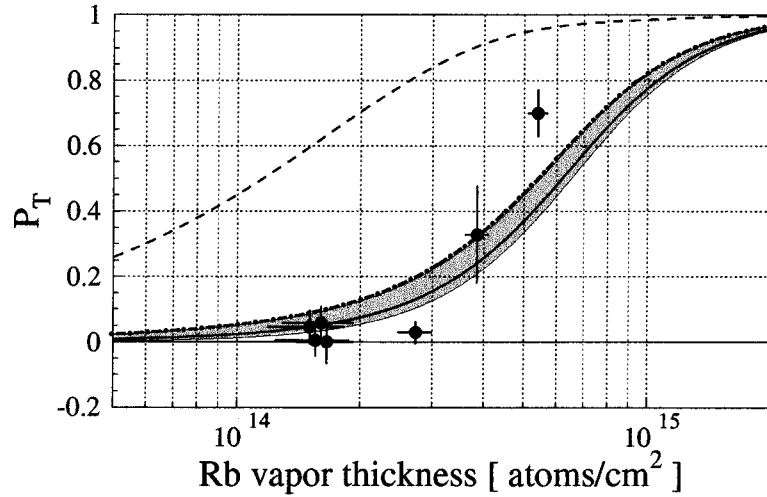


Figure 5.6: Observed  $P_T$  (●) plotted as a function of the Rb vapor thickness. A solid curve shows the theoretical curve with  $\sigma_{se}$  obtained by the  $\chi^2$  fitting method. A shaded area corresponds to the errors of  $\sigma_{se}$ . A dashed curve is the theoretical curve assuming  $\sigma_{se}=5.9\times 10^{-15}$  cm<sup>2</sup> which is calculated by the semi-classical impact parameter method. The dot-dashed curve is the results with the spin-exchange cross section obtained by the calculation of the close coupling method.

<sup>3</sup>He<sup>+</sup>-Rb system, which suggests imperfection of the theory.

For better reproduction, we will travel for more comprehensive calculations as discussed in the next subsection.

#### 5.1.4 Calculation including transition to other states

To estimate the spin-exchange cross section more precisely, a calculation allowing multichannel transitions was carried out by N. Shimakura. To include the transitions, the theory on the basis of the close coupling method was used. Indeed, four states for singlet states and four states for triplet states as shown in Fig. B.1 were included. The impact energy dependence of the calculated results of spin-exchange cross section is indicated by a thick curve in Fig. 5.5. A great reduction is found in comparison with the theory with a single channel. At lower energies two theories predict comparable values, while at higher energies the theory with multi channels predicts much smaller values than the theory with a single channel does. This suggests that transitions to these excited states becomes predominated according as an increase of the incident energy.

At 6.33 keV/amu, the spin-exchange cross section is

$$\sigma_{se} = 0.429 \times 10^{-15} \text{ cm}^2. \quad (5.5)$$

In Fig. 5.6, we show the calculated  $P_T$  plotted as a function of the Rb vapor thickness obtained by assuming the above theoretical prediction (dot-dashed curve). This curve does not contradict with

the experimental result measured at 6.33 keV/amu. If one includes more transition channels, the theoretical value for the  $\sigma_{se}$  would reproduce the experimental results more satisfactorily.

This value is too small to contribute to a certain amount of  $P_T$  in the range of the Rb thickness of  $\sim 10^{14}$ . So, it is found that the observed  $P_T$  was well reproduced mainly by the model calculation including the electron pumping with a minor contribution from the spin-exchange processes. This demonstrates that we could really observe the “electron pumping”.

### 5.1.5 Extraction of experimental value of the spin-exchange cross section

Next, to experimentally evaluate the spin-exchange cross sections,  $\sigma_{se}$ , the experimental results on the Rb vapor thickness dependence of  $P_T$  were fitted by parameterizing the  $\sigma_{se}$  with the  $\chi^2$  fitting method using the rate equations (3.3) of the electron pumping which was described in the chapter 3. In the present  $\chi^2$  fitting, we employed errors combined by experimental errors in the Rb and  $^3\text{He}^+$  polarizations,  $\sigma_p$ , and the errors in the Rb vapor thickness,  $\sigma_\pi$ , as expressed by

$$\sigma = \sqrt{\sigma_p^2 + (dP/d\pi)^2 \sigma_\pi^2}. \quad (5.6)$$

The most probable value of the  $\sigma_{se}$  was derived from the minimum value of  $\chi^2$ ,  $\chi_{\min}^2$  ( $= 20.5$ ), and the error in the  $\sigma_{se}$  was obtained by the deviation of the  $\sigma_{se}$  when the  $\chi^2$  was equal to  $\chi_{\min}^2 \pm \chi_{\min}^2/(n-1)$ , where  $n$  is a data number. To include the errors in the capture and stripping cross sections, the shifts in  $\sigma_{se}$  were evaluated when the capture and stripping cross sections were varied by their errors. The best fitted curve is shown by a solid curve in Fig. 5.6. The spin-exchange cross section is

$$\sigma_{se} = 0.12^{+0.27}_{-0.26} \times 10^{-15} \text{ cm}^2, \quad (5.7)$$

where the errors include a fitting error and errors of the capture and stripping cross sections. The shaded area in Fig. 5.6 corresponds to the errors in Eq. (5.7).

In addition, as a by-product, a striking result is found that the experimental  $\sigma_{se}$  for the  $^3\text{He}^+$ -Rb system is an order of magnitude smaller than the theoretical prediction based on a single channel calculation, while those for the H-Rb system are reasonably reproduced by the theory.

A great reduction of the  $\sigma_{se}$  relative to the theoretical results for the  $^3\text{He}^+$ -Rb system has not been known so far because no experimental data have been available due to the experimental difficulty. This suggests that the collision mechanism for the  $^3\text{He}^+$ -Rb system is much more complex than that for the H-Rb system. In fact, we assumed, in this theory, that only one transition channel for both systems.

In conclusion, it is found that in the  $^3\text{He}^+$ -Rb system the transition effect is much more influential than the H-Rb system. This result is qualitatively explained as follows: In the H-Rb system, the first excited state is the H(1s, $^2\text{S}$ )-Rb(5p, $^2\text{P}$ ). On the other hand, in the  $^3\text{He}^+$ -Rb system, there

are two states between the  $\text{He}^+(1s, ^2S)\text{-Rb}(5S)$  and the  $\text{He}^+(1s, ^2S)\text{-Rb}(5p, ^2P)$ , i.e.,  $\text{He}(1s2s, ^1, ^3S)\text{-Rb}^+$  and  $\text{He}(1s2p, ^1, ^3P)\text{-Rb}^+$ . Due to this fact, the spin-exchange cross sections for the  $^3\text{He}^+\text{-Rb}$  system are reduced.

## 5.2 Optimization of the electron pumping polarized $^3\text{He}$ ion source

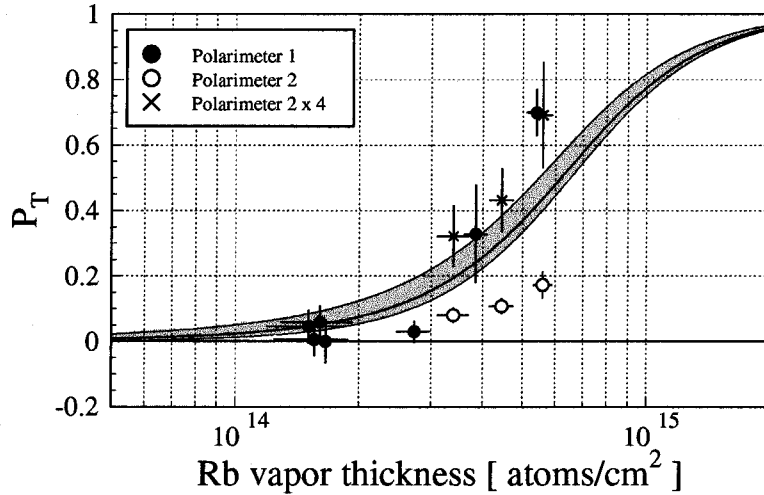


Figure 5.7: Thickness dependence of  $P_T$  measured by the polarimeter 1 (closed circle) and polarimeter 2 (open circle). The cross hairs are obtained  $P_T$  by polarimeter 2 multiplied by a factor 4.

In this section, we discuss an optimization of the electron pumping polarized  $^3\text{He}$  ion source by varying the pumping laser power, an incident  $^3\text{He}^+$  energy, and an ion current of an incident  $^3\text{He}^+$  ion.

For this purpose, we have improved a polarimeter itself so that the distance between a carbon foil and a position of photon detection can be changed precisely. This was done by replacing the polarimeter 1 with the polarimeter 2. With this new polarimeter, we observed the  $^3\text{He}$  polarization as a function of the pumping laser power, the  $^3\text{He}^+$  ion current, and the  $^3\text{He}^+$  impact energy to look for the optimized condition of the electron pumping polarized  $^3\text{He}$  ion source.

At first, we measured the Rb vapor thickness dependence with the polarimeter 2 to compare to the results with the polarimeter 1. The measured polarization transfer coefficients,  $P_T$ , are shown in Fig. 5.7, where the close circles are referred to the data provided by the polarimeter 2 and the open circles are referred to the data provided by the polarimeter 1.

It is found that the data from the polarimeter 2 are reduced to about 1/4 of the data from the polarimeter 1. It is possible that this reduction was caused by the radial localization of Rb polarization or the polarization hole. If the origin is caused by these processes it is considered

that the relative value is reliable. So we discussed below using normalized  $P_T$  measured by the polarimeter 2 by multiplying a factor 4.

### 5.2.1 Dependence on pumping laser power

To see an influence of the pumping laser power upon the  $^3\text{He}^+$  nuclear polarization, the  $P_T$  was measured by varying the pumping laser power.

In this section, at first, we will clarify physics underlying the measurement by showing the theoretical calculation of  $P_T$ , and will compare them with the experimental results. A general trend of the  $^3\text{He}^+$  nuclear polarization is governed primarily by the Rb polarization produced by the laser optical pumping. An areal distribution of the Rb vapor polarization is determined by the pumping laser intensity and the Rb vapor thickness. As discussed in the later section on the relaxation mechanism, the change of the Rb vapor thickness induces a pronounced variation of the radial distribution of the Rb polarization due to the radiation trapping effect. On the other hand, it is easily understood that an intensity of the pumping laser influences only on an axial distribution of the Rb polarization due to the laser absorption by the Rb vapor itself. From the direct measurement of the Rb polarization at a Rb vapor thickness of  $4.8 \times 10^{14}$  atoms/cm<sup>2</sup> by varying the pumping laser intensity, it was found that when the laser power is less than 2 W, the Rb polarization is proportional to the laser power, while for the pumping laser power larger than 2 W, the Rb polarization is saturated. This ensures that an axial distribution of the Rb polarization would be homogeneous in case of the pumping laser power larger than 2 W. On the other hand, when the laser power is less than 2 W, the Rb polarization is expressed by  $P_{\text{Rb}}/P_{\text{Rb}}^{2\text{W}}$ , where  $P_{\text{Rb}}$ , and  $P_{\text{Rb}}^{2\text{W}}$  are, respectively, a Rb polarization at a certain Rb vapor thickness, in this case  $4.8 \times 10^{14}$  atoms/cm<sup>2</sup>, a Rb polarization obtained with a laser power of 2 W at the same thickness. Keeping these things in mind, we try to make a theoretical calculation of  $P_T$ . Firstly, we assume that the Rb vapor thickness ( $\pi$ ) the Rb polarization distribution along the Rb vapor thickness ( $\pi$ ) of is given by

$$P_{\text{Rb}}(\pi) = \frac{P_{\text{Rb}}^{2\text{W}}}{1 + \exp\left(\frac{\pi - \pi_0}{a}\right)}, \quad (5.8)$$

where  $a$  is a diffuseness,  $\pi$  and  $\pi_0$  are, respectively a Rb thickness, and a thickness at which the Rb polarization reduces to a half of the initial polarization. Here, the diffuseness is conveniently defined as  $0.03 \times 10^{15}$  cm<sup>-2</sup>.

Under the above assumption, we solved the rate equations (3.3) at the Rb vapor thickness of  $4.8 \times 10^{14}$  atoms/cm<sup>2</sup> according as the same prescription already given in Chapter 3. The calculated Rb polarizations distribution on the  $z$  direction are shown in Fig. 5.8 for pumping laser powers of 1, 1.5 and 2 W. The observed Stokes parameter,  $P_T$ , and the Rb polarization (open circles) are plotted in Fig. 5.9. The closed circles are the theoretical results.

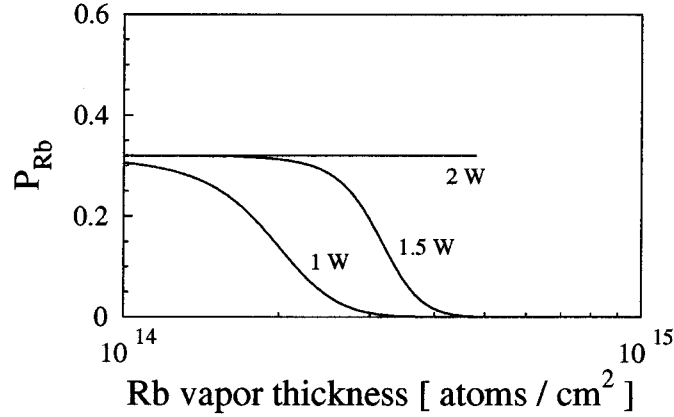


Figure 5.8: The Rb thickness dependence of the Rb polarizations for the pumping laser power of 1, 1.5, and 2 W.

It is found that  $P_T$  is not so influenced by an inhomogeneity of the Rb polarization along the  $z$ -direction. This is due to the fact that we have chosen a Rb vapor thickness at  $\pi = 4.8 \times 10^{14}$  atoms/cm<sup>2</sup>, with which a major contribution of the electron pumping process in the latter half of the Rb vapor is the electron stripping that does not need the polarized Rb vapor.

Finally, we will discuss the experimental results in comparison with the theory. The open circles in Fig. 5.9 are the experimental results of  $P_T$ . The experimental results show unexpectedly a decrease with an increase of the laser power. This is a strange phenomenon which is explained neither theoretically.

### 5.2.2 Dependence on $^3\text{He}^+$ ion current

In this subsection, we will discuss the depolarizations of the Rb and  $^3\text{He}^+$  nuclear polarization induced by a  $^3\text{He}^+$  ion beam penetrating the Rb vapor. For this purpose, we observed both the  $^3\text{He}^+$  polarization and the Rb polarization by varying a  $^3\text{He}^+$  ion current.

The mechanisms of the Rb depolarization and of the  $^3\text{He}^+$  depolarization are, basically, different each other as mentioned in the following scenario. At first, we think about the Rb depolarization. A Rb vapor is ionized by a bombardment of a  $^3\text{He}$  ion as given as follows,



The ionized  $\text{Rb}^+$  may form a molecule composing of the  $\text{Rb}^+ + \text{Rb}$  which induces a depolarization of the Rb vapor. Since the number of such a molecule increases according as an ion current, a sizable Rb depolarization may be expected by an increase of the ion current.

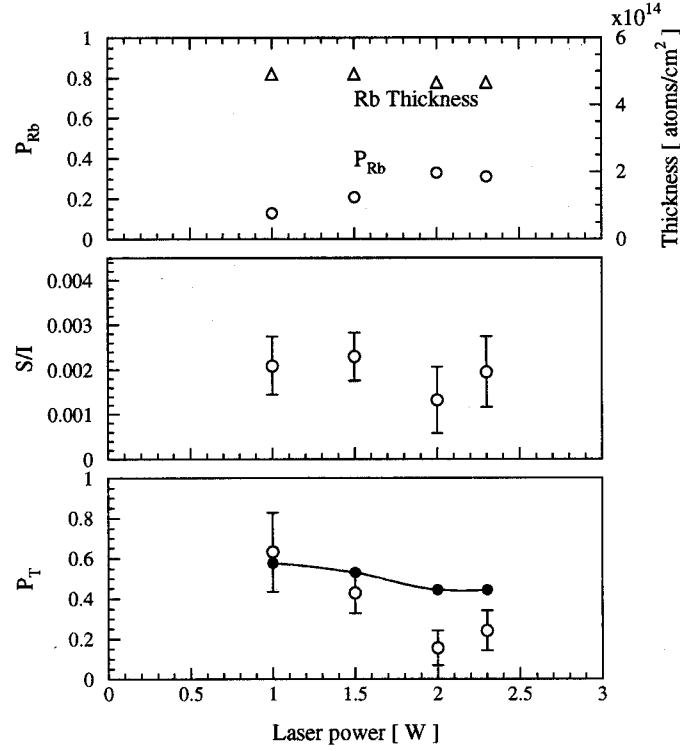


Figure 5.9: The observed Stokes parameter,  $P_T$ , and the Rb polarization (open circles) are plotted. The closed circles indicated are the theoretical results.

In the next step, we think about the  ${}^3\text{He}^+$  depolarization. If a fraction of the  $\text{Rb}^+$  ion increases by the  ${}^3\text{He}^+$  bombardment, an effective thickness of the polarized Rb vapor reduces. Consequently, an efficiency of the electron pumping reduces because of the decrease of the effective Rb vapor thickness, which would eventually make  $P_T$  reduced. When the  ${}^3\text{He}$  ion incident on the Rb vapor, a fraction of the Rb ions is given in Appendix E) as formulated by,

$$F^+ = \frac{1}{1 + R^{-1}}, \quad (5.10)$$

where

$$R = \frac{I\sigma_{10}\rho_{Rb}l}{e(2\pi rl + \pi r^2)} \sqrt{\frac{2\pi m}{kT}}. \quad (5.11)$$

Here, the meaning of parameters used in the above equations are referred to the Appendix E.  $F^+$  is plotted in Fig. 5.10 as a function of an ion current. It is found from this result that the ion fraction is expected to be negligible small in an ion current range less than a few  $\mu\text{A}$ . Keeping the above aspects in mind, an ion current dependence was measured over a range from 100 nA to 300 nA, where an upper limit of the range is due to the limitation on a performance of the duoplasmatron ion source and a lower limit corresponds to the value that the beam-foil spectroscopy

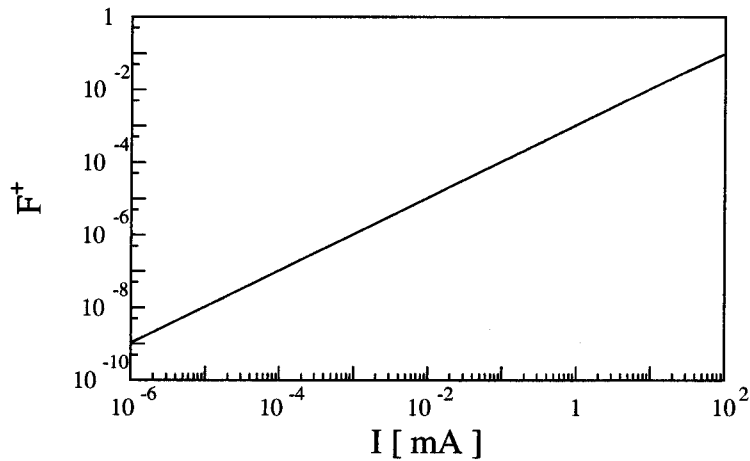


Figure 5.10: Calculated fraction of a  $\text{Rb}^+$  ion plotted as a function of  $^3\text{He}$  ion current

could measure the nuclear polarization reliably free from the instrumental background. The beam current was monitored by a Faraday cup attached at the end of the beam-foil polarimeter. Therefore, the absolute values of the beam current penetrating the Rb vapor cell may be different from these values. This experiment was performed at a Rb thickness of  $5 \times 10^{14}$  atoms/cm<sup>2</sup> and a beam energy of 19keV. Measured  $P_{\text{He}}$  and  $P_{\text{Rb}}$  are plotted as a function of the  $^3\text{He}^+$  beam current. It is concluded that both of  $P_{\text{He}}$  and  $P_{\text{Rb}}$  do not change over the measured current range. This is a reasonable agreement with the results based on the calculated estimate of the  $F^+$  fraction. For practical purpose, a measurement at higher beam current is necessary.

### 5.2.3 Impact energy dependence

In this subsection, we discuss a dependence of  $P_{\text{T}}$  on an  $^3\text{He}^+$  impact energy. The reason why  $P_{\text{T}}$  might depend on the impact energy is simple. It is only because the stripping and capture cross sections for a  $^3\text{He}^+$  ion on a Rb vapor have an impact energy dependence. Indeed, Fig. 5.4 shows the experimental data of these cross sections plotted as a function of impact energy, where the open circles and triangles are the electron capture cross sections and the electron stripping cross sections for the He ions/atoms impact on Cs atoms, respectively [65]. The closed circles are the electron capture cross sections for the  $\text{He}^+$  ions incident on Rb atoms [64]. The electron stripping cross sections increase with an increase of the impact energy while the capture cross sections decrease.

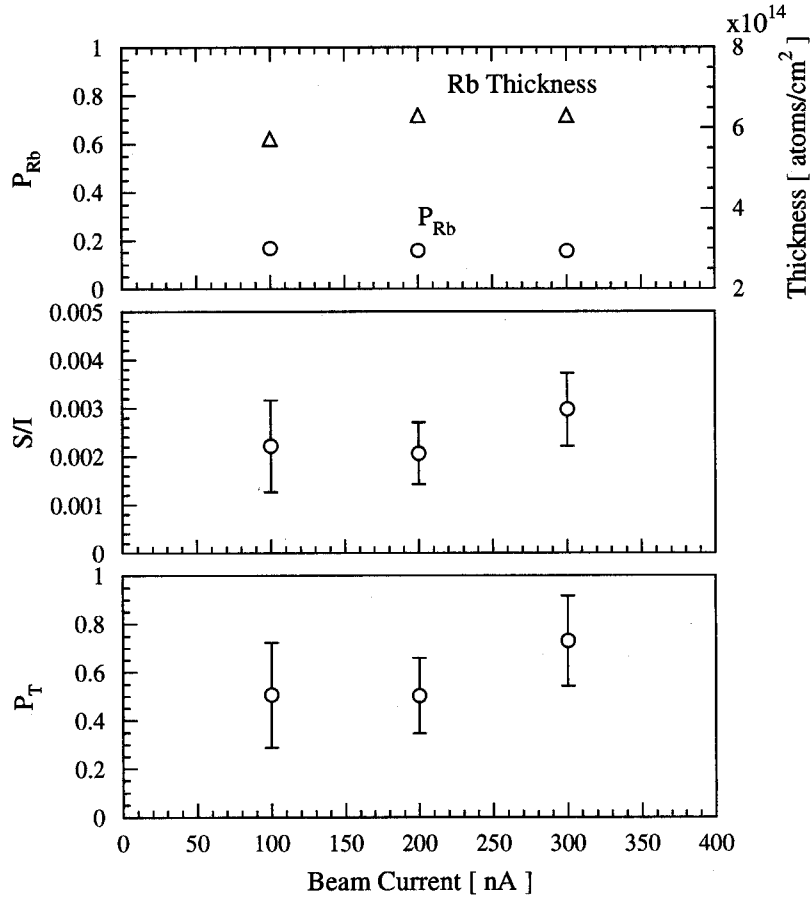


Figure 5.11: Observed  $P_T$ , the Stokes parameter, and the Rb polarization plotted as a function of the  ${}^3\text{He}^+$  current.

We discuss now the experimental details of the impact energy dependence. The energy dependence was measured by changing a second extract voltage of the duoplasmatron ion source in a range from 15 keV to 19 keV. The upper limit is constrained by a discharge problem on the duoplasmatron ion source and a lower one is constrained by a degradation of the ion beam transmission. The experimental data for the  $P_T$  at the Rb thickness at  $5 \times 10^{14}$  atoms/cm<sup>2</sup> are shown in Fig. 5.12 together with the theoretical curve numerically evaluated by solving the rate equations (3.3) as discussed in the chapter 3. No drastic energy dependence of  $P_T$  was observed in an energy range from 15 keV to 19 keV. This tendency is consistent with the theoretical results.

### 5.3 Relaxation of optically pumped Rb vapor

In this section, we will mention one of the important topics in backing-up the principle of the electron pumping, namely, the detailed study on the relaxation mechanism of the Rb vapor. At first,

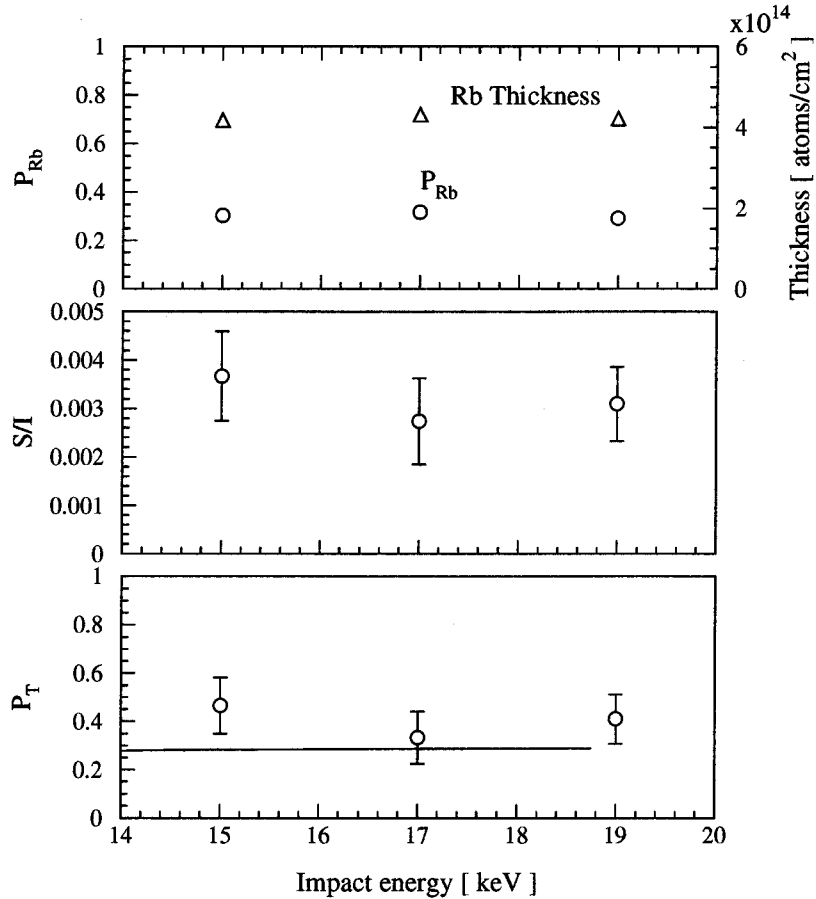


Figure 5.12: Observed  $P_T$ , the Stokes parameter, and the Rb polarization plotted as a function of  ${}^3\text{He}^+$  impact energy. The solid line are results of the theoretical calculation using the measured capture and stripping cross sections shown in Fig. 5.4

we will concentrate on a brief review concerning what kinds of observables have been measured, for what reason they were measured, and then present the experimental results and discussion.

### 5.3.1 A brief review of measurement

The Rb relaxation rates, inverse of the decay time of the Rb polarization, were measured varying the following parameters:

1. The magnetic field ( $B = 1 - 5$  T) for  $T_{\text{cell}} = 125$  °C,
2. the Rb cell temperature ( $T_{\text{cell}} = 90 - 130$  °C) for magnetic fields  $B = 1, 1.5, 2,$  and  $3$  T,
- and 3. the frequency of pumping laser ( $\nu_p = \nu_0 + 110, \nu_0 + 130,$  and  $\nu_0 + 150$  GHz, where  $\nu_0$  is a resonance frequency of the pumping laser without the magnetic field) for  $B = 4$  T and  $T_{\text{cell}} = 125$  °C.

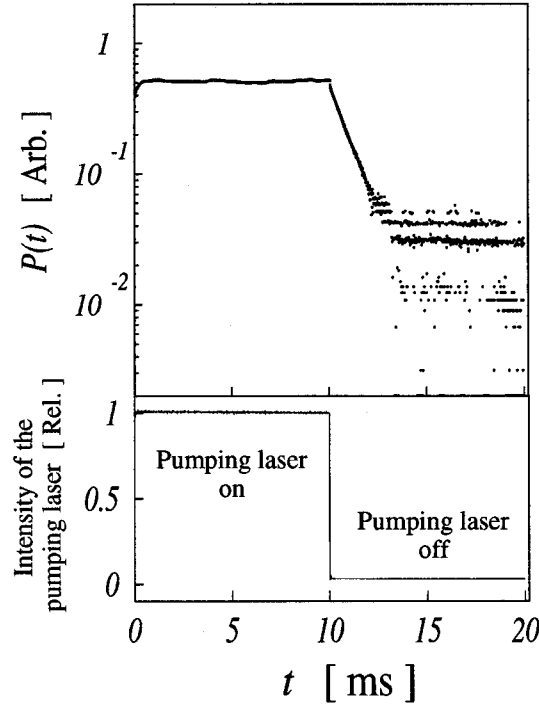


Figure 5.13: A time spectrum of the Rb polarization taken at  $B = 4$  T and  $T_{\text{cell}} = 125$  °C. The solid curve is a time spectrum of intensity for the pumping laser, from which a switching performance could be extracted.

To measure the time spectra of the Rb polarization,  $P(t)$ , we employed an electro-optical shutter (Pockels cell) to chop the pumping laser beam. A laser pulse of 10 ms duration with a switching time of  $\sim 1$   $\mu$ s was employed. The switching time is much shorter than the Rb relaxation time. Fig. 5.13 shows a typical  $P(t)$  as a function of time together with the pumping laser intensity profile. As to be seen there, the laser intensity remains constant for 10 ms and drops to zero level within a  $\mu$ s after the switch off time. This procedure is followed for all  $P(t)$  measurement reported below.

### 5.3.2 Experimental results

#### Time spectra of the Rb polarization

Figs 5.14-(a), 5.14-(b), and 5.14-(c) show the time spectra recorded by changing the magnetic field,  $B$ , the cell temperature,  $T_{\text{cell}}$  for  $B = 2$  T, and the pumping laser frequency,  $\nu_p$ , respectively. From these figures, two features become apparent. The relaxation rates seem to be very sensitive to the external parameters,  $B$ ,  $T_{\text{cell}}$ , and  $\nu_p$ . In each spectrum, there are at least two significant components as typically shown in Fig. 5.15. A fast one has  $T_f \simeq \mu$ s and a slow one  $T_s \simeq$  ms. The

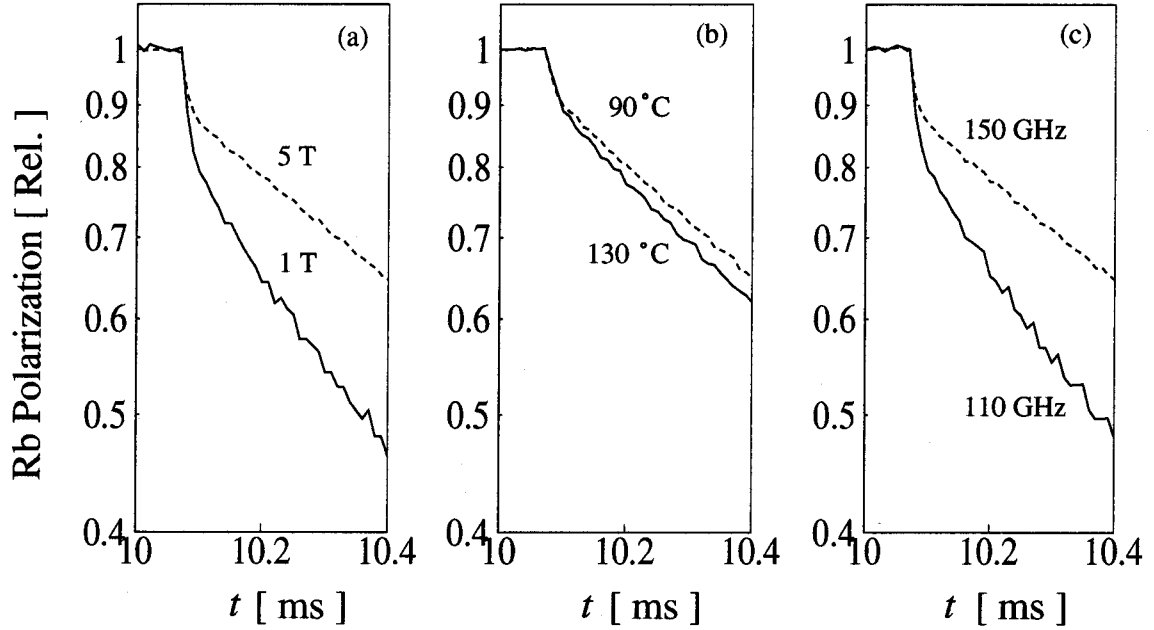


Figure 5.14: Summary of time spectra. (a) Magnetic field dependence taken at  $T_{\text{cell}} = 125$  °C. (b) Rb cell temperature dependence taken at  $B = 4$  T. (c) Pumping laser frequency dependence taken at  $B = 4$  T and  $T_{\text{cell}} = 125$  °C.

relaxation spectrum is, thus, fitted with a two component formula,

$$P(t) = P_f e^{-t/T_f} + P_s e^{-t/T_s} + C, \quad (5.12)$$

where  $P_f$ ,  $T_f$  and  $P_s$  and  $T_s$  are intensities and time constants of fast and slow components, respectively. The constant “ $C$ ” is dark current contribution to the intensity, with no significant effect on the determination of polarization parameters.

In what follows, we summarize the relaxation rates for the fast and slow components individually for  $B$ ,  $T_{\text{cell}}$ , and  $\nu_p$  dependence. For each  $B$ ,  $T_{\text{cell}}$ , and  $\nu_p$  setting, the relaxation rate measurements were repeated several times. The  $T_f$  and  $T_s$  are the weighted means of the fits of those spectra.

### **$B$ dependence**

Fig. 5.16 shows the deduced magnetic field dependence of relaxation rates for the fast (upper part) and slow (lower part) components, respectively. It is found from these results that the relaxation rates for the fast component are almost independent of  $B$ , while those for the slow component monotonically decrease as  $B$  increases and reach a plateau. The solid curves in Fig. 5.16 are the results of the theoretical calculation as described in the next section.

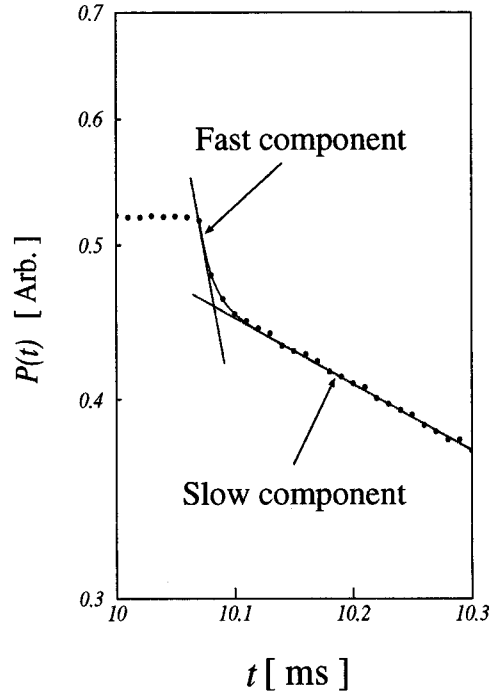


Figure 5.15: Same time spectrum in Fig. 5.13, but a time range between 10.0 and 10.3 ms is expanded.

### $T_{\text{cell}}$ dependence

Fig. 5.17 shows the deduced temperature dependence of relaxation rates for the fast (upper part) and slow (lower part) components, respectively. The fast component shows a steep increase in the relaxation rate as temperature increases for  $B = 1 - 3$  T, nearly independent of the magnetic field. This feature is consistent with the upper part of Fig. 5.16, where the fast component is found to be independent of  $B$ .

The slow component, while it shows increases in the relaxation rates as temperature increases, it exhibits somewhat complex pattern for  $B$ ,  $T_{\text{cell}}$  dependence. Also shown as the solid curves are theoretical results to be discussed in the next section.

### $\nu_p$ dependence

Fig. 5.18 shows the observed relaxation rates for the fast (upper part) and slow (lower part) components plotted as the pumping laser frequency ( $\nu_p$ ) is varied for  $B = 4$  T. In the figure, the abscissa shows  $\Delta\nu_p = \nu_p - \nu_0$ , where  $\nu_0$  is the resonance frequency without the magnetic field. Also indicated on the abscissa is the resonance position along the axis from the center of the Rb cell,

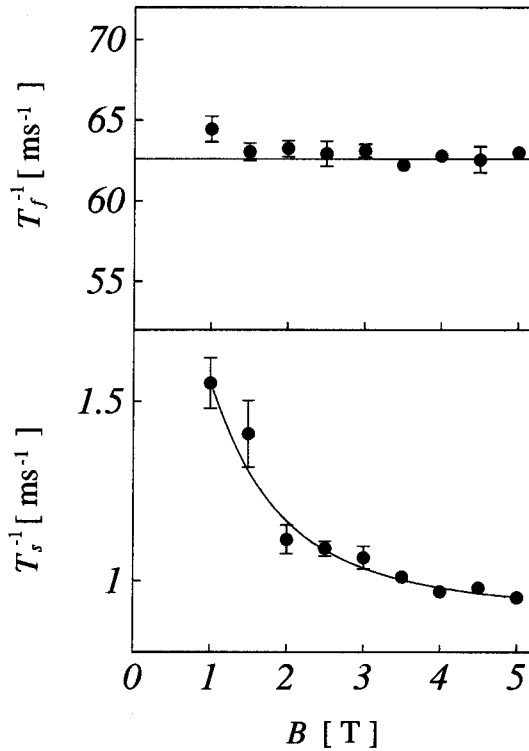


Figure 5.16: The observed relaxation rates plotted as a function of  $B$  for the fast (upper part) and slow (lower part) components. They are taken at  $T_{\text{cell}} = 125$  °C. The solid curves are results of the theoretical calculations (see the text).

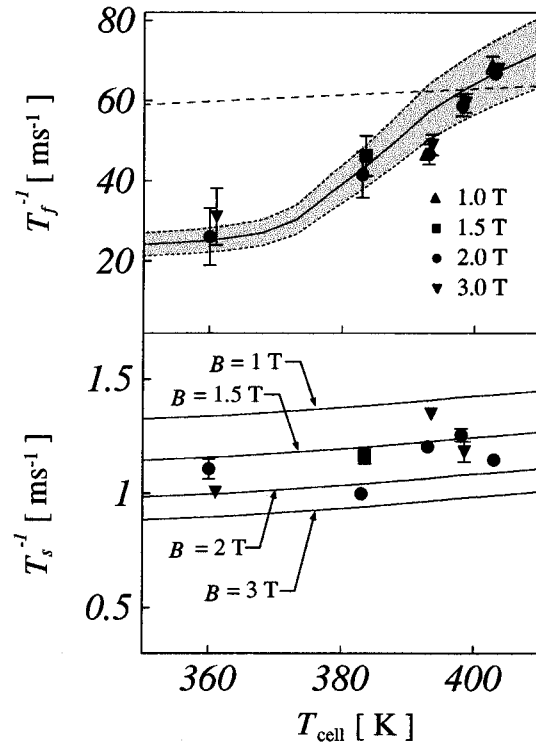


Figure 5.17: The observed relaxation rates plotted as a function of  $T_{\text{cell}}$  for the fast (upper part) and slow (lower part) components. They are taken at  $B = 1.0, 1.5, 2.0,$  and  $3.0$  T. The hatched area and the curves are the result of the theoretical calculations (see the text).

as estimated from the known magnetic field profile. As the line-width of the pumping laser is 20 GHz, at a set frequency, the resonance condition is satisfied by less than half of the cell region. This enables us to study the localization effects. As seen in Fig. 5.18, the fast component is nearly independent of the resonance frequency with a variation less than 3 %, where as the slow component changes by about 50 % as we change  $\nu_p$  by 40 GHz.

### 5.3.3 Comparison of the experimental results with the model calculations

The observed relaxation rates are then compared with the results of the theoretical calculation based on these models.

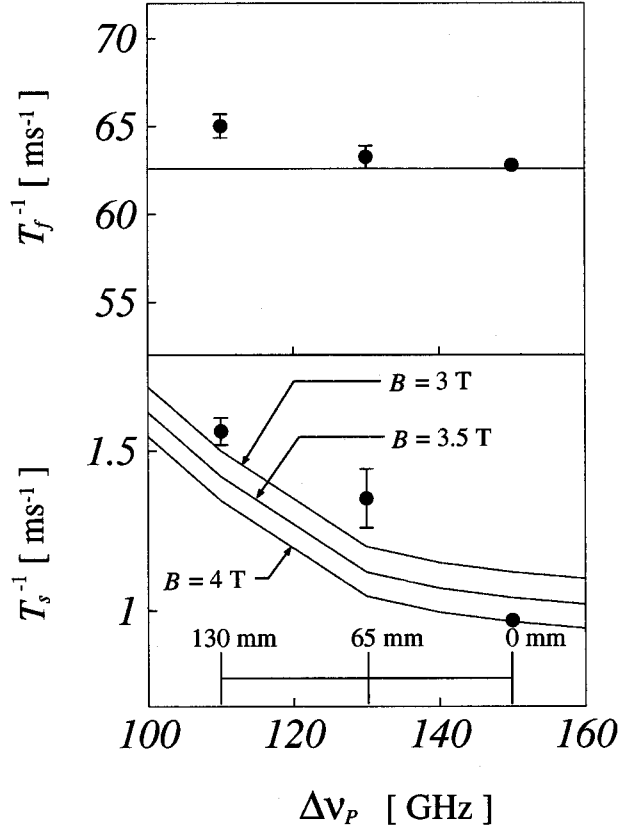


Figure 5.18: The observed relaxation rates plotted as a function of  $\Delta\nu_p$  for the fast (upper part) and slow (lower part) components. They are taken at  $B = 4$  T,  $T_{\text{cell}} = 125$  °C. The curves are the result of the theoretical calculations (see the text).

### Slow component

**$B$  dependence** The relaxation rate for the slow component ( $T_s^{-1}$ ) is given as a sum of the contributions from wall relaxation and effusion processes,  $T_s^{-1} = T_{ws}^{-1} + T_{es}^{-1}$ . The solid curve in the bottom part of the Fig. 5.16 is the best fit curve of the data with the two relaxation processes. The fit parameters thus determined are  $\tau_c = \tau_s = (5.6 \pm 0.5) \times 10^{-12}$  s and  $b = 0.61 \pm 0.10$  T assuming that  $\tau_c = \tau_s$  [40], which are listed in Table 5.2 along with the results of other measurements. As to be seen there, the local magnetic field,  $b$  for a metal like Cu is much larger than that for an insulator like Paraffin. Also, the sticking time,  $\tau_s$  of a metal is very small compared to that of an insulator.

**$T_{\text{cell}}$  dependence** Fig. 5.19 shows a plot of the  $B$ -independent relaxation rates, plotted against the square root of cell temperature. The dotted curve is the numerical evaluation for the effusion model with the parameters of the geometry of the experimental arrangement, i.e.,  $S'/S = 0.6$ ,  $C'/C$

	Atom	Wall material	$B$ (T)	$\tau_c$ ( $\times 10^{-12}$ s)	$\tau_s$ ( $\times 10^{-12}$ s)	$b$ (T)
Present work	Rb	Cu	1.0 - 5.0	$5.6 \pm 0.5$	$5.6 \pm 0.5$	0.61
Levy et al. [40]	Na	Cu	$\leq 1.2$	$19.4 \pm 0.5$	$19.4 \pm 0.5$	$0.214 \pm 0.007$
Bouchiat et al. [38]	Rb	Paraffin	$\leq 0.5$	$\sim 1$	$4 \times 10^2$	$5 \times 10^{-3}$

Table 5.2: Deduced parameters for the wall relaxation, for Rb and Na atoms as optically pumped atoms, for the Cu and Paraffin as the wall materials, for  $B$  as the magnetic field strength in unit of Tesla.  $\tau_c$  and  $\tau_s$  are, respectively, a correlation time and a sticking time in unit of s, and  $b$  is a local magnetic field in unit of T. Except for Ref. [38];  $\tau_c = \tau_s$  is assumed.

= 0.06,  $L = 30$  cm, and  $R = 0.9$  cm. As is seen there, the deduced  $T_{es}^{-1}$  follows the same trend as the calculation, thus indicating that the effusion model is a physically reasonable description. To obtain a quantitative agreement with the data, we performed a Monte Carlo simulation in the framework of the effusion model. The simulation incorporates an angular distribution of the scattering proportional to  $\cos \theta$ , where  $\theta$  is the scattering angle of the Rb atom with respect to the normal to the surface at the point of incidence. We did this calculation for 50,000 test particles. The hatched region is the Monte Carlo results, including the statistical errors. It is seen that the Maxwell's law of velocity distribution with the present geometry and angular distribution is able to reproduce the experimental data.

**$v_p$  dependence** The relaxation rates for the slow component showed a remarkable  $v_p$  dependence as shown in the lower part of Fig. 5.18. This result suggests that the relaxation rates for Rb polarization produced at the Rb cell center is lower than those produced at both ends of the Rb cell. To see it more closely, the relaxation rates due to the effusion,  $T_{es}^{-1}$  are shown in Fig. 5.20.  $v_p$  dependence is intuitively understood in terms of thermal diffusion of the polarized Rb vapor in the cell: The Rb vapor from the center of the cell, effuses predominantly through the slots of the cell. Near the edges, the vapor has an additional path of effusion along the cell axis. Thus the rate of effusion at the edges is higher than at the center. In the presence of magnetic field, the resonance frequencies ( $\nu_p$ ) varies along the cell axis and thus the  $v_p$  dependence is closely tied to the effusion process. To quantitatively examine this picture, a Monte Carlo simulation based on the kinetic theory of gases was performed and the result is shown as the solid curve in Fig. 5.20. The hatched area is the spread of the statistical error of the simulation. A satisfactory agreement between the measurement and the model calculation strongly indicates that the  $v_p$  dependence is mainly determined by the effusion.

Before closing this section, we note that the effusion effect plays a major role in the relaxation mechanism in the presence of strong magnetic field, in contrast to the dominance of wall relaxation effect at low fields. We identified the importance of the effusion effect for the first time in the present work, as we employed much higher magnetic fields than the previous works.

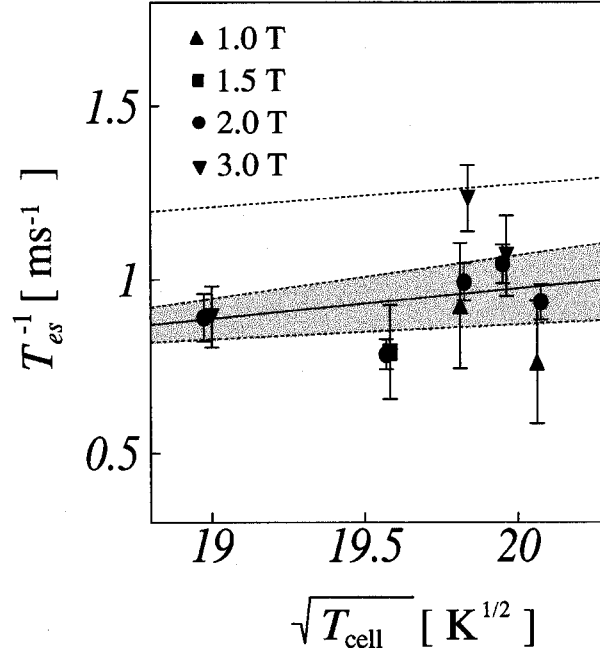


Figure 5.19: The relaxation rates for the slow component are plotted as a function of  $\sqrt{T_{\text{cell}}}$  after the wall relaxation rates were subtracted. The hatched area is the result of the Monte Carlo simulation. The dotted curve is the result obtained by using Eq. (3.16).

### Fast component

As presented in subsection 5.3.2,  $B$ ,  $T_{\text{cell}}$ , and  $v_p$  dependence of the relaxation rates for the fast component are strikingly different from those for the slow component (see Fig. 5.16, Fig. 5.17, and Fig. 5.18), i.e. the  $B$  and  $v_p$  dependence for the fast component are less pronounced, while  $T_{\text{cell}}$  dependence is remarkable. This strongly indicates that the fast component has an origin in a process completely different from the wall relaxation and effusion effect. In order to comprehensively understand the behavior of the fast component, we proposed in the chapter 3, a model in which a sheath of Rb with a higher polarization than that of the surrounding Rb vapor is formed along the pumping laser trajectory. This model predicts that the relaxation rate for the fast component is given by Eq. (3.20). The only unknown parameter in this equation is  $r_0$ , the sheath radius. The dashed line in the upper part of Fig. 5.17 is the temperature dependence of  $T_f^{-1}$  as estimated assuming that  $r_0$  does not vary with  $T_{\text{cell}}$  and the value is 3.7 mm. Clearly, this simple evaluation, showing a slow variation of  $T_f^{-1}$  with  $T_{\text{cell}}$ , fails to reproduce the observed steep change with temperature. It is easily recognized that  $r_0$ , the sheath radius will vary with  $T_{\text{cell}}$  (Fig. 4.13). To incorporate this aspect quantitatively, we performed another Monte Carlo simulation which was discussed in Appendix C.

On the basis of the above expectation, we deduce  $r_0$  at each  $T_{\text{cell}}$  by using Eq. (3.20) so that

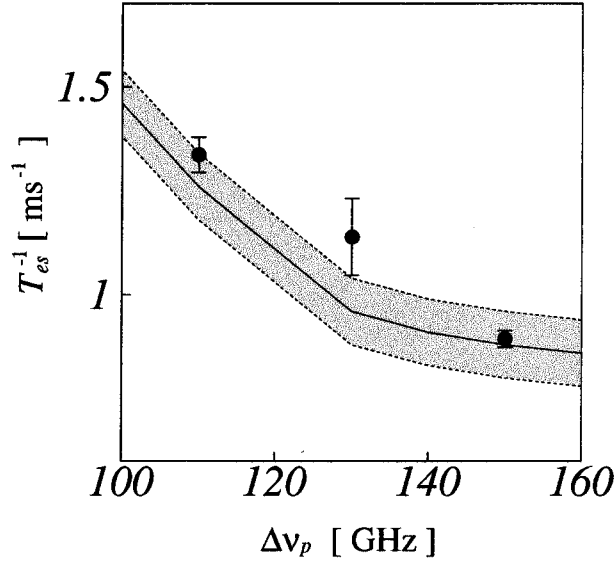


Figure 5.20: The observed relaxation rates for the slow component are plotted as a function of the resonance frequency shift after the wall relaxation rates were subtracted. The hatched area is the result of the Monte Carlo simulation.

the theory might reproduce the observed results. The result is shown in Fig. 5.22. It is found that  $r_0$  decreases as  $T_{\text{cell}}$  increases as qualitatively understood in terms of the effect of the radiation trapping. The Rb polarization is calculated as a function of  $r$ , the radial distance from the pumping laser (the laser spot size is 3 mm) and the results are shown in Fig. 5.21. The  $r_0$ 's are defined as the radius at which the Rb polarization is reduced to  $\sim 5\%$  of the maximum. The result is shown as hatched area in Fig. 5.22. Clearly, the calculation well reproduces the  $T_{\text{cell}}$  dependence of  $r_0$ . With the  $r_0$  parameters thus determined, we plotted the relaxation rates for the fast component shown as hatched area in the upper part of Fig. 5.17. Once again, there is a good agreement between the observed relaxation rates and the calculated ones. These results are convincing proof of the validity of the model proposed for the fast component.

From the fact that there is no pronounced  $\nu_p$  dependence as shown in Fig. 5.18 and from Eq. (3.20), it is suggested that the sheath spreads homogeneously in the axial direction.

### 5.3.4 Conclusion from study on Rb relaxation

The relaxation rates of the optically pumped Rb atoms of high density vapor in the presence of strong magnetic field were observed time differentially with a chopped pumping laser light. The observed time spectra of the Rb polarization clearly demonstrated the presence of two relaxation components; a slow component with  $T_s^{-1} \sim 1 \text{ ms}^{-1}$ , and a fast component with  $T_f^{-1} \sim 65 \text{ ms}^{-1}$ . The relaxation rates for these components were deduced as functions of the magnetic field, the Rb

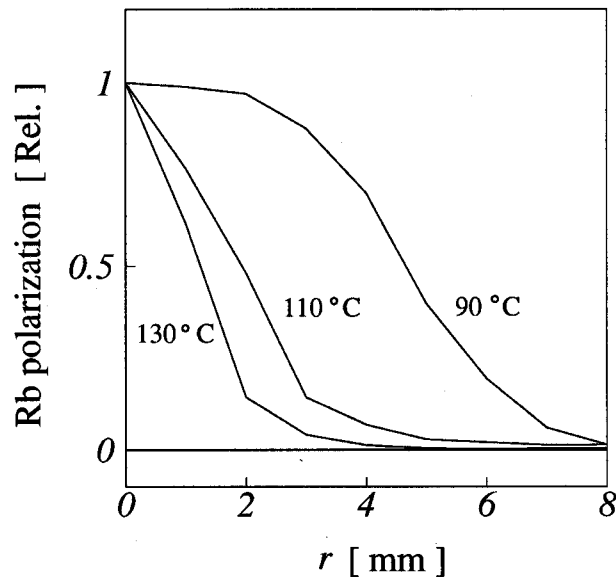


Figure 5.21: The Rb polarization plotted as a function of the radius obtained from the Monte Carlo simulation. The solid curves are derived at the Rb vapor density of  $2.0 \times 10^{13}$  atoms/cm<sup>3</sup> ( $T_{\text{cell}} = 130$  °C),  $0.8 \times 10^{13}$  atoms/cm<sup>3</sup> ( $T_{\text{cell}} = 110$  °C), and  $0.2 \times 10^{13}$  atoms/cm<sup>3</sup> ( $T_{\text{cell}} = 90$  °C), respectively.

cell temperature, and the pumping laser frequency, and quantitative evaluation of the data against possible physical models are done.

In the previous studies, the slow component was known to be caused by the wall relaxation process for low vapor densities and weak magnetic fields. The present analysis confirmed the presence of an additional relaxation mechanism independent of the magnetic field and succeeded in accounting for this component in terms of the effusion.

The fast component, on the other hand, was not well recognized in the previous studies. The present analysis demonstrated that this component is caused by the relaxation process of the highly polarized sheath of the Rb vapor along the pumping laser path.

#### 5.4 Possible origin of reduction of <sup>3</sup>He polarization

The <sup>3</sup>He polarization observed with the polarimeter 2 could not reproduce the value observed with the polarimeter 1. It is striking that an amount of the <sup>3</sup>He polarization is reduced by about a factor 4. In this section, we will discuss about the origin of this reduction.

We see that a relative position between two polarimeters has been changed as shown in Fig. 5.23, the polarimeter 1 is located at the lower beam transport than the polarimeter 2. This requires the change of the beam transport. Another important modification was that in the po-

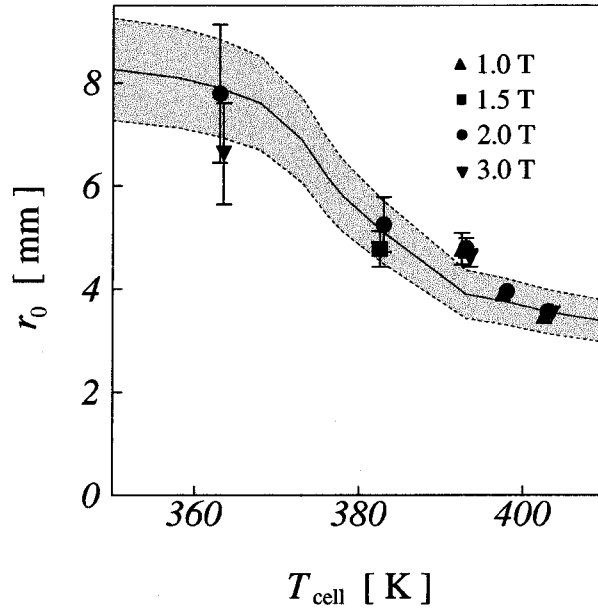


Figure 5.22:  $r_0$  deduced from Fig. 5.17 (upper part) by assuming Eq. (3.20). The hatched area is the result of the Monte Carlo simulation.

larimeter 2 we used a smaller slit, which eventually changed an acceptance aperture.

A performance test of the polarimeter system was carried out by producing a polarized  $^3\text{He}$  atom by means of the tilted foil method which was mentioned in the section 4.1.5. Through this test, a large difference between the values observed by the above two polarimeters was not seen.

Under these circumstances, we will discuss possible causes of the reduction of the  $^3\text{He}$  polarization keeping it in mind that the origin of the reduction might be related to the change of ion beam optics. We can refer two possible candidates for the cause of the reduction.

#### 5.4.1 Radial localization of Rb polarization

As discussed in Sec. 5.3 the Rb polarization is localized near the region exposed by the pumping laser light. Fig. 5.21 shows that the polarized region of the Rb vapor calculated by the Monte Carlo simulation with a Rb vapor thickness of  $5 \times 10^{14}$  atoms/cm<sup>2</sup> is about 2 mm at FWHM. If a  $^3\text{He}$  ion beam is incident on a Rb vapor with a spot size larger than the Rb polarized region or deviates from this polarized region, an obtainable  $^3\text{He}$  nuclear polarization should be reduced. Provided a spot diameter of an initial ion beam is 8 mm, an overlapping region with a polarized Rb vapor is only 1/4 of the total  $^3\text{He}^+$  ion beam. As a result, an observed polarization of  $^3\text{He}$  is reduced to 1/4 of theoretical prediction.

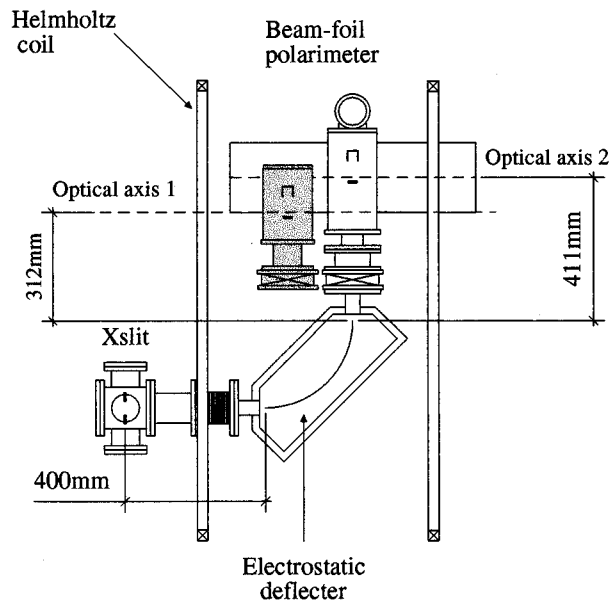


Figure 5.23: Relative position of the beam-foil polarimeter 1, and 2. The shaded polarimeter shows the polarimeter 1 which is drawn at left side position to be visible. The another polarimeter is the polarimeter 2 which is drawn at normal position. The dashed lines are optical axis for the polarimeter 1 and 2.

#### 5.4.2 Polarization hole effect

As discussed in Chap. 3 the "polarization hole" produced by the electron pumping effect may be another candidate for the reduction of the  $^3\text{He}$  polarization. The polarization hole is a phenomenon that the  $^3\text{He}$  polarization becomes small around the center of the ion beam axis, while the beam intensity distribution is homogeneous, even if the Rb vapor has a uniformly distributed polarization over the Rb vapor cell volume. The detailed shape of the hole depends on the condition of the ion beam. If only the region of the hole, unfortunately, happens to be observed by the polarimeter 2, the measured polarization must be reduced. Since the acceptance of the polarimeter 2 is, indeed, smaller than that of the polarimeter 1, it is probable that only the region of the hole might be measured by the polarimeter 2.

## Chapter 6

# Future prospect

In this chapter, we will discuss a feasibility of the  $^3\text{He}$  ion source as a practical device on the basis of the results obtained through the present work and applications with polarized  $^3\text{He}$  ion beam.

### 6.1 Feasibility of the electron pumping ion source

#### 6.1.1 Definition of $Q$ factor, figure of merit

We define a normalized  $Q$  factor which characterizes a performance of the polarized ion source for the further discussion by

$$Q = P^2 \times F, \quad (6.1)$$

$$F = I_{\text{out}}/I_{\text{in}}, \quad (6.2)$$

where  $P$ ,  $I_{\text{out}}$ , and  $I_{\text{in}}$  are, respectively, a  $^3\text{He}$  nuclear polarization, an output polarized  $^3\text{He}^+$  beam current by this polarized ion source and an input unpolarized  $^3\text{He}^+$  beam current.

#### 6.1.2 Improvement of $^3\text{He}$ polarization

The maximum polarization so far recorded with the present device was 0.055. Of course, this value is insufficient for a practical ion source but will be simply enlarged by the following improvements; realization of a thick alkali-metal vapor with a high polarization and a use of the Sona transition, where the Sona transition can convert an electron polarization to a nuclear one with an efficiency of 100 % [26]. The realization of the thick Rb vapor with a high polarization is not so easy even if the intense pumping lasers are available as discussed in the preceding chapter. To overcome this difficulty, a novel method has been required. Recently, a breakthrough was made by the group from the TRIUMF [69]. This is an optical pumping of a Rb vapor mixed with a Cs vapor. Since this method produces both of the Rb and Cs polarizations, a highly polarized ( $\leq 0.9$ ) alkali-metal vapor consisting of the Rb + Cs vapors whose total thickness ( $\sim 1 \times 10^{15}$ ) is thick enough for the

electron pumping can be obtained. The creation of the polarization hole was suggested. This makes the inhomogeneity distribution that  $^3\text{He}$  polarization sinks around the center of beam axis. However, this effect is reduced by using a collinear beam with respect to the beam axis.

### 6.1.3 Improvement of $^3\text{He}^+$ beam current

We have used a duoplasmatron ion source to produce an unpolarized  $^3\text{He}^+$  beam current. Our duoplasmatron, unfortunately, has produced only  $200\ \mu\text{A}$   $^3\text{He}^+$  beam. However, if our ion source be replaced with an ECR ion source, it will be not so difficult to produce a more intense  $^3\text{He}^+$  beam current, say, about  $\sim 2\text{-mA}$   $^3\text{He}^+$  with a compact ECR ion source like a NANOGUN. An improvement of the beam transport system is also necessary.

## 6.2 Evaluation of $Q$ factor for electron pumping polarized ion source

Here, we will evaluate an optimized condition of the electron pumping. For this purpose, we will evaluate the  $Q$  factors at an arbitrary  $^3\text{He}^+$  impact energy and an arbitrary thickness of the Rb vapor fully polarized.

We start with an intuitive consideration. An equilibrated  $^3\text{He}^+$  fraction is estimated to be 0.15 with an incidence of a 19 keV  $^3\text{He}$  (the upper figure in Fig. 6.1). A beam emittance degradation due to the charge exchange collisions under a high magnetic field may be lightened by using a collinear beam with respect to the beam axis. Therefore, it is expected that the polarized  $^3\text{He}^+$  beam current more than  $300\ \mu\text{A}$  would be extracted after the electron pumping processes, where the  $^3\text{He}$  polarization generated would almost reach the Rb polarization.

Keeping this in mind, we will extend the above discussion to the general case. The  $Q$  factors calculated with the rate equations (3.3) in the Chap. 3 are plotted as a function of the Rb vapor thickness at different  $^3\text{He}$  impact energies in Fig. 6.1. This figure clearly demonstrates the performance of the electron pumping polarized ion source. In the upper figure, the thick (thin) solid curve is the calculated result of the  $^3\text{He}^+$  polarization,  $P$  ( $^3\text{He}^+$  fraction,  $F$ ) at an  $^3\text{He}^+$  impact energy of 6.33 keV/amu assuming the full Rb polarization. The dashed curve is the calculated result of the  $P \times 25$  at the same  $^3\text{He}^+$  impact energy, but the polarization of the Rb vapor is assumed to follow the measured values in the present work (Note that the  $P$  multiplied by 25 are plotted!). The thick (thin) dash-dot curve is the calculated result of the  $P$  ( $F$ ) at an  $^3\text{He}^+$  impact energy of 0.1 keV/amu. The calculated  $Q$  factors are shown in the lower figure. The meaning of type of these curves is same as the upper figure. With the present device, we have a maximum value of  $Q$  factor of 0.01 at the Rb vapor thickness of  $5 \times 10^{14}$  atoms/cm<sup>2</sup>.

From this result it is suggested that as long as it is concerned with the present device, the performance is orders of magnitude smaller than that of the ideal case. In addition, it is suggested that by reducing the  $^3\text{He}^+$  impact energy down to 0.1 keV/amu a larger  $Q$  factor might be obtained than that at 6.33 keV/amu. In the dot-dashed curve, a broad maximum is obvious at the Rb

vapor thickness around  $1 \times 10^{14}$  atoms/cm<sup>2</sup>. This is due to an enhanced cross section of the spin-exchange process as mentioned already in the preceding chapter. Another important point with this low energy behavior is that a Rb vapor thinner than that needed for the higher <sup>3</sup>He<sup>+</sup> impact energy is available. This is a great advantage because a high polarization with a thin Rb vapor is easily obtained.

### 6.3 Possibility of spin-exchange polarized ion source

In this section, we will discuss the more detail about the spin-exchange effect on the electron pumping polarized <sup>3</sup>He ion source. As a matter of fact, the polarized proton ion source based on the spin-exchange collisions has been rigorously studied by A. N. Zelenski [68].

As discussed in the preceding chapter already, the spin-exchange cross section has a pronounced impact energy dependence;  $10^{-16}$  cm<sup>2</sup> at 6.33 keV/amu greatly increases  $1.0 \times 10^{-14}$  cm<sup>2</sup> at 0.1 keV/amu. On the contrary, though the electron capture cross section does not change drastically, the electron stripping cross section drastically decreases according to decrease of a <sup>3</sup>He impact energy. In consequence, at such a low energy region, the electron pumping plays a minor role. This is, in fact, the results shown by the dot-dash curves in Fig. 6.1, where the following parameters are used for the present calculation:  $1.1 \times 10^{-14}$  cm<sup>2</sup> for the spin-exchange cross section,  $8.2 \times 10^{-15}$  cm<sup>2</sup> for the electron capture cross section [67],  $0.02 \times 10^{-15}$  cm<sup>2</sup> for the triplet electron stripping cross section extrapolated from the experimental data by A. S. Schlachter et. al. [65], and the electron stripping cross section for the singlet <sup>3</sup>He atoms is neglected. It is concluded that at a low energy region such as at 0.1 keV/amu, the <sup>3</sup>He polarization is generated not by the electron pumping but by the spin-exchange collisions.

We now try to compare the performances of the electron pumping polarized <sup>3</sup>He ion source with the spin-exchange polarized <sup>3</sup>He ion source. It is found from Fig. 6.1 that the maximum value of  $Q$  for the electron pumping type is 0.15, while that of  $Q$  for the spin-exchange type is 0.2. Though these values are comparable each other, a great advantage of the spin-exchange type is use of a polarized thin Rb vapor which can be produced easily without various difficulties such as a spatially inhomogeneity of the polarized Rb vapor, reduction of the Rb polarization etc. as discussed in the former part of the present work. In addition, the use of the thin Rb vapor has a great merit in reducing the beam emittance growth due to the multiple collisions [52].

### 6.4 Application of polarized <sup>3</sup>He ion source

In our present work, we could experimentally prove the validity of the "electron pumping". The establishment of the electron pumping method will hopefully push the construction of a practical polarized <sup>3</sup>He ion source for nuclear physics at an intermediate energy region. In this case, the choice of the spin-exchange polarized <sup>3</sup>He ion source may be another choice in addition to the

electron pumping ion source. On the other hand, there has been a growing demand to accelerate polarized  $^3\text{He}$  beams by the colliders such as RHIC at Brookhaven, and HERA at Desy. One of the physical motivations of the above facilities is to clarify the quark structure of the neutron as a counterpart of the proton. It may be timely to think about the development of the electron pumping polarized  $^3\text{He}$  ion source with improved performances in order to dedicate it to the above facilities.

On the other hand, a polarized  $^3\text{He}$  beam may be applied to the fields other than nuclear and particle physics including, for example, plasma fusions, astrophysics, biomedical field, etc. [2].

The electron pumping itself is regarded as a generalized technique of the optical pumping. This may open up a new application field in the science. For example, the electron pumping may polarize atoms or ions even if the optical pumping could not polarize them because the pumping lasers are not available.

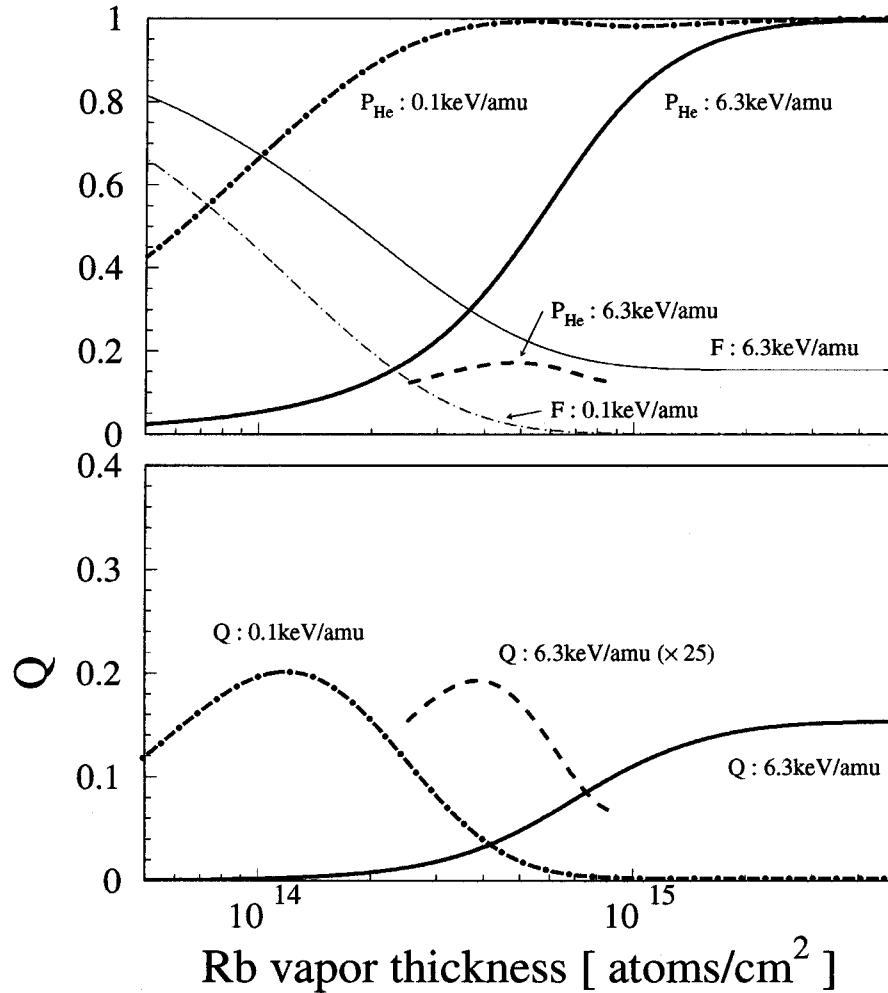


Figure 6.1:  $^3\text{He}$  polarization,  $^3\text{He}^+$  fraction, and calculated  $Q$  factors ( $=P^2F$ ) plotted as a function of the Rb vapor thickness at different  $^3\text{He}$  impact energies. In the upper figure, the thick (thin) solid curve is the result for  $P_{\text{He}}$  ( $F$ ) assuming a full polarization for the Rb vapor at an  $^3\text{He}$  impact energy of  $6.33 \text{ keV/amu}$ . The thick dotted curve is the result for the  $P_{\text{He}}$  at an  $^3\text{He}$  impact energy of  $6.33 \text{ keV/amu}$  assuming the experimentally deduced Rb polarization. The thick (thin) dot-dashed curve is those calculated assuming a full polarization of the Rb vapor with an  $^3\text{He}$  impact energy of  $0.1 \text{ keV/amu}$ . In the lower figure, the curves show the result for  $Q$ . The meanings of curve type are same as the upper figure.

## Chapter 7

# Conclusion

We have developed a polarized  $^3\text{He}$  ion source to use a polarized  $^3\text{He}$  ion beam for nuclear physics at an intermediate energy region. A novel method was proposed to produce a highly polarized  $^3\text{He}$  beam with a high intensity as an alternative method to overcome the following serious difficulties in the OPPIS ( Optical Pumping Polarized Ion Source ) well established in producing a polarized proton beam; a large depolarization due to an insufficient LS decoupling scheme, and a beam emittance growth due to the charge exchanging collisions in the strong magnetic field. This method is called an "electron pumping" because this method utilizing polarized electrons is considered to be an extended concept of the optical pumping by polarized photons.

Our first goal was to experimentally verify the principle of the electron pumping. For this purpose, we constructed a bench test device composing of a duoplasmatron ion source to produce an unpolarized  $^3\text{He}^+$  ion, an analyzing magnet for momentum selection of the ion , a Rb vapor cell and a superconducting solenoidal coil, an electrostatic deflector to select the polarized ion, a polarimeter based on the beam foil spectroscopy, and a laser system for the optical pumping and monitoring. The data taking and the device control were performed with the computer. With this system, we measured a polarization transfer coefficient,  $P_T$  defined by a ratio of the  $^3\text{He}$  polarization to the Rb polarization as a function of the Rb vapor thickness at an impact energy of 6.33 keV/amu. A theoretical calculation on the electron pumping predicted a characteristic behavior of  $P_T$  depending on the the Rb vapor thickness. The theory consistently reproduced the observed trend of  $P_T$  with the reasonable parameters, such as the capture and stripping cross sections. From this fitting result, we concluded that the electron pumping could gain a firm position as a novel technology in polarization physics.

In summary, we could successfully produce a 6.33-keV/amu polarized  $^3\text{He}^+$  ion beam with a polarization degree of 0.055 and an ion current of  $2 \mu\text{A}$  under the following conditions; the Rb polarization and thickness were 0.16 and  $5.5 \times 10^{14}$  atoms/cm<sup>2</sup>, respectively.

The direction of our activities was, then, oriented to the detailed study on the electron pumping indispensable to make this method reliable, i.e., the relaxation mechanism of the Rb vapor, and

the spin-exchange processes between a  $^3\text{He}^+$  ion and a Rb atom. The former study is of practical importance in order to comprehensively understand the complex behavior of the Rb polarization occurring in the Rb vapor with an extremely high density since this structure influences on the final  $^3\text{He}^+$  nuclear polarization. The latter study is of fundamental importance in concluding that we really succeeded in proving the principle of the electron pumping, since the spin-exchange processes also contribute to polarize  $^3\text{He}^+$  ion.

To study the relaxation mechanisms of the Rb polarization, a pulsed pumping laser was used to measure the relaxation times of the Rb polarization. The observed results taken by varying the external magnetic field, the Rb cell temperature, and the position of the polarized region were successfully analyzed by the models based on the relaxation by the cell wall, the relaxation due to effusion caused by a gas kinematics of the Rb atom, and the radiation trapping effect. It was found that a major relaxation mechanism at a high magnetic field is the effusion with a less contribution from the wall relaxation. It was also concluded through the above study that the radiation trapping effect played a substantial role in forming a sheath with a high Rb polarization along the pumping laser whose radius depends significantly on the Rb vapor thickness.

The study on the spin-exchange processes started with a reanalysis of the Rb thickness dependence of  $P_T$ . The reanalyzed value of the spin-exchange cross section was orders of magnitudes smaller than the theoretical value evaluated by the semi-classical impact parameter method assuming formation of a quasimolecule composed of a Rb atom and a  $^3\text{He}^+$  ion. This was striking contrast with the case of the H-Rb system for which the theory could reasonably reproduce the observation. To solve this discrepancy, we further refined a theoretical calculation to allow many transition channels to the final state. As a result, the theoretical value was reduced and became quantitatively equal to the observed value. Another important product of our work obtained through the study on the spin-exchange processes is associated with a proposal of a new type of a polarized  $^3\text{He}$  ion source. The theoretical calculation suggested that the spin-exchange cross section increases by lowering a  $^3\text{He}^+$  impact energy. If we choose a  $^3\text{He}^+$  impact energy of, for example, 0.1 keV/amu, the  $^3\text{He}^+$  polarization would be solely determined by the spin-exchange processes with almost no contribution from the electron pumping. The greatest merit of the spin-exchange polarized  $^3\text{He}$  ion source is that one does not need a thick Rb vapor which is difficult to be highly polarized.

# Acknowledgment

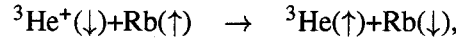
I thank Professor M. Tanaka for giving me a chance to join the project of the construction of  $^3\text{He}$  ion source, and for helping to overcome difficulties appeared in many places throughout the present work. I wish to express my gratitude to Professor T. Yamagata for the continuing guidance and encouragement. I would like to express the appreciation to K. Yonehara and T. Takeuchi for frequent, stimulating and helpful discussion as co-worker. I wish to thank Professor K. Hatanaka for his helpful advice. I am grateful to Professor N. Shimakura for his help in the calculation of spin-exchange cross section. I also would like to express the appreciation to Dr. M. Fujiwara for giving us valuable suggestions and discussions. I am grateful to RCNP ex-director, H. Ejiri for encouragement. I am greatly indebted to Dr. A. Tamii and Dr. H. Akimune for suggestions in the computer data taking and control system. I am pleased to acknowledge the fruitful discussion of Dr. T. Shimoda and S. Shimizu. I should like to express my grateful thanks to staffs of Research Center for Nuclear Physics and Sumitomo Accelerator Service for their technical supports and advice.

## Appendix A

# Mechanism of spin-exchange

Here, we will describe the mechanism of spin-exchange for  ${}^3\text{He}^+$ -Rb impact on Rb atom and derive the cross section formula.

The spin-exchange occurs through the exchange of electrons. Here, we consider the following exchange process;



where the direction of arrow indicates the direction of the spin of an electron of  ${}^3\text{He}^+$  ion and a valence electron of Rb atom. To derive the cross section for above process, firstly we will describe the wave function for  ${}^3\text{He}^+$ -Rb system.

In  ${}^3\text{He}^+$ -Rb system, wave functions for singlet and triplet states are respectively given as

$$\Phi_{1\Sigma} = \frac{1}{2} \{ \alpha(1)\beta(2) - \beta(1)\alpha(2) \} \{ \phi_{\text{Rb}}(1)\phi_{\text{He}}(2) + \phi_{\text{He}}(1)\phi_{\text{Rb}}(2) \} \quad (\text{A.1})$$

$$\Phi_{3\Sigma} = \frac{1}{2} \{ \alpha(1)\beta(2) + \beta(1)\alpha(2) \} \{ \phi_{\text{Rb}}(1)\phi_{\text{He}}(2) - \phi_{\text{He}}(1)\phi_{\text{Rb}}(2) \}, \quad (\text{A.2})$$

where  $\alpha(\beta)$  is the electron spin-up(-down) wavefunction and  $\phi_{\text{He}}$  and  $\phi_{\text{Rb}}$  are the spatial parts of wave functions for  ${}^3\text{He}^+$  ion and Rb atom, respectively.

Then, the wave function that Rb atom has  $M = +1/2$  and  ${}^3\text{He}$  ion has  $M = -1/2$  is written as

$$\Psi_{\text{I}} = \frac{1}{\sqrt{2}} \begin{vmatrix} \alpha(1)\phi_{\text{Rb}}(1) & \beta(1)\phi_{\text{He}}(1) \\ \alpha(2)\phi_{\text{Rb}}(2) & \beta(2)\phi_{\text{He}}(2) \end{vmatrix} \quad (\text{A.3})$$

$$= \frac{1}{\sqrt{2}} \{ \alpha(1)\phi_{\text{Rb}}(1)\beta(2)\phi_{\text{He}}(2) - \alpha(2)\phi_{\text{Rb}}(2)\beta(1)\phi_{\text{He}}(1) \} \quad (\text{A.4})$$

and, the wave function that Rb atom has  $M = -1/2$  and  ${}^3\text{He}$  ion has  $M = +1/2$  is written as

$$\Psi_{\text{II}} = \frac{1}{\sqrt{2}} \begin{vmatrix} \beta(1)\phi_{\text{Rb}}(1) & \alpha(1)\phi_{\text{He}}(1) \\ \beta(2)\phi_{\text{Rb}}(2) & \alpha(2)\phi_{\text{He}}(2) \end{vmatrix} \quad (\text{A.5})$$

$$= \frac{1}{\sqrt{2}} \{ \beta(1)\phi_{\text{Rb}}(1)\alpha(2)\phi_{\text{He}}(2) - \beta(2)\phi_{\text{Rb}}(2)\alpha(1)\phi_{\text{He}}(1) \}. \quad (\text{A.6})$$

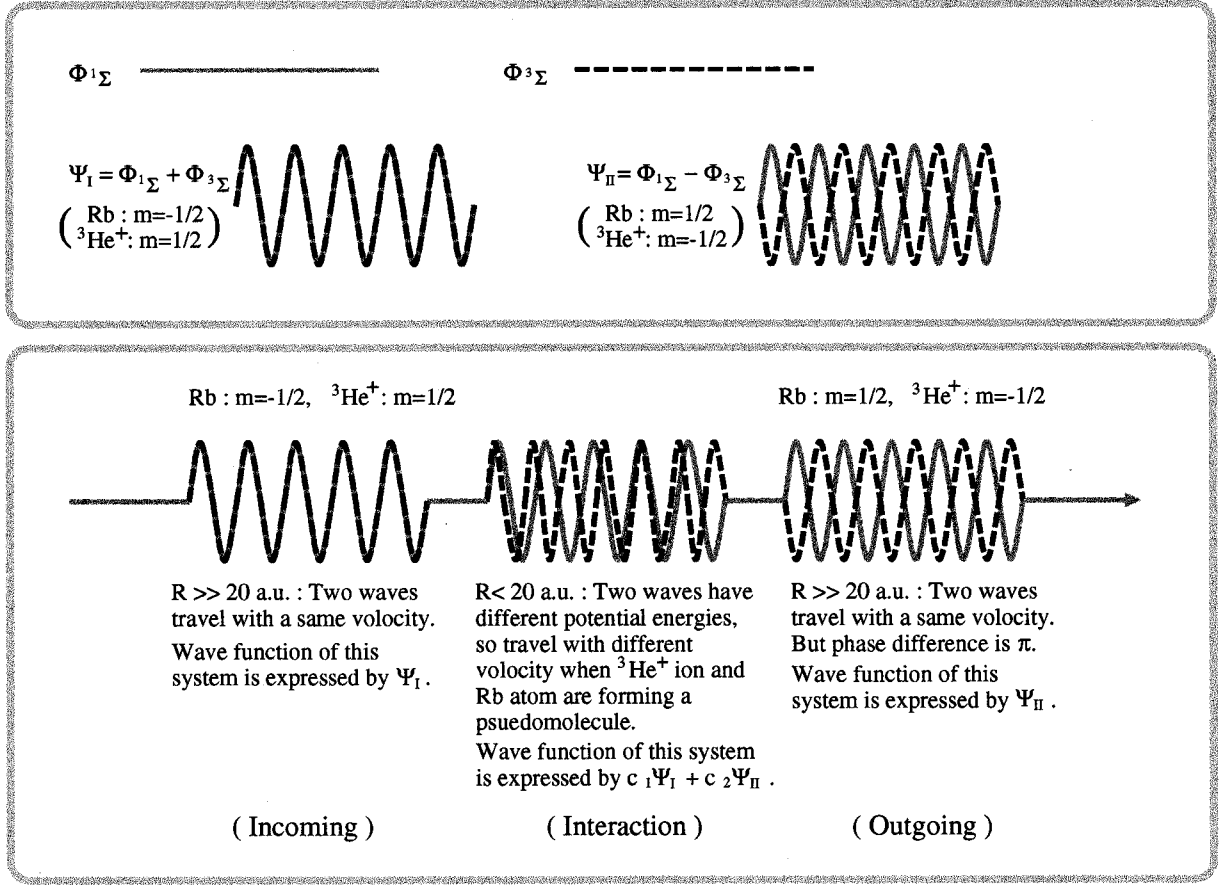


Figure A.1: Mechanism of the spin-exchange

Here,  $\Psi_I$  and  $\Psi_{II}$  are written as a linear superposition of  $\Phi_{1\Sigma}$  and  $\Phi_{3\Sigma}$  as follows.

$$\Psi_I = \frac{1}{\sqrt{2}} (\Phi_{1\Sigma} + \Phi_{3\Sigma}) \quad (\text{A.7})$$

$$\Psi_{II} = \frac{1}{\sqrt{2}} (-\Phi_{1\Sigma} + \Phi_{3\Sigma}) \quad (\text{A.8})$$

Then, this can be also presented using a following matrix.

$$\begin{pmatrix} \Psi_I \\ \Psi_{II} \end{pmatrix} = \begin{pmatrix} \cos \theta & \sin \theta \\ -\sin \theta & \cos \theta \end{pmatrix} \begin{pmatrix} \Phi_{1\Sigma} \\ \Phi_{3\Sigma} \end{pmatrix} \quad (\text{A.9})$$

Here,  $\theta$  is  $\pi/4$ . In the  $\Psi_I$  state, a phase difference between  $\Phi_{3\Sigma}$  and  $\Phi_{1\Sigma}$  is zero. On the other hand, in the  $\Psi_{II}$  state, this phase difference is  $\pi$ .

Let's assume the  $^3\text{He}^+$ -Rb system is initially in the  $\Psi_I$  state. At first, the phase difference between  $\Phi_{1\Sigma}$  and  $\Phi_{3\Sigma}$  is zero. But, when the ion and the atom are closing each other, the phase difference gradually slips out of zero since the  $\Phi_{1\Sigma}$  and  $\Phi_{3\Sigma}$  states has different energy at a small

internuclear separation. In other words, the  $\Psi_{\text{II}}$  state is mixed in a wave function of this system. As a result, the two electrons are exchanged ( Fig. A.1 ).

The spin-exchange cross section is obtained by a following procedure. When an initial state of the  $^3\text{He}^+$ -Rb system is  $\Psi_{\text{I}}$ , the wave function of the system at time  $t$  is

$$|\Psi_{\text{I}}(t)\rangle = \frac{1}{\sqrt{2}} \exp\left(-i \int_0^t E_{\text{t}}/\hbar dt\right) |\Phi_{3\Sigma}\rangle + \frac{1}{\sqrt{2}} \exp\left(-i \int_0^t E_{\text{s}}/\hbar dt\right) |\Phi_{1\Sigma}\rangle. \quad (\text{A.10})$$

A probability which the  $\Psi_{\text{II}}$  state is mixed in the system,  $P(\text{I} \rightarrow \text{II})$ , is

$$\begin{aligned} P(\text{I} \rightarrow \text{II}) &= |\langle \Psi_{\text{II}} | \Psi_{\text{I}}(t) \rangle|^2 = \left| \frac{1}{2} \left\{ -\exp\left(-i \int_0^t E_{\text{s}}/\hbar dt\right) + \exp\left(-i \int_0^t E_{\text{t}}/\hbar dt\right) \right\} \right|^2 \\ &= \sin^2 \left\{ \frac{1}{2} \int_0^t (E_{\text{t}} - E_{\text{s}}) t / \hbar dt \right\}. \end{aligned} \quad (\text{A.11})$$

The spin-exchange cross section is determined by the impact parameter method.

$$\sigma_{\text{se}} = 2\pi \int_0^{\infty} b \sin^2 \frac{\phi_{\text{ts}}}{2} db \quad (\text{A.12})$$

$$\phi_{\text{ts}} = \int_0^t (E_{\text{t}} - E_{\text{s}}) t / \hbar dt \quad (\text{A.13})$$

Where  $b$  is an impact parameter.

## Appendix B

# Potential energy calculation for (He-Rb)<sup>+</sup> quasimolecule

In order to determine the energy difference between  $V_t$  and  $V_s$ , i.e.  $V_{ts}$ , the molecular electronic states for the  ${}^3\text{He}^+\text{-Rb}$  system were calculated by using the valence-bond configuration-interaction method with the Gaussian type pseudopotentials representing the  $\text{Rb}^+$  core [70] by N. Shimakura. The pseudopotential parameters for the  $\text{Rb}^+$  core and the Slater type orbitals (STO's) for the Rb atom were taken from Ref. [70]. The orbital exponents of the STO's for the He atom was obtained by optimizing its energies. The obtained orbital exponents are given in Table B.1. Through

He		Rb	
1s	2.9110000	4s	1.47256
	2.0000000	5s	1.45575
	1.4530000		0.83134
	1.0000000		0.45312
2s	1.3093953 (1.4530000)*	5p	1.06297
	0.5372721 (1.0000000)		0.67145
2p	0.7167531 (1.6998674)		
	0.5057654 (0.5314231)		

\* Values in parenthesis correspond to the triplet manifold.

Table B.1: Slater-type orbital basis set.

the above calculations, the energies of the quasimolecule are evaluated individually for singlets and triplets as a function of  $R$  as numerically shown in Table B.2 and also graphically shown in Fig. B.1. The meaning of the numbers in these table and figure is as follows:

State	Symmetry	Asymptotic limit
1	$1,^3\Sigma$	$\rightarrow \text{He}^+(1s,^2S)+\text{Rb}(5s,^2S)$
2	$1,^3\Sigma$	$\rightarrow \text{He}^+(1s2s,^1,^3S)+\text{Rb}^+$
3	$1,^3\Sigma$	$\rightarrow \text{He}^+(1s2p,^1,^3P)+\text{Rb}^+$
4	$1,^3\Sigma$	$\rightarrow \text{He}^+(1s,^2S)+\text{Rb}(3p,^2P)$

Then, we compare these results at the separated atom limits with the experimental spectroscopic energies. As a result, it is found that the experimental values are reproduced by the present calculation to better than 0.04 % except for the lowest state,  $^3\text{He}(1s^2,^2S) - \text{Rb}^+$  (0.8 %). To ensure validity of the above calculation method, the energies of the  $\text{He}^+$ -Na system (solid curves) are calculated according to the present prescription so as to compare them with the results of M6 and Riera (dotted curves in Fig. B.2) [71] deduced by the CI (configuration interaction) method with Gaussian type functions. From the above comparison, it is found that the results of both methods are approximately equal each other, which indicates the validity of our method. From this discussion, we conclude that we can appropriately use our calculation method for evaluating the spin-exchange cross sections for the  $^3\text{He}^+$ -Rb system.

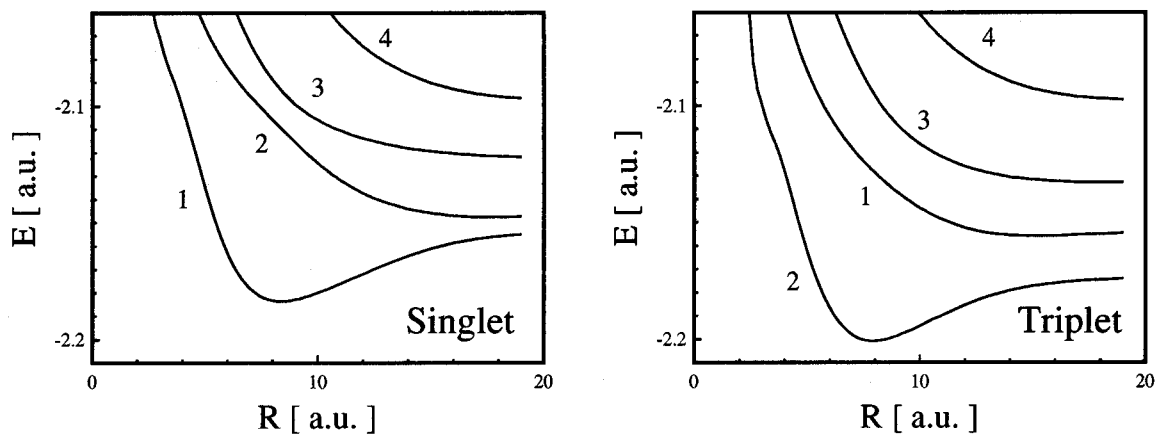


Figure B.1: Potential energy curve for the  $\text{He}^+$ -Rb quasimolecule states calculated by N. Shimakura; left: singlet states, right: triplet states. The numbers indicated are referred to the text.

By using the system energies obtained above,  $V_{\text{ts}}$  for the  $^3\text{He}^+$ -Rb system (solid curve) is calculated as shown in Fig. B.3. For reference,  $V_{\text{ts}}$  for the H-Rb system (dot-dashed curve) is also plotted in this figure [70].

R	Singlet				R	Triplet			
	State 1	State 2	State 3	State 4		State 1	State 2	State 3	State 4
1.0	-0.48607	-0.484563	-0.31438	-0.259089	1.0	-0.577636	-0.44174	-0.296784	-0.119733
1.2	-1.064041	-0.905805	-0.834927	-0.707315	1.2	-1.104119	-0.971071	-0.838518	-0.587891
1.4	-1.457587	-1.307802	-1.232949	-1.132436	1.4	-1.476975	-1.340619	-1.220984	-1.071356
1.6	-1.701158	-1.560802	-1.480636	-1.423038	1.6	-1.710652	-1.571999	-1.465319	-1.397934
1.8	-1.844012	-1.713695	-1.630394	-1.603577	1.8	-1.854003	-1.71646	-1.617523	-1.592413
2.0	-1.948647	-1.828429	-1.746224	-1.72811	2.0	-1.962579	-1.828764	-1.734171	-1.729347
2.2	-2.000288	-1.890971	-1.812029	-1.790496	2.2	-2.019629	-1.891982	-1.805622	-1.795044
2.4	-2.03084	-1.931388	-1.854934	-1.828447	2.4	-2.054691	-1.934943	-1.852232	-1.835336
2.6	-2.05392	-1.962854	-1.888039	-1.857506	2.6	-2.080732	-1.96929	-1.887457	-1.866108
2.8	-2.064822	-1.981195	-1.907575	-1.873791	2.8	-2.093225	-1.99025	-1.908146	-1.883261
3.0	-2.071192	-1.993825	-1.921206	-1.884714	3.0	-2.099852	-2.004929	-1.922238	-1.894502
3.2	-2.078284	-2.005917	-1.934287	-1.895448	3.2	-2.10649	-2.018592	-1.935809	-1.905373
3.4	-2.084116	-2.015823	-1.945229	-1.904311	3.4	-2.111794	-2.029693	-1.947031	-1.914422
3.6	-2.089064	-2.023947	-1.954538	-1.911753	3.6	-2.116385	-2.038724	-1.956707	-1.922232
3.8	-2.094611	-2.031663	-1.963729	-1.919256	3.8	-2.121854	-2.047145	-1.966418	-1.930284
4.0	-2.100806	-2.03902	-1.972922	-1.926997	4.0	-2.128256	-2.055089	-1.976263	-1.938618
4.2	-2.107262	-2.045663	-1.981831	-1.934762	4.2	-2.135065	-2.062271	-1.985849	-1.946785
4.4	-2.113948	-2.051606	-1.990519	-1.942622	4.4	-2.142053	-2.068752	-1.995101	-1.954667
4.6	-2.120899	-2.057006	-1.999132	-1.950634	4.6	-2.149098	-2.074707	-2.004044	-1.962253
4.8	-2.127956	-2.061909	-2.007612	-1.958574	4.8	-2.155968	-2.080183	-2.012571	-1.969455
5.0	-2.134898	-2.066339	-2.015818	-1.966147	5.0	-2.162446	-2.085187	-2.020584	-1.976187
5.2	-2.141551	-2.070357	-2.023637	-1.973159	5.2	-2.168416	-2.089763	-2.028063	-1.982432
5.4	-2.147786	-2.074031	-2.030989	-1.979537	5.4	-2.173827	-2.093963	-2.035035	-1.98821
5.6	-2.153513	-2.077414	-2.037833	-1.985287	5.6	-2.178663	-2.097835	-2.041542	-1.993549
5.8	-2.158672	-2.080545	-2.044159	-1.990458	5.8	-2.182929	-2.101415	-2.04763	-1.998477
6.0	-2.163245	-2.083456	-2.049987	-1.995103	6.0	-2.186645	-2.104737	-2.05335	-2.003026
6.2	-2.167239	-2.086176	-2.055352	-1.999283	6.2	-2.189844	-2.107832	-2.058746	-2.007227
6.4	-2.170678	-2.088731	-2.060296	-2.00305	6.4	-2.192557	-2.110726	-2.063857	-2.011114
6.6	-2.173599	-2.091144	-2.06486	-2.006452	6.6	-2.194819	-2.113442	-2.068711	-2.014715
6.8	-2.176044	-2.093437	-2.069082	-2.009527	6.8	-2.196663	-2.116	-2.07332	-2.01806
7.0	-2.178057	-2.095631	-2.072997	-2.012312	7.0	-2.198121	-2.118418	-2.07769	-2.021179
7.2	-2.179682	-2.097745	-2.076631	-2.014841	7.2	-2.199225	-2.120707	-2.081818	-2.024102
7.4	-2.180962	-2.099799	-2.080008	-2.017145	7.4	-2.200008	-2.122883	-2.085699	-2.026865
7.6	-2.181934	-2.10181	-2.083144	-2.019257	7.6	-2.200505	-2.124955	-2.089329	-2.029508
7.8	-2.182637	-2.103794	-2.086054	-2.021211	7.8	-2.200748	-2.126933	-2.092707	-2.032074
8.0	-2.183103	-2.105763	-2.088745	-2.02305	8.0	-2.200769	-2.128824	-2.095838	-2.034617
8.2	-2.183361	-2.107726	-2.091226	-2.024841	8.2	-2.200598	-2.130634	-2.098732	-2.037175
8.4	-2.183438	-2.109687	-2.093504	-2.026708	8.4	-2.200264	-2.132369	-2.101401	-2.039785
8.6	-2.183359	-2.111644	-2.09559	-2.028912	8.6	-2.199792	-2.134031	-2.103858	-2.042461
8.8	-2.183144	-2.113592	-2.097495	-2.031832	8.8	-2.199206	-2.135624	-2.106121	-2.045191
9.0	-2.182812	-2.115521	-2.099233	-2.035418	9.0	-2.198526	-2.13715	-2.108205	-2.047945
9.2	-2.18238	-2.11742	-2.100818	-2.03921	9.2	-2.197771	-2.138609	-2.110126	-2.050687
9.4	-2.181863	-2.119277	-2.102268	-2.042914	9.4	-2.196956	-2.140004	-2.111898	-2.053383
9.6	-2.181274	-2.121082	-2.103598	-2.046425	9.6	-2.196096	-2.141333	-2.113534	-2.056006
9.8	-2.180625	-2.122827	-2.10482	-2.049715	9.8	-2.195202	-2.142598	-2.115047	-2.058537
10.0	-2.179926	-2.124506	-2.105948	-2.052786	10.0	-2.194286	-2.143798	-2.116447	-2.060966
10.2	-2.179187	-2.126114	-2.106992	-2.05565	10.2	-2.193356	-2.144934	-2.117745	-2.063287
10.4	-2.178415	-2.127649	-2.107963	-2.058323	10.4	-2.192419	-2.146006	-2.118949	-2.065495
10.6	-2.177618	-2.129109	-2.108867	-2.060822	10.6	-2.191484	-2.147013	-2.120068	-2.067593
10.8	-2.176802	-2.130494	-2.109711	-2.063161	10.8	-2.190556	-2.147957	-2.121107	-2.069581
11.0	-2.175973	-2.131807	-2.110502	-2.065355	11.0	-2.18964	-2.148838	-2.122073	-2.071464
11.5	-2.173869	-2.134775	-2.112273	-2.070279	11.5	-2.18743	-2.150771	-2.124206	-2.07573
12.0	-2.171771	-2.137326	-2.113795	-2.074515	12.0	-2.185375	-2.152335	-2.125989	-2.079424
12.5	-2.169725	-2.139494	-2.115107	-2.078174	12.5	-2.183508	-2.153555	-2.127481	-2.08261
13.0	-2.167758	-2.141322	-2.116246	-2.08134	13.0	-2.181852	-2.154466	-2.128712	-2.085348
14.0	-2.164168	-2.144097	-2.118073	-2.086437	14.0	-2.179175	-2.155504	-2.130555	-2.089684
15.0	-2.161136	-2.14591	-2.119414	-2.0902	15.0	-2.177276	-2.155784	-2.131735	-2.092771
16.0	-2.158731	-2.146966	-2.120371	-2.092907	16.0	-2.175986	-2.155632	-2.132424	-2.094874
17.0	-2.156961	-2.147431	-2.12103	-2.094773	17.0	-2.175121	-2.155302	-2.132775	-2.096211
18.0	-2.155761	-2.147468	-2.121471	-2.095978	18.0	-2.174534	-2.154943	-2.132913	-2.096975
19.0	-2.154999	-2.147246	-2.121763	-2.096682	19.0	-2.174126	-2.154621	-2.132936	-2.097337

Table B.2: Calculated potential energies for  $^3\text{He}^+\text{-Rb}$  (all values in a.u.)

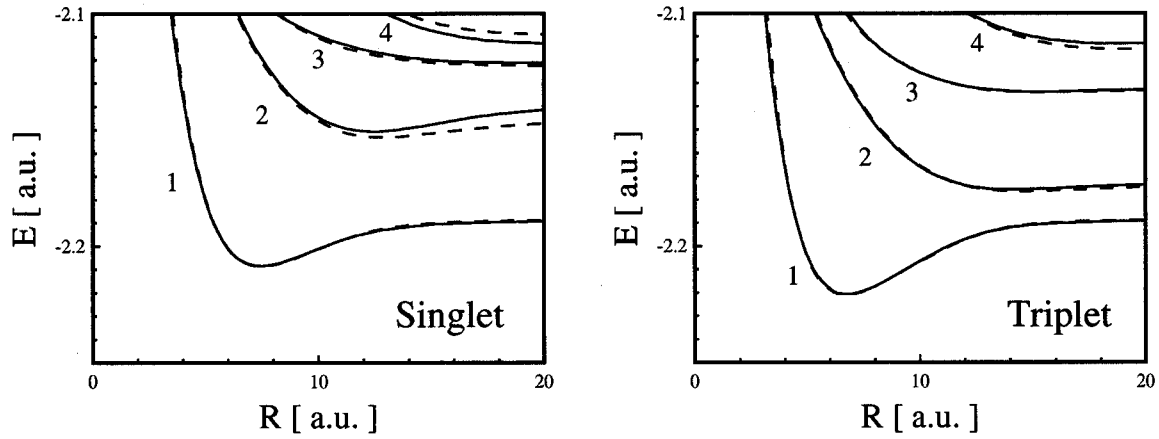


Figure B.2: Potential energy curve for the  $\text{He}^+$ -Na quasimolecule states denoted by  $1^1\Sigma$ , and  $1^3\Sigma$ ; left: singlet states, right: triplet states. Solid curves are calculated results by N. Shimakura and dashed curves are calculated results by M6 and Riera [71]. The numbers indicated are referred to the text.

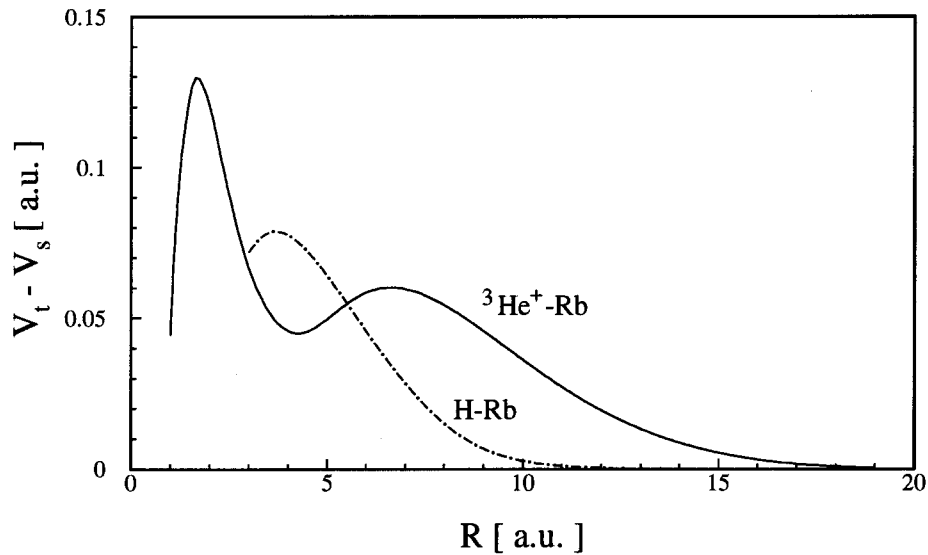


Figure B.3: Potential energy difference,  $V_{ts}$ , between the  $1^1\Sigma$  and  $1^3\Sigma$  states plotted as a function of an internuclear separation. The solid curve is the result of the present calculation for the  $^3\text{He}^+$ -Rb system and a dot-dashed curve is a result of the calculation for the H-Rb system by Stevens et al. [70].

## Appendix C

# A Monte Carlo simulation for evaluating a radial distribution of the Rubidium polarization caused by a radiation trapping effect

The angular distribution for the circularly polarized light and linearly polarized light emitted from the Rb atom are given as  $(1 + \cos^2 \theta)/2$  and  $(\sin^2 \theta)/2$ , respectively, where  $\theta$  is an angle with respect to the direction of the magnetic field. Then, if another Rb atom distributed in the direction of  $B$  absorbs circularly polarized light predominantly, no depolarization occurs. On the other hand, if another Rb atom distributed in direction perpendicular to  $B$  absorbs the linearly polarized light predominantly a serious depolarization occurs. This eventually produces a sheath with a higher polarization in the direction of  $B$ .

To verify this, we performed a Monte Carlo simulation. A uniform Rb density across the cell for the temperature of  $T_{\text{cell}}$ : 90, 110, and 130 °C with atom densities of 0.2, 1.0, and  $2.0 \times 10^{13}$  atoms/cm<sup>3</sup>, respectively, were employed. For each calculation, a sample of 50,000 circularly polarized photons propagating along  $B$  were transported. Fig. 5.21 shows the the Rb polarization along the cell radially. The results confirm that higher atom densities results in lesser polarization, once we leave the central axis. Also, worth noting is that the width of the polarization distribution is very closely related to the mean free path for scattering.

## Appendix D

# Analytical estimation of polarization hole

The  $r_{ce^-}$ , and  $r$ - distributions of the polarization are estimated in the extreme case, i.e.,  $B_z$  is  $\infty$  and the initial beam spot size is 0.

With a Rb thickness less than  $\sim 1 \times 10^{15}$  atoms/cm<sup>2</sup>, a number of the charge exchange collision is  $0 \sim 2$  because the capture and stripping cross sections for this process is an order of  $10^{-15}$  cm<sup>2</sup>. If only one capture process occurs, a charge state of the outgoing <sup>3</sup>He particle becomes neutral and this component does not contribute to formation of the polarization hole. Therefore, the polarization hole is created only by the another collision, i.e., double collisions. In the discussion below, we assume only the double collision. Suppose that a <sup>3</sup>He ion is incident on the Rb vapor under an infinite  $B_z$  with an incident angle,  $\theta$  with respect to the  $z$  axis. The beam trajectory in the Rb cell is schematically shown in Fig. D.1; for a <sup>3</sup>He<sup>+</sup> ion, the trajectory is parallel to the  $z$  axis and for a <sup>3</sup>He atom, the trajectory is a line which has an angle,  $\theta$  with respect to the  $z$  axis.

The  $r$  value at the cell exit is determined simply by the collision points,  $z_1$ , and  $z_2$  where the capture and stripping occur, respectively. A joint probability density function ( joint p.d.f. ) for  $z_1$  and  $z_2$  is

$$f(z_1, z_2) = \frac{2}{3} \sigma_{10} \sigma_{11} e^{-\sigma_{10} L} \exp\{-(\sigma_{11} - \sigma_{10})(z_2 - z_1)\}, \quad (\text{D.1})$$

where the factor of 2/3 means that 1/3 of <sup>3</sup>He<sup>+</sup> ions become to singlet state in the electron capture process. A p.d.f. of  $z (= z_2 - z_1)$  is obtained by the convolution method and given by

$$g_2(z) = \frac{2}{3} \sigma_{10} \sigma_{11} (L - z) e^{-\sigma_{10} L} \exp\{-(\sigma_{11} - \sigma_{10})z\}, \quad (\text{D.2})$$

where  $L$  is the Rb cell length.

Then, the p.d.f. of  $z$ ,  $g_2(z)$  is converted to the p.d.f. of  $r$ ,  $h_2(r)$  by using a relation  $r = z\theta$  as expressed by

$$h_2(r) = \frac{2}{3} \sigma_{10} \sigma_{11} e^{-\sigma_{10} L} (L - r/\theta) \exp\left\{-(\sigma_{11} - \sigma_{10}) \frac{r}{\theta}\right\}. \quad (\text{D.3})$$

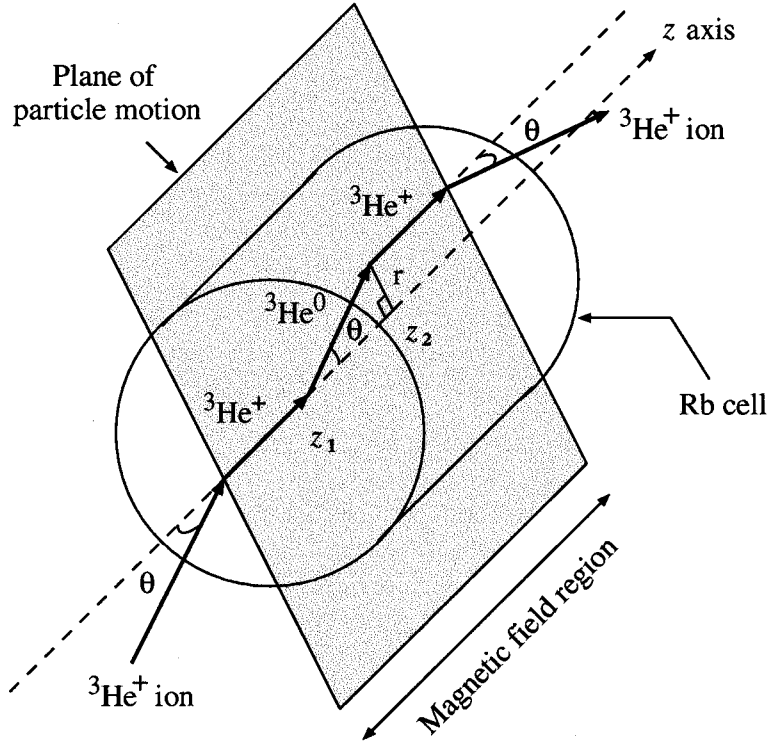


Figure D.1: The schematic view of the beam trajectory in the infinite magnetic field; for a  ${}^3\text{He}^+$  ion, the trajectory is parallel to the  $z$  axis and for a  ${}^3\text{He}^0$  atom, the trajectory is a line which has an angle,  $\theta$  with respect to the  $z$  axis.

An expectation value of  $r$  is then given by

$$R(\theta) = \frac{\int_0^{L\theta} r h_2(r) dr}{\int_0^{L\theta} h_2(r) dr} = R_0 \theta, \quad (\text{D.4})$$

where

$$R_0 = \frac{C_2 L - 2 + (C_2 L + 2)e^{-C_2 L}}{C_2(C_2 L - 1 + e^{-C_2 L})} \quad (\text{D.5})$$

$$C_1 = \sigma_{10} \sigma_{11} e^{-\sigma_{10} L} \quad (\text{D.6})$$

$$C_2 = \sigma_{11} - \sigma_{10} \quad (\text{D.7})$$

If  $\theta$  is uniformly distributed from 0 to  $\theta_{\max}$  the expectation value of  $r$  is given by averaging over

$\theta$  as

$$\begin{aligned} R &= \frac{\int_0^{\theta_{\max}} \theta R(\theta) d\theta}{\int_0^{\theta_{\max}} \theta d\theta} \\ &= \frac{2}{3} R_0 \theta_{\max}, \end{aligned} \tag{D.8}$$

where  $r_{ce}$  is defined by

$$r_{ce} = 2R \tag{D.9}$$

## Appendix E

# Fraction of $\text{Rb}^+$ ions produced by charged particle beam passing through Rb vapor cell

The charged particles ionize the Rb atoms. This causes reduction of a number of Rb atoms and consequently reduces the polarization of the  $^3\text{He}$  beam. We consider a sample of polarized Rb gas with a thickness  $x$  atoms/cm<sup>2</sup> stored in a Rb vapor cell with a bore radius  $r$  cm and a length of  $l$  cm.

We assume that the ionization cross section is approximately equal to the electron capture cross section,  $\sigma_{10}$ . Consider a beam of  $I$  A incident on the polarized Rb atoms. Under the above condition the formation rate of  $\text{Rb}^+$  ions by the beam per length of  $dx$  is

$$\frac{I}{e}\sigma_{10}dx = \frac{I}{e}\sigma_{10}\rho_{\text{Rb}}dl, \quad (\text{E.1})$$

where  $e$  and  $\rho_{\text{Rb}}$  are an elementary charge and the Rb vapor density ( atoms/cm<sup>3</sup> ). From the above equation, the formation rate per unit volume is

$$S^+ = \frac{I}{e\pi r^2}\sigma_{10}\rho_{\text{Rb}}. \quad (\text{E.2})$$

Next, consider probability of the  $\text{Rb}^+$  ion to form a Rb atom by possible processes such as collisions with the cell wall or replacement with another Rb atom provided by the Rb sample source. This rate is given by the wall collision rate,  $S^0$ , which is obtained from gas kinematic theory. Suppose that there are  $N^+$  ions in the Rb cell with a volume  $V$ . The number of ions in the velocity range from  $v$  to  $v + dv$  and in the angular range from  $\theta$  to  $\theta + d\theta$  is given by

$$n(v, \theta) = dN_v(v)d\omega/4\pi = \sin\theta d\theta d\phi dN_v(v)/4\pi \quad (\text{E.3})$$

The number of the wall collisions in area  $dA$  per time  $dt$  is

$$dq = \int \int \frac{n(v, \theta) v \cos \theta dt dA}{V} \quad (E.4)$$

$$= \int_0^{\pi/2} \sin \theta \cos \theta d\theta \int_0^{2\pi} d\phi \frac{v dt dA}{4\pi V} \quad (E.5)$$

$$= \frac{v}{4V} dN_v(v) dA dt. \quad (E.6)$$

Assuming that velocity distribution of ions obeys the law of Maxwell's velocity distribution,  $N_v(v)$  is expressed by

$$dN_v(v) = \frac{4N^+}{\sqrt{\pi}} \left( \frac{m}{2kT} \right)^{\frac{3}{2}} v^2 \exp\left(-\frac{mv^2}{2kT}\right) dv. \quad (E.7)$$

Here,  $k$ ,  $T$  and  $m$  are the Boltzman constant, vapor temperature and mass of Rb atom, respectively. Substituting E.7 into E.6 and integrating this over the whole velocity range, the number of the wall collisions for an area  $A$  per unit time is obtained as follows;

$$\frac{dQ}{dt} = \frac{A}{V} \sqrt{\frac{kT}{2\pi m}} N^+ \quad (E.8)$$

Consequently, the recombination rate from a  $Rb^+$  ion to a Rb atom,  $S^0$  is given by

$$S^0 = \frac{A}{V} \sqrt{\frac{kT}{2\pi m}}. \quad (E.9)$$

Finally, the production rate of  $Rb^+$  ions is given by

$$\frac{dN^+}{dt} = S^+ N^0, \quad (E.10)$$

and the recombination rate of  $Rb^0$  ions is

$$\frac{dN^0}{dt} = S^0 N^+. \quad (E.11)$$

In an equilibrium state, the production and reformation rates should be equal as shown by

$$S^+ N^0 = S^0 N^+ \quad (E.12)$$

Substituting eqs. E.2 and E.9 into eq. E.12, a ratio of number of the Rb ions to the atoms is given by,

$$R = \frac{N^+}{N^0} = \frac{I\sigma_{10}\rho_{Rb}V}{e\pi r^2 A} \sqrt{\frac{2\pi m}{kT}} \quad (E.13)$$

$$= \frac{I\sigma_{10}\rho_{Rb}l}{e(2\pi r l + \pi r^2)} \sqrt{\frac{2\pi m}{kT}} \quad (E.14)$$

Here, in the evaluation of the above result, the form of the Rb cell is assumed to be a coaxial tube with a cell length of  $l$  and a bore radius of  $r$ . By using the total number,  $N_t$  ( $=N^0 + N^+$ ), the fraction of the  $Rb^+$  ions is expressed by

$$F^+ = \frac{N^+}{N_t} = \frac{1}{1 + R^{-1}}. \quad (E.15)$$

# Bibliography

- [1] G. Clausnitzer, R. Fleischmann, and H. Schopper, *Z. Physik* **144**, 336 (1956).
- [2] *Nucl. Instrum. Methods A* **402** (1998), proceedings of the *7th RCNP International Workshop on Polarized  $^3\text{He}$  Beams and Gas Targets and Their Application* Kobe, Japan, 1997, edited by M. Tanaka.
- [3] E. C. J. Ashman et al., *Phys. Lett. B* **206**, 364 (1988).
- [4] A. Kastler, *J. Physique. Rad.* **11**, 255 (1950).
- [5] L. F. Wouters, *Phys. Rev.* **75**, 213 (1951).
- [6] K. Hatanaka, K. Takahisa, and H. Tamura, *AIP Conf. Proc.* **421**, 352 (1998), proceedings of *Polarized Gas Targets and Polarized Beams*, Urbana, Illinois, 1997.
- [7] V. Derenchuk, R. Brown, and H. Petri, in *The International Workshop on Polarized Beams and Polarized Gas Targets* (World Scientific, Cologne, Germany, 1995), p. 180.
- [8] P. D. Eversheim, in *The International Workshop on Polarized Beams and Polarized Gas Targets* (World Scientific, Cologne, Germany, 1995), p. 224.
- [9] W. E. Lamb and R. C. Retherford, *Phys. Rev.* **79**, 549 (1950).
- [10] L. Madansky and G. Owen, *Phys. Rev. Lett.* **2**, 209 (1959).
- [11] B. L. Donnally and W. Sawyer, *Phys. Rev. Lett.* **15**, 439 (1965).
- [12] B. L. Donnally, T. Clapp, W. Sawyer, and M. Schultz, *Phys. Rev. Lett.* **12**, 502 (1964).
- [13] L. W. Anderson, *Nucl. Instrum. Methods* **167**, 363 (1979).
- [14] E. K. Zavoiskii, *Sov. Phys. JETP* **5**, 378 (1957).
- [15] W. Haeberli, *Annual Rev. Nucl. Sci.* **17**, 373 (1967).
- [16] Y. Mori, K. Ikegami, A. Takagi, and S. Fukumoto, *Nucl. Instrum. Methods* **220**, 264 (1984).

- [17] A. Takagi, M. Kinsho, K. Ikegami, Z. Igarashi, and Y. Mori, AIP Conf. Proc. **421**, 347 (1998), proceedings of *Polarized Gas Targets and Polarized Beams*, Urbana, Illinois, 1997.
- [18] C. D. P. Levy, A. N. Zelenski, K. Jayamanna, M. McDonald, R. Ruegg, P. W. Schmor, and G. Wight, AIP Conf. Proc. **293**, 179 (1994), proceedings of *Polarized Ion Sources and Polarized Gas Targets*, Madison, Wisconsin, 1993.
- [19] A. N. Zelenski, in *The International Workshop on Polarized Beams and Polarized Gas Targets* (World Scientific, Cologne, Germany, 1995), p. 111.
- [20] C. D. P. Levy, K. Jayamanna, S. G. Kadantsev, M. McDonald, P. W. Schmor, J. Welz, G. W. Wight, A. N. Zelenski, and T. Sakae, in *The International Workshop on Polarized Beams and Polarized Gas Targets* (World Scientific, Cologne, Germany, 1995), p. 120.
- [21] A. N. Zelenski, V. I. Davydenko, G. Dutto, A. A. Hamian, V. Klenov, C. D. P. Levy, I. I. Morozov, P. W. Schmor, W. T. H. van Oers, and G. W. Wight, AIP conf. proc. **421**, 372 (1998), proceedings of *Polarized Gas Targets and Polarized Beams*, Urbana, Illinois, 1997.
- [22] C. D. P. Levy and A. N. Zelenski, Rev. of Sci. Instrum. **69**, 732 (1998).
- [23] R. L. York, D. Tupa, D. R. Swenson, M. W. McNaughton, and O. B. vanDyck, AIP Conf. Proc. **293**, 196 (1994), proceedings of *Polarized Ion Sources and Polarized Gas Targets*, Madison, Wisconsin, 1993.
- [24] A. N. Zelenskii, S. A. Kokhanovskii, V. M. Lobashev, and V. G. Polushkin, Nucl. Instrum. Methods A **245**, 223 (1986).
- [25] A. N. Zelenski, V. Klenov, Y. Kuznetsov, V. Zoubets, G. Dutto, S. Kadantsev, C. D. P. Levy, G. W. Wight, P. W. Schmor, J. Alessi, *et al.*, in *Proceedings of the 1999 Particle Accelerator Conference (PAC)* (1999).
- [26] P. G. Sona, Energie Nucleaire **14**, 295 (1967).
- [27] S. D. Baker, E. B. Carter, D. O. Findley, and L. L. Htfield, Phys. Rev. Lett. **20**, 738 (1968).
- [28] O. Karban, S. W. Oh, and W. B. Powell, Phys. Rev. Lett. **31**(2), 109 (1973).
- [29] R. J. Slobodrian, C. Rioux, J. Giroux, and R. Roy, AIP Conf. Proc. **131**, 8 (1985).
- [30] M. Tanaka, N. Shimakura, T. Oshima, K. Katori, M. Fujiwara, H. Ogata, and M. Kondo, Phys. Rev. A **50**, 1184 (1994).
- [31] A. S. Belov, Nucl. Instrum. Methods A **402**, 205 (1998).
- [32] G. G. Ohlsen, J. L. McKibben, R. R. S. Jr., and G. P. Lawrence, Nucl. Instrum. Methods **73**, 45 (1969).

- [33] M. Tanaka, M. Fujiwara, S. Nakayama, and L. W. Anderson, *Phys. Rev. A* **52**, 392 (1995).
- [34] B. H. Bransden and C. J. Joachain, *Physics of Atoms and Molecules* (Wiley, New York, 1983).
- [35] W. Franzen, *Phys. Rev.* **115**, 850 (1959).
- [36] H. J. Besch, U. Koepf, and E. W. Otten, *Phys. Lett.* **25B**, 120 (1967).
- [37] U. Koepf, H. J. Besch, E. W. Otten, and C. von Platten, *Z. Physik* **226**, 297 (1969).
- [38] M. A. Bouchiat and J. Brossel, *Phys. Rev.* **147**, 41 (1966).
- [39] W. Happer, *Phys. Rev.* **B1**, 2203 (1970).
- [40] C. D. P. Levy, P. W. Schmor, and W. M. Law, *J. Appl. Phys.* **63**, 4819 (1988).
- [41] D. R. Swenson and L. W. Anderson, *Nucl. Instrum. Methods* **B12**, 157 (1985).
- [42] D. R. Swenson and L. W. Anderson, *Nucl. Instrum Methods* **B29**, 627 (1988).
- [43] R. J. Knize, *Phys. Rev. A* **40**, 6219 (1989).
- [44] T. E. Chupp, R. J. Holt, and R. G. Milner, *Ann. Rev. Nucl. Part. Sci.* **45**, 373 (1994).
- [45] M. E. Wagshul and T. E. Chupp, *Phys. Rev. A* **49**, 3854 (1994).
- [46] T. Yamagata, M. Tanaka, K. Yonehara, Y. Arimoto, T. Takeuchi, M. Fujiwara, Y. A. Plis, L. W. Anderson, and R. Morgenstern, *Nucl. Instrum. Methods A* **402**, 199 (1998).
- [47] M. Tanaka, T. Yamagata, K. Yonehara, T. Takeuchi, Y. Arimoto, M. Fujiwara, Y. Plis, L. W. Anderson, and R. Morgenstern, *Phys. Rev. A* **60**, R3354 (1999).
- [48] W. Happer and W. A. V. Wijngaarden, *Hyperfine Interactions* **38**, 435 (1987).
- [49] M. Prutton, *Surface Physics* (Oxford University Press, 1975).
- [50] C. H. Holbrow, A. P. Ghosh, D. Heinzen, X. Zu, W. W. Q. Jr., G. Shimkaveg, P. G. Pappas, J. E. Thomas, , and M. S. Feld, *Phys. Rev. A* **34** (1986).
- [51] C. Martin, T. Walker, L. W. Anderson, and D. R. Swenson, *Nucl. Instrum. Methods A* **335**, 233 (1993).
- [52] T. Takeuchi, T. Yamagata, K. Yonehara, Y. Arimoto, and M. Tanaka, *Rev. of Sci. Instrum.* **69**, 412 (1998).
- [53] H. Wollnik *et al.*, *Computer Program "GIOS"*, Giessen University.

- [54] M. Berz, *COSY INFINITY Version5 User's Guide and Reference Manual*, Michigan State University, NSCL Technical Report MSUCL-977.
- [55] M. Dulick, *Computer Program "FARADAY"*, Los Alamos National Laboratory.
- [56] T. J. Killian, *Phys. Rev.* **27**, 578 (1926).
- [57] W. H. S. D. Stoller and F. J. Dyson, *Phys. Rev. A* **44**, 7459 (1991).
- [58] T. Ogitsu, T. Higo, and H. Mizuno, in *Proceedings of the 1995 Particle Accelerator Conference (PAC)* (1996).
- [59] G. Walker, *Cryocoolers*, vol. 1 (Plenum Press, New York and London, 1983).
- [60] H. J. Andrä, *Physica Scripta* **9**, 257 (1974).
- [61] T. Ohshima, K. Abe, K. Katori, M. Fujiwara, T. Itahashi, H. Ogata, M. Kondo, and M. Tanaka, *Phys. Lett. B* **274**, 163 (1992).
- [62] U. Fano and J. H. Macek, *Rev. Mod. Phys.* **45**(4), 553 (1973).
- [63] T. Sakae, T. Yamamoto, A. Zelenski, and C. Levy, *Nucl. Instrum. Methods A* **402**, 191 (1998).
- [64] R. J. Girnius and L. W. Anderson, *Nucl. Instrum. Methods* **137**, 373 (1976).
- [65] A. S. Schlachter, D. H. Loyd, P. J. Bjorkholm, L. W. Anderson, and W. Haeberli, *Phys. Rev.* **174**, 201 (1968).
- [66] D. R. Swenson, D. Tupa, and L. W. Anderson, *J. Phys. B* **18**, 4433 (1985).
- [67] J. R. Peterson and D. C. Lorents, *Phys. Rev.* **182**, 152 (1969).
- [68] A. N. Zelenski, C. D. P. Levy, W. T. H. van Oers, P. W. Schmor, J. Welz, and G. W. Wight, *AIP Conf. Proc.* **339**, 650 (1995).
- [69] A. N. Zelenski, private communication.
- [70] W. J. Stevens, A. M. Karo, and J. R. Hiskes, *J. Chem. Phys.* **74**, 3989 (1981).
- [71] O. Mó and A. Riera, *J. Mol. Struct. (Theochem)* **164**, 135 (1988).

## Short curriculum vitae of Yasushi Arimoto

### Personal data

Date of birth: July 5, 1972  
Place of birth: Ayabe, Kyoto Pref., Japan

### Education

1991-1995 Osaka City University  
Bachelor of Science, March 1995  
Major: Physics  
1995-1997 Osaka University  
Master of Science, March 1997  
Major: Physics  
1997-2000 Osaka University  
Doctor of Science, March 2000  
Major: Physics

### Publications

1. Y. Arimoto, N. Shimakura, K. Yonehara, M. Tanaka, T. Yamagata, and T. Takeuchi, "Unexpected reduction of the spin-exchange cross section for fast  $^3\text{He}^+$  ions incident on Rb atoms", *European Physical Journal D*, to be published.
2. M. Tanaka, T. Yamagata, K. Yonehara, T. Takeuchi, Y. Arimoto, M. Fujiwara, Y. Plis, L. W. Anderson, and R. Morgenstern, "Production of a nuclear polarized  $^3\text{He}$  beam by multiple electron capture and stripping collisions", *Physical Review A* **60**, R3354 (1999).
3. T. Yamagata, M. Tanaka, K. Yonehara, Y. Arimoto, T. Takeuchi, M. Fujiwara, Yu. A. Plis, L. W. Anderson, and R. Morgenstern, "Development of RCNP polarized  $^3\text{He}$  ion source based on electron pumping", *Nuclear Instruments & Methods A* **402** Proceedings of *HELION97 workshop*, 199 (1998).
4. T. Takeuchi, T. Yamagata, K. Yonehara, Y. Arimoto and M. Tanaka, "Ion optics for multiple charge exchange collisions determined by means of Monte Carlo simulation", *Review of Scientific Instruments* **69**, 412 (1998).

## Conference proceedings and presentations

1. 有本靖、米原克也、竹内猛、田中正義、山県民穂、“偏極  $^3\text{He}$  イオン源の VME-Sbus インターフェイスによるコントロールシステムとデータ収集システムの開発”、日本物理学会秋の分科会、佐賀大学、1996 年 10 月.
2. 有本靖、米原克也、竹内猛、田中正義、山県民穂、“ビームフォイル分光法による  $^3\text{He}$  ビームの核偏極度の測定”、日本物理学会年会、名城大学、1997 年 3 月.
3. 有本靖、米原克也、竹内猛、田中正義、山県民穂、“ビームフォイル分光法による  $^3\text{He}$  ビームの核偏極度の測定 II”、日本物理学会年会、東邦大学、1998 年 3 月.
4. 有本靖、米原克也、竹内猛、田中正義、山県民穂、“ビームフォイル分光法による  $^3\text{He}$  ビームの核偏極度の測定 III”、日本物理学会年会、広島大学、1999 年 3 月.
5. Y. Arimoto, K. Yonehara, T. Takeuchi, M. Tanaka and T. Yamagata, “Development of Measurement and Control System for Polarized  $^3\text{He}$  Ion Source Based on Electron Pumping” Proceedings of *the 11th Symposium on Accelerator Science and Technology*, SPring-8, Sayo, Hyogo, 14 (1997).
6. Y. Arimoto, N. Shimakura, K. Yonehara, M. Tanaka, T. Yamagata, and T. Takeuchi, “Unexpected reduction of spin-exchange cross section for fast  $^3\text{He}^+$  ion incident on Rb atom” Proceedings of *the 12th Symposium on Accelerator Science and Technology*, RIKEN, Wako, Saitama, 22 (1999).
7. M. Tanaka, T. Yamagata, K. Yonehara, T. Takeuchi, Y. Arimoto, M. Fujiwara, Y. Plis, L. W. Anderson, and R. Morgenstern, “Polarized  $^3\text{He}$  Ion Source Based on Electron Pumping”, Proceedings of *High Energy Spin Physics*, Protovino, Moscow, 625 (1998).